Development of Data Analytics and Modeling Tools for Civil Infrastructure Condition Monitoring Applications

Jinwoo Jang

Submitted in partial fulfillment of the

requirements for the degree

of Doctor of Philosophy

in the Graduate School of Arts and Sciences

COLUMBIA UNIVERSITY

2016

ABSTRACT

Development of Data Analytics and Modeling Tools for Civil Infrastructure Condition Monitoring Applications

Jinwoo Jang

This dissertation focuses on the development of data analytics approaches to two distinct important condition monitoring applications in civil infrastructure: structural health monitoring and road surface monitoring. In the first part, measured vibration responses of a major long-span bridge are used to identify its modal properties. Variations in natural frequencies over a daily cycle have been observed with measured data, which are probably due to environmental effects such as temperature and traffic. With a focus on understanding the relationships between natural frequencies and temperatures, a controlled simulation-based study is conducted with the use of a full-scale finite element (FE) model and four regression models. In addition to the temperature effect study, the identified modal properties and the FE model are used to explore both deterministic and probabilistic model updating approaches. In the deterministic approach (sensitivity-based model updating), the regularization technique is applied to deal with a trade-off between natural frequency and mode shape agreements. Specific nonlinear constraints on mode shape agreements are suggested here. Their capabilities to adjust mode shape agreements are validated with the FE model. To the best of the author's knowledge, the sensitivity-based clustering technique, which enables one to determine efficient updating parameters based on a sensitivity analysis, has not previously been applied to any *civil* structure. Therefore, this technique is adapted and applied to a full-scale bridge model for the first time

to highlight its capability and robustness to select physically meaningful updating parameters based on the sensitivity of natural frequencies with respect to both mass and stiffness-related physical parameters. Efficient and physically meaningful updating parameters are determined by the sensitivity-based clustering technique, resulting in an updated model that has a better agreement with measured data sets. When it comes to the probabilistic approach, the application of Bayesian model updating to large-scale civil structures based on real data is very rare and challenging due to the high level of uncertainties associated with the complexity of a large-scale model and variations in natural frequencies and mode shapes identified from real measured data. In this dissertation, the full-scale FE model is updated via the Bayesian model updating framework in an effort to explore the applicability of Bayesian model updating to a more complex and realistic problem. Uncertainties of updating parameters, uncertainty reductions due to information provided by data sets, and uncertainty propagations to modal properties of the FE model are estimated based on generated posterior samples.

In the second part of this dissertation, a new innovative framework is developed to collect pavement distress data via multiple vehicles. Vehicle vibration responses are used to detect isolated pavement distress and rough road surfaces. GPS positioning data are used to localize identified road conditions. A real-time local data logging algorithm is developed to increase the efficiency of data logging in each vehicle client. Supervised machine learning algorithms are implemented to classify measured dynamic responses into three categories. Since data are collected from multiple vehicles, the trajectory clustering algorithm is introduced to integrate various trajectories to provide a compact format of information about road surface conditions. The suggested framework is tested and evaluated in real road networks.

Table of Contents

List of Figures **vi**

List of Tables **xi**

1 Scope **1**

1.1 Dissertation Outline 2

1.1.1 Structural Health Monitoring 2

1.1.2 Road Surface Monitoring 6

I Structural Health Monitoring **8**

2 Operational Modal Analysis and a Full-Scale FE Model of a Large Suspension Bridge **9**

2.1 Overview of the Enhanced Frequency Domain Decomposition Method 10

2.2 Ambient Dynamic Test on a Large Suspension Bridge 12

2.3 Initial FE Model of a Bridge 15

3 Sensitivity-based Model Updating **21**

3.1 Introduction 22

3.2 Sensitivity-based Model Updating Procedures 25

3.3 Overview of the Interior Point Method for Optimization 27
3.4 Application of Model Updating and the Results 30
3.5 Regularization: Implementation of a Nonlinear Constraint Equation in Model Updating 37
3.5.1 Multi objectives in model updating 37
3.5.2 Regularization on a mode shape agreement 39
3.5.3 Updating results with nonlinear constrains 41
3.6 Sensitivity-based Clustering for Parameterization in Model Updating 46
3.6.1 Importance of parameterization in model updating 46
3.6.2 Sensitivity analysis on decomposed structural components . . 47
3.6.3 Hierarchical clustering for the sensitivities of natural frequencies 49
3.6.4 Updating parameters selected by the sensitivity-based clustering and the interpretation of their physical meanings 52
3.6.5 Updating results with sensitivity-based clustering 57
3.7 Conclusions 60
3.7.1 Importance of system identification technique in model updating 60
3.7.2 Nonlinear constraints in balancing between natural frequencies and mode shapes 61
3.7.3 The selection of the modal parameters sensitivity-based clustering analysis 62
3.7.4 The results of four model updating exercises 62

4 Bayesian Model Updating **64**

4.1 Introduction 64
4.2 Overview of the Bayesian Model Updating Framework 68
4.3 Overview of Hybrid Monte Carlo Simulations 70

4.4 Bayesian Model Updating of a Full-scale FE Model 74
4.4.1 Likelihood function and prior PDF 74
4.4.2 Generated posterior samples by the HMC simulation 77
4.4.3 Correlation between updating parameters 79
4.4.4 Probabilities of the updated parameters and the variations of the natural frequencies and mode shapes of the FE model . . 81
4.4.5 Modeling error reductions after Bayesian model updating . . . 88
4.5 Conclusions 91

5 Temperature Effects on Natural Frequencies 94
5.1 Background 95
5.2 Modeling of thermal effects on natural frequencies 97
5.3 Spatial variations in temperatures over the bridge 102
5.4 Regression analysis 107
5.4.1 Learning model: random forest, neural network, and SVM . . 107
5.4.2 Result of regression analysis 109

II Road Surface Monitoring 111

6 Framework of Road Surface Monitoring to Detect Pavement Distress via Multiple Vehicles 112
6.1 Introduction 112
6.2 Road Surface Monitoring System 117
6.2.1 Sensor package with micro computer 117
6.3 Data Logging Algorithm in Vehicle Clients 118
6.3.1 Signal processing of measured data 119
6.3.2 Data Logging Mechanism Based on the Level of Vibrations . . 121

6.4 Street Defect Classifier at Back-end Server 126
6.4.1 Division of logged data into smaller fragments 126
6.4.2 Output categories of a classifier 129
6.4.3 Selection of the input parameters for a supervised machine learning and the manually labeled data for the training of classifiers 131
6.4.4 Principal component analysis on numeric input parameters . . 132
6.4.5 Multilayer neural network for the classification 133
6.4.6 Random forest for the classification 135
6.4.7 Results of the classification 137
6.5 Discussion 142
6.6 Conclusions and Future Work 146

7 Trajectory Clustering: Application to Road Surface Monitoring 148
7.1 Introduction 148
7.2 Trajectory Clustering analysis 150
7.2.1 Inter-vector distance function 150
7.2.2 Hierarchical clustering 152
7.2.3 Representative trajectories 153
7.2.4 Robustness of the trajectory clustering for measurement noise 154
7.3 Application: Integration of the Result of Road Surface Monitoring System 155
7.3.1 The rating of road surface conditions for each trajectory cluster 155
7.3.2 GPS accuracy 159
7.4 Conclusions 162

III Conclusions **163**

8 Conclusions **164**

Bibliography **168**

List of Figures

2.1 The first singular values of the PSD matrices for four data sets: (a) 3AM data set; (b) 8AM data set; (c) 12PM data sets; and (d) 5PM data sets. 14

2.2 Identified mode shapes from the measured data. 16

2.3 Polar plots for mode shapes. 17

2.4 AutoMAC matrix of the identified mode shapes. 17

2.5 Initial FE model of a large suspension bridge. 18

3.1 Flowchart of the model updating procedure. 33

3.2 Convergence of the updating parameters during the optimization procedure. 35

3.3 MAC pairing matrix between the identified mode shapes and updated mode shapes. 36

3.4 MAC pairing matrices between the identified mode shapes and the mode shapes of the updated models with the MAC constraints: (a) MAC level 0.7; and (b) MAC level 0.8. 43

3.5 Convergence of the updating parameters during the optimization procedure with two levels of the MAC constraints:(a) MAC level 0.7; and (b) MAC level 0.8. 44

3.6 Comparison of optimized updating parameters: Section 3, 0.7 MAC level, and 0.8 MAC level. 45
3.7 Sensitivity to the mass densities and Young's moduli of the decomposed structural components and spring coefficients: 70 out of the 279 physical parameters. 48
3.8 Hierarchical binary cluster tree with 30 leaf nodes: (a) Young's modulus & spring coefficient; and (b) Mass density. 51
3.9 Cluster analysis result of mass densities: the locations of the structural components in the clusters and the corresponding sensitivity matrices: (a) topological locations of cluster 2; (b) sensitivity matrix of cluster 2; (c) topological locations of cluster 3; (d) sensitivity matrix of cluster 3; (e) topological locations of cluster 5; and (f) sensitivity matrix of cluster 5. 53
3.10 Cluster analysis result of stiffness-related parameters: the locations of the structural components in the clusters and the sensitivity matrices: (a) topological locations of cluster 6; (b) sensitivity matrix of cluster 6; (c) topological locations of cluster 7; (d) sensitivity matrix of cluster 7; (e) topological locations of cluster 22; and (f) sensitivity matrix of cluster 22. 54
3.11 Sensitivity matrix of clusters. 56
3.12 Convergence of the updating parameters, which are determined by the sensitivity-based clustering method. 58
3.13 MAC pairing matrix between the identified mode shapes and the mode shapes of the updated model with updating parameters determined by the sensitivity-based clustering. 59

4.1 Algorithm for the HMC method. 73
4.2 Posterior samples (θ_1 - θ_{12}) generated by HMC simulation. 78
4.3 Convergence to stationarity for selected updating parameters (θ_3, θ_6, and θ_{22}): (a) moving averages; and (b) moving standard deviation. . . 80
4.4 Pairwise plots for selected posterior samples (θ_3, θ_6, and θ_{22}). 82
4.5 Pairwise plots for selected posterior samples (θ_3, θ_6, and θ_{22}). 82
4.6 Histograms of the updated parameters (posterior samples) θ_1 - θ_{22}. . . 84
4.7 Kernel density estimation: PDFs of updated parameter θ_1 - θ_{22} estimated by KDE. 85
4.8 95% confidence intervals for the updated parameters (posterior samples). 86
4.9 Sensitivity matrix of natural frequencies with respect to updating parameters θ (more uncertainty reductions for θ_6, θ_{15}, and θ_{22} as shown in Table 4.1). 87
4.10 Variation of the natural frequencies of the FE model for selected modes (H1, V1, V2, T1, SV1, H2, and V3): histograms and PDFs estimated by KDE. 89
4.11 Variation of the MAC values between the identified model shapes and those from the FE model for selected modes (H1, V1, V2, T1, SV1, H2, and V3): histograms and PDFs estimated by KDE. 90

5.1 Locations of 22 parameters for temperatures of the structural components ($T_1 - T_{22}$). 103
5.2 Realization of temperature fields: (a) five realizations of the temperature field T_i; (b) histogram of the maximum differences in the realization; and (c) correlation matrix of the generated temperature fields. . 104

5.3 Variance of the temperature fields explained by principal components. 105

6.1 Architecture of the proposed road surface monitoring system. 117

6.2 Means shifting correction by removing EMA values: (a) acceleration responses in the y direction with the EMA values; and (b) EMA removed acceleration responses in the y direction. 120

6.3 Determination of the thresholds based on the preselected actual 23 street defects. 122

6.4 Flowchart of the local data logging algorithm. 123

6.5 Example of a logged data segment: (a) acceleration in the y direction; (b) acceleration in the z direction; (c) RMS_y; and (d) RMS_z. 125

6.6 GPS locations of the data segments. 127

6.7 Fragmentation of the logged *data segment*: (a) acceleration responses in the y direction; (b) acceleration responses in the z direction; (c) RMS values in the y direction; and (d) RMS values in the z direction. 128

6.8 Three classes of street defects: (a) impulse class; (b) rough class; and (c) smooth class. 130

6.9 Principal component analysis for manually labeled inputs. 134

6.10 Validation confusion matrices of the neural network. 136

6.11 Structure of feedforward neural networks. 136

6.12 Schematic of random forests. 138

6.13 Validation confusion matrices of the random forest. 138

6.14 Detected street defects based on the data collected from three different vehicles: (a) result from the vehicle 1; (b) result from the vehicle 2; and (c) result from the vehicle 3. 140

6.15 Identified road surface conditions on the overlapping route: (a) result from the vehicle 1, and (b) result from the vehicle 3. 141

6.16 Classification results on the overlapping route: (a) result from the vehicle 1 and the "Pothole + Rough" ground truth; (b) result from the vehicle 3 and the "Pothole + Rough" ground truth; (c) result from the vehicle 1 and the "Manhole + Raveling" ground truth; (d) result from the vehicle 3 and the "Manhole + Raveling" ground truth;(e) result from the vehicle 1 and the "Uneven surface" ground truth; and (f) result from the vehicle 3 and the "Uneven surface" ground truth. . . 143

7.1 Trajectory clustering. 150

7.2 Distance function for two trajectory. 151

7.3 Representative trajectory. 153

7.4 Trajectory clustering on simulated data sets: (a) The histogram of measurement errors in meter; (b) simulated trajectories; and (b) corresponding representative trajectories. 156

7.5 Results of the trajectory clustering analysis: (a) representative trajectories in the small area; (b) representative trajectories for "Pothole + Rough"; (c) representative trajectories for " Manhole + Raveling"; and (d) representative trajectories for "Uneven surface". 160

7.6 Results of the trajectory clustering analysis on online map: (a) representative trajectories in the small area (b) overall trajectory clustering result. 161

List of Tables

2.1 Natural frequencies and damping ratios identified from the four data sets. 13

2.2 Natural frequencies computed from the initial FE model and the MAC values between the identified and computed mode shapes. 20

3.1 Physical parameters selected for the model updating for the bridge and the optimized updating parameters. 34

3.2 Identified, initial, and updated natural frequencies and the MAC values between the identified and updated mode shapes. 37

3.3 Updated natural frequencies and MAC values between the identified and updated mode shapes with the two desired MAC levels (0.7 and 0.8). 42

3.4 Comparison of the results in updating with cluster analysis and without cluster analysis. 58

4.1 Statistical results of the posterior samples and uncertainty reductions after Bayesian model updating (the standard deviations of the prior PDFs is 0.3). 86

4.2 Natural frequencies and the MAC values of the FE model after Bayesian model updating. 91

5.1 Variation in the natural frequencies associated with the thermal effects using thermal prestress and temperature-dependent Young's modulus. 101

6.1 Comparison between the vibration-based and image-based approaches. 115

Acknowledgments

I would first like to express my sincere gratitude to my advisor, Prof. Andrew W. Smyth, for his great support and mentorship during my graduate studies. He has nurtured me to explore various interesting and innovative topics by sharing his knowledge, insight, and expertise. His belief in me has been strong momentum for me to enthusiastically get involved in research and projects. In addition to all of the intellectual interactions with him, he also has encouraged me to be a generous and open-minded person.

I would also like to gratefully acknowledge the other members of my dissertation committee: Raimondo Betti, George Deodatis, Haim Waisman, and Nicolas Chbat. I greatly appreciated their time and effort to provide constructive comments and insightful observations.

I must also mention faculty members at Kookmin University where I got my undergraduate degree: Prof. Youngki Lee, Doobyong Bae, Sokhwan Choi, Kee Jeung Hong, and Chang Kook Oh. They have provided invaluable guidance and mentoring support that enabled me to successfully initiate my graduate studies.

My research was funded by the Department of Civil Engineering and Engineering Mechanics and National Science Foundation under CMMI-1200859 and CMMI-1100321. It was also partially funded by vibration monitoring projects from the Metropolitan Museum of Art, Penn museum, and New-York Historical Society.

I would also like to thank my colleagues in the department for their friendship

and intellectual support: Adrian, Suparno, Luc, Patrick, Raphael, Thalia, Audrey, Sung-Hwan, Sang Guk, Seonhong, Mostafa, Hao, Juan, Christos, Athina, Jenny. I also should mention Kristof, a visiting scholar from KU Leuven, for intellectual interaction and introducing various Belgium beers as well. There are also colleagues I met during my internship at Philip Research North America: Hao-yu, Yong, Dave, and Rohit. They helped me to explore new technologies in other fields of engineering.

Lastly, I would like to thank my parents for their unconditional support and love, which have filled my life with courage and pride to go for things that I have never done before. There is my wife, Ji Young Bae, who always has been staying by my side and being an amazing cheerleader during my studies. There is one more thing, my son, Roy Jang, who was joined my family during my PhD studies and gave me one more reason to go through this process with a great deal of motivation.

To Ji Young Bae and Roy Jang

Chapter 1

Scope

In the last few decades, the advances in sensing and wireless technologies have enabled one to measure a wide variety of data from infrastructure systems under operational conditions. In-depth data analytics on a variety of measurements can lead to the extraction of information about the current conditions of infrastructure, which can be a practically valuable resource for the maintenance of infrastructure. Although a great deal of attention has been paid to efforts to develop robust algorithms for the assessment of infrastructure conditions, most of them have some limitations and therefore more study is needed to further develop an existing methods or to introduce a new innovative framework.

This dissertation explores data analytics approaches to vibration response measurements from a bridge and road networks. Vibration responses measured from a major long-span bridge are used to study temperature effects on natural frequencies and to investigate both deterministic and probabilistic model updating approaches. With the use of vibration responses of multiple vehicles over road conditions and GPS positioning data, a new framework is developed to collect road surface condition data for the pavement distress management system.

1.1 Dissertation Outline

1.1.1 Structural Health Monitoring

Chapters 2, 3, 4, and 5 address the topic of structural health monitoring (SHM), which is an emerging technology that diagnoses the state of health of civil structures by leveraging homogeneous or heterogeneous measurements of structures. The primary goal of SHM is to detect, quantify, and/or localize structural damage which can be caused by extreme loading conditions or the aging of structures. Many researchers have made and are making a tremendous effort in developing a robust data analytics approach to extract valuable information for structural management systems. One of the popular approaches in SHM is a vibration-based damage detection technique, which utilizes dynamic responses of structures to detect structural damage. The main idea of this technique is that structural damage alters the global stiffness of structures and thus changes the characteristic of the dynamic behavior of structures. When processing vibration measurements, a major focus is, in general, placed on the extraction of modal parameters such as natural frequencies, damping ratios, and mode shapes since they characterize the dynamics of structures. Moreover, modal properties are one of the widely-used damage sensitive features in vibration-based damage detection techniques. It has been widely acknowledged that changes in natural frequencies provide useful information to detect structural damage and changes in mode shapes bear useful information to localize structural damage (Balmès, Basseville, Mevel, & Nasser, 2009). In general, mathematical and/or computational models are incorporated with measurements of structures to describe the dynamic behavior of a structure. These models are also used to study the correlations between structural damage and structural dynamic behavior. They are also used to predict how structure will behave

under extreme loading conditions. The accuracy of models plays a significant role in structural condition assessment and predictions of the dynamic behavior of structures.

In the last few decades, the model updating technique has gained a great deal of attention in the SHM community due to its great potential to localize and quantify structural damage. Model updating based on vibration response measurements is a technique that reduces inherent modeling errors in a finite element (FE) model that arise from simplifications, idealized connections, and uncertainties with regard to material properties. An updated FE model, which has fewer discrepancies with measurements, provides a more robust prediction of a structural behavior under operating and hazardous conditions. In this dissertation, measured vibration responses of a major long-span bridge and a full-scale FE model of the bridge are used to explore various model updating techniques and to study temperature effects on natural frequencies.

Chapter 2 describes an ambient dynamic test conducted on a large suspension bridge and the development of a full-scale FE model. In general, an ambient dynamic test is the most feasible and therefore popular in many civil applications since a specific input excitation device, which might induce damage during a test and would lead to an added cost, is not necessary. In this chapter, operational modal analysis is carried out based on real ambient vibration measurements to identify modal properties of the bridge considered here. In addition to identified modal properties, a full-scale FE model of the bridge is developed. The FE model is further modified via both deterministic (Chapter 3) and probabilistic (Chapter 4) model updating approaches to minimize discrepancies between the identified modal properties and those from the FE model. An updated FE model, whose physical parameters are tuned to minimize the discrepancies, is used to study temperature effects on natural frequencies in Chapter 5 since the variations in natural frequencies were observed with real measurements,

which are mostly due to the environmental effects.

In Chapter 3, sensitivity-based model updating, which belongs to a deterministic approach, is demonstrated with four model updating exercises. This chapter focuses on the trade-off between natural frequency and mode shape agreements and parameterization of a full-scale FE model. A method that adjusts the level of mode shape agreements is suggested, which imposes nonlinear constraints during an optimization process. The innovative sensitivity-based clustering method for parameterization in a model updating problem, which has not been used in any civil application, is adopted and applied to a full-scale model to validate its robustness to determine efficient and physically meaningful updating parameters. Updating parameters determined by this method include physical parameters having similar effects on targeted natural frequencies. This chapter provides the interpretation of the physical meanings of clustered parameters, which can be a practically-important finding for structural engineers.

In Chapter 4, a full-scale FE model is updated using the Bayesian model updating framework, one of the popular probabilistic model updating approaches. Bayesian model updating of a full-scale FE model is challenging due to its large number of degrees-of-freedom and physical parameters. Therefore, there are limited studies that address Bayesian model updating of a full-scale FE model. However, in real-life applications, a full-scale model is widely used in structural management systems. In this chapter, an effort has been made to extend the applicability of Bayesian model updating to a more complex and realistic updating problem. This chapter provides the theoretical background of Bayesian model updating. In order to circumvent the calculation of multi-dimensional integrations, which is involved during the Bayesian model updating procedures, the hybrid Monte Carlo sampling method is used. This sampling method has a robust capability to deal with the high dimensionality. Uncer-

tainties of updating parameters and uncertainty propagations to natural frequencies and mode shapes are estimated based on posterior samples.

Chapter 5 investigates temperature effects on natural frequencies. The variations of the identified modal properties in Chapter 2, are observed, which have motivated the study of temperature effects on natural frequencies. An updated FE model, whose physical parameters are tuned using the sensitivity-based model updating method (Chapter 3) and therefore having a better consistency with the measurements, is used to conduct a controlled simulation-based study to investigate the effects of spatial temperature variations on natural frequencies. An understanding of temperature effects on natural frequencies is fundamentally important in vibration-based damage detection techniques when modal properties are used as damage sensitive features. Civil structures are subjected to various operational and environmental conditions. Modal properties of structures also can be changed by operational and environmental conditions in addition to structural damage. An understanding of how the modal properties of structures are related to the environmental and operational conditions can help improve the reliability of the vibration-based damage detection techniques by discriminating normal changes of modal properties due to environmental conditions from changes due to structural damage. In this chapter, a method that generates spatial variations of temperatures over a bridge is developed. Thermal prestress modeling is used to simulate thermal effects on natural frequencies. Based on simulated data sets (frequencies versus temperatures), the relationships between natural frequencies and temperatures are modeled using various regression models.

1.1.2 Road Surface Monitoring

Chapters 6 and 7 introduce a new framework for pavement distress data collection. In road surface condition monitoring, the current state-of-the-art technology uses data collection vehicles that are equipped with various sensors to automatically collect pavement distress data. These vehicles are able to collect network-level pavement data in an operating condition and at highway speed. Laser, acoustic, infrared sensors are used to obtain profiles of road surfaces. Area scanning, line scanning, and 3-D laser imaging are used for pavement distress recording. Due to the high cost of the current automated data collection practice, pavement distress data are collected periodically. However, there is a practical need to collect data more frequently, especially for street defects such as potholes and sunken manholes, which in general develop quickly compared to the other pavement distresses such as cracking and rutting. A framework of data acquisition and system integration introduced in Chapter 6 and 7 aims to provide up-to-date information for pavement distress management. The proposed system is of practical importance since it provides continuous information about road conditions, which can be valuable for pavement management systems and/or public safety.

Chapter 6 explains the architecture of the suggested system and embedded data processing algorithms (data logging and street defect detection algorithms). In the suggested system, vibration responses of vehicles and positioning data are collected from mobile data collection kits mounted on multiple vehicles. In each mobile data collection kit, a triaxial accelerometer and global positioning system (GPS) sensor collect data that can be used for the detection of isolated pavement distresses and rough road surfaces. A local data logging algorithm is embedded in each vehicle client to increase the efficiency of a local data logging process and to perform a preliminary

evaluation based on predetermined thresholds. At a back-end server, the street defect detection algorithm, which relies on the supervised machine learning technique, is implemented to classify collected data into three different categories of road surface conditions.

Chapter 7 explains the trajectory clustering technique, which is a data mining approach to extract compacted information from massive trajectory data. This technique is practically significant because there is a need to process tremendous trajectory data which recently have become available due to the advances in sensing technology. Trajectory clustering aims to group trajectory data based on their locations and moving directions using a specific inter-vector distance calculation. This chapter starts with a brief overview of trajectory clustering. This is followed by detailed explanations about how distances between trajectories are calculated and how representative trajectories are estimated based on trajectories belonging to the same cluster. Then, trajectory clustering is applied to the classification results demonstrated in Chapter 7, which are indeed trajectory data since each collected data set consists of a classification result and a sequence of GPS positioning data points. Trajectory clustering is able to integrate the classification results from multiple vehicles and to draw compact trajectory representations, which can be readily visualized and interpreted.

Part I

Structural Health Monitoring

Chapter 2

Operational Modal Analysis and a Full-Scale FE Model of a Large Suspension Bridge

When identifying model properties of structures, ambient dynamic testing is generally the most feasible and therefore popular test method since there is no need for a specific excitation device which might induce damage and would lead to added cost. Operational modal analysis (OMA), which is also known as an ambient modal identification, is the identification of modal properties of structures under operational conditions, where input forces are considered to be unknown. Modal properties such as natural frequencies, damping ratios, and mode shapes are extracted from ambient vibration responses in the time or frequency domain. Various OMA approaches have been developed and have become available. Reynders (2012) has extensively reviewed various OMA approaches and compared them with each other. This chapter starts with an overview of the Enhanced Frequency Domain Decomposition method, which is used in this study to identify modal properties of a large suspension bridge. This

is followed by a description of an ambient dynamic test conducted on a bridge and modal properties identified from ambient vibration measurements. Then, the development of an initial FE model is demonstrated. This FE model is used to study the model updating techniques in Chapters 3 and 4 and temperature effects on natural frequencies in Chapter 5.

2.1 Overview of the Enhanced Frequency Domain Decomposition Method

The Enhanced Frequency Domain Decomposition (EFDD) method (Brincker, Ventura, & Andersen, 2001) is one of the popular Operational Modal Analysis (OMA) techniques. It is used to identify the modal properties of structures vibrating due to ambient forces such as traffic and wind. The main assumption of this methods is that input forces are broadband random and structures are lightly damped. It is also assumed that structures behave in an elastic range since the environmental forces are not big enough to push structures into a plastic range. In order to more accurately identify modal properties, monitoring is usually conducted for a long period of time to have a large enough of data.

In this method, power spectral density (PSD) matrices $Gyy(\omega)$ are first computed at all discrete frequency domains. Their diagonal elements are power spectral densities. Their off-diagonals values are cross spectral densities (CSD). The size of the PSD matrix is the same as the measured degrees-of-freedom (DOFs). Once PSD matrices are estimated, the Singular Value Decomposition (SVD) method is applied to the PSD matrices to orthogonalize dynamic modes. The PSD matrices can be

expressed after the SVD as follows:

$$Gyy(\omega) = \mathbf{\Phi \Sigma \Phi}^H, \tag{2.1}$$

where the superscript H denotes a Hermitian transformation; $\Sigma \in \mathbb{R}^{n_m \times n_m}$ is a singular value matrix; and $\Phi \in \mathbb{C}^{n_m \times n_m}$ is a singular vector unitary matrix. n_m is the number of measured DOFs. The singular value matrix $\mathbf{\Sigma}$ and the singular vector matrix $\mathbf{\Phi}$ are be expressed as:

$$\begin{aligned} \mathbf{\Sigma} &= diag(s_1, s_2, s_3, \ldots, s_{n_m}) \\ \Phi &= [\phi_1, \phi_2, \phi_3, \ldots, \phi_{n_m}] \end{aligned} \tag{2.2}$$

In the EFDD technique, a single-degree-of-freedom (SDOF) CSD function, which corresponds to a single dynamic mode, is used to identify a natural frequency, a damping ratio, and a mode shape. A SDOF CSD function is estimated based on the Modal Assurance Criterion (MAC) values (Allemang & Brown, 1982) between a singular vector corresponding to a peak value and singular vectors at all discrete frequency points. The MAC value between ϕ_i and ϕ_j is defined as follows:

$$\text{MAC}(\phi_i, \phi_j) = \frac{|\phi_i^H \phi_j|^2}{\phi_i^H \phi_i \ \phi_j^H \phi_j}. \tag{2.3}$$

Then, the MAC rejection level is used to determine whether singular values belong to the same dynamic mode. If the MAC values at some discrete frequency points are bigger than the MAC rejection level, the singular values and vectors are assigned to the same SDOF CSD function, which is also called a bell-shaped SDOF function. By taking the inverse Fourier transformation of the SDOF CSD functions, SDOF auto-correlation functions are obtained and used for the identification of model properties. Natural frequencies are calculated based on the linear fitting of the zero crossing num-

ber versus time. Damping ratios are obtained from the logarithmic decrement. Mode shapes are the weighted average of the singular vectors belonging to the same SDOF CSD function. The MAC values associated with singular vectors or corresponding singular values (power density) can be weighting factors in the estimation of mode shapes. Complex-numbered singular vectors are, in general, required to be rotated in order to be situated along the real axis of a polar plot. The rotational angle can be a value such that minimizes angular distances between the real axis and the singular vector.

2.2 Ambient Dynamic Test on a Large Suspension Bridge

An ambient dynamic test was conducted on a large suspension bridge. It was a double-deck steel structure with two towers, three spans, and four suspension cables. Its total length is 2089 m. The main span is 451 m long, and each suspension cable is 982 m long. Tri-axial accelerometers were deployed at nine different locations, recording data at a sampling frequency of 200 Hz. The total measured DOFs were 27. During the test, the bridge was in an operational condition and vibrated due to the environmental forces. One sensor was placed at the top of the tower. Another one was located at one of the side spans of the bridge. The other accelerometers were placed on the main span. During a day, four hour-long data were selected to be recorded per day. Data recording started at various representative timestamps during a day, which are morning rush hours (8AM), evening rush hours (5PM), midday time (12PM), and night time (3AM). These four time zones are selected because they can be representative for different ambient excitation conditions such as temperature and

amount of traffic. In this study, the four sets of measurements which were recorded on the same day, but at four different time zones, are used. PSD matrices are calculated using Welch's method with a Hamming window envelope and 66.7% overlapping. Then, PSD matrices are decomposed into singular values and vectors using the SVD method. The first singular values corresponding to 3AM, 8AM, 12PM, and 5PM data sets are shown in Figure 2.1.

The EFDD method (Brincker et al., 2001) was used to identify the modal properties of the structure under consideration here based on the first singular values and vectors of the PSD matrices. More interest was placed on predominant global vibration modes whose natural frequencies were below 1 Hz. The natural frequencies and mode shapes corresponding to the first seven dynamic modes were defined as targets in model updating exercises considered in Chapters 3 and 4. The identified natural frequencies of these modes from the four different time zones are summarized in Table 2.1. Variations in the identified natural frequencies were observed during a single day, which were more dominant for the first few lower modes. The observed frequency variations can be due to operational and environmental conditions such as temperature and amount of traffic. Temperature effects on natural frequencies are

Table 2.1: Natural frequencies and damping ratios identified from the four data sets.

Mode		Natural Frequency [Hz]				
		3AM	8AM	12PM	5PM	Mean
H1	First lateral	0.2060	0.1877	0.1969	0.1847	0.1938
V1	First vertical	0.2361	0.2232	0.2267	0.2214	0.2269
V2	Second vertical	0.3065	0.3000	0.3054	0.2993	0.3028
T1	First torsional	0.3740	0.3720	0.3731	0.3740	0.3733
SV1	First side-span vertical	0.3350	0.3390	0.3422	0.3335	0.3374
H2	Second lateral	0.4531	0.4501	0.4502	0.4475	0.4502
V3	Third vertical	0.5075	0.4950	0.4969	0.4990	0.4996

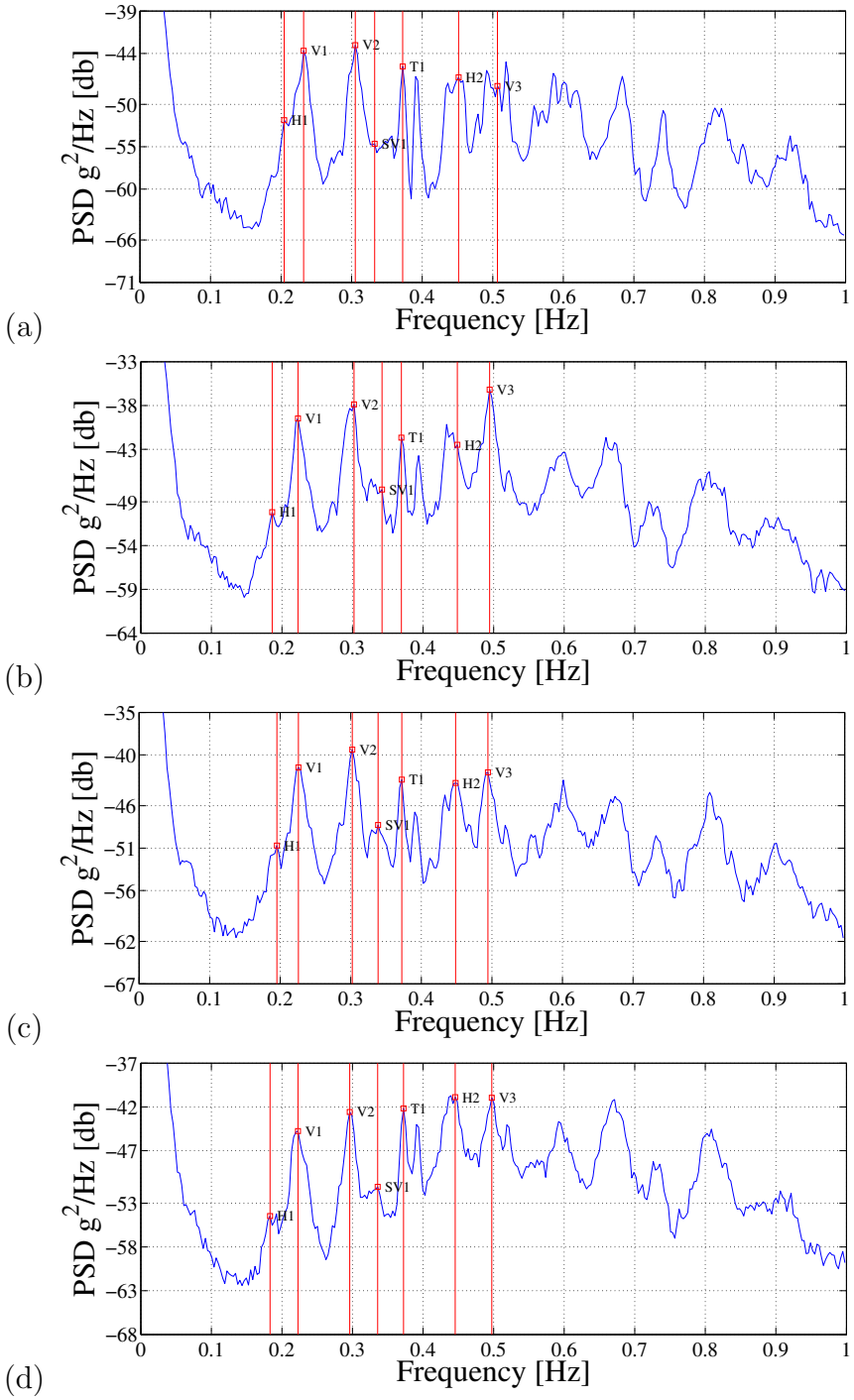

Figure 2.1: The first singular values of the PSD matrices for four data sets: (a) 3AM data set; (b) 8AM data set; (c) 12PM data sets; and (d) 5PM data sets.

demonstrated in Chapter 5.

The 3D representations of the identified mode shapes, which are the average of the four sets of mode shapes from the different time zones, are plotted in Figure 2.2, in which the red dots denote the locations of accelerometers. The magnitudes of the mode shapes at the sensor locations were identified based on the real measured data. The other magnitudes (the blue lines) were interpolated. The sensors on the symmetrical locations along the longitudinal direction were used to determine whether the identified mode shapes were symmetric or not. The sensors placed on the both ends of the deck along the same longitudinal location are used to see whether the mode shapes of the deck had in-phase or out-of-phase motions. Based on the symmetricity and in-phase or out-of-phase motions of the mode shapes, the modal displacements at the sensor locations were projected to the other side of the bridge along the longitudinal and traversal directions. Then, the projected modal displacements, modal displacements at the sensor locations, and the boundary conditions were used for the interpolation of the identified mode shapes. In Figure 2.3, identified mode shapes were presented in the polar plots. The identified mode shapes were mainly along the real axises, which means there were no significant complex mode shapes. Figure 2.4 shows the AutoMAC matrix of the identified mode shapes to present the spatial independence.

2.3 Initial FE Model of a Bridge

In addition to the identified modal properties, an FE model is developed to study temperature effects on natural frequencies and the model updating techniques. Creating precise FE models of bridges is not in general an easy task. In order to have a very precise model, reasonable assumptions and good engineering judgment are

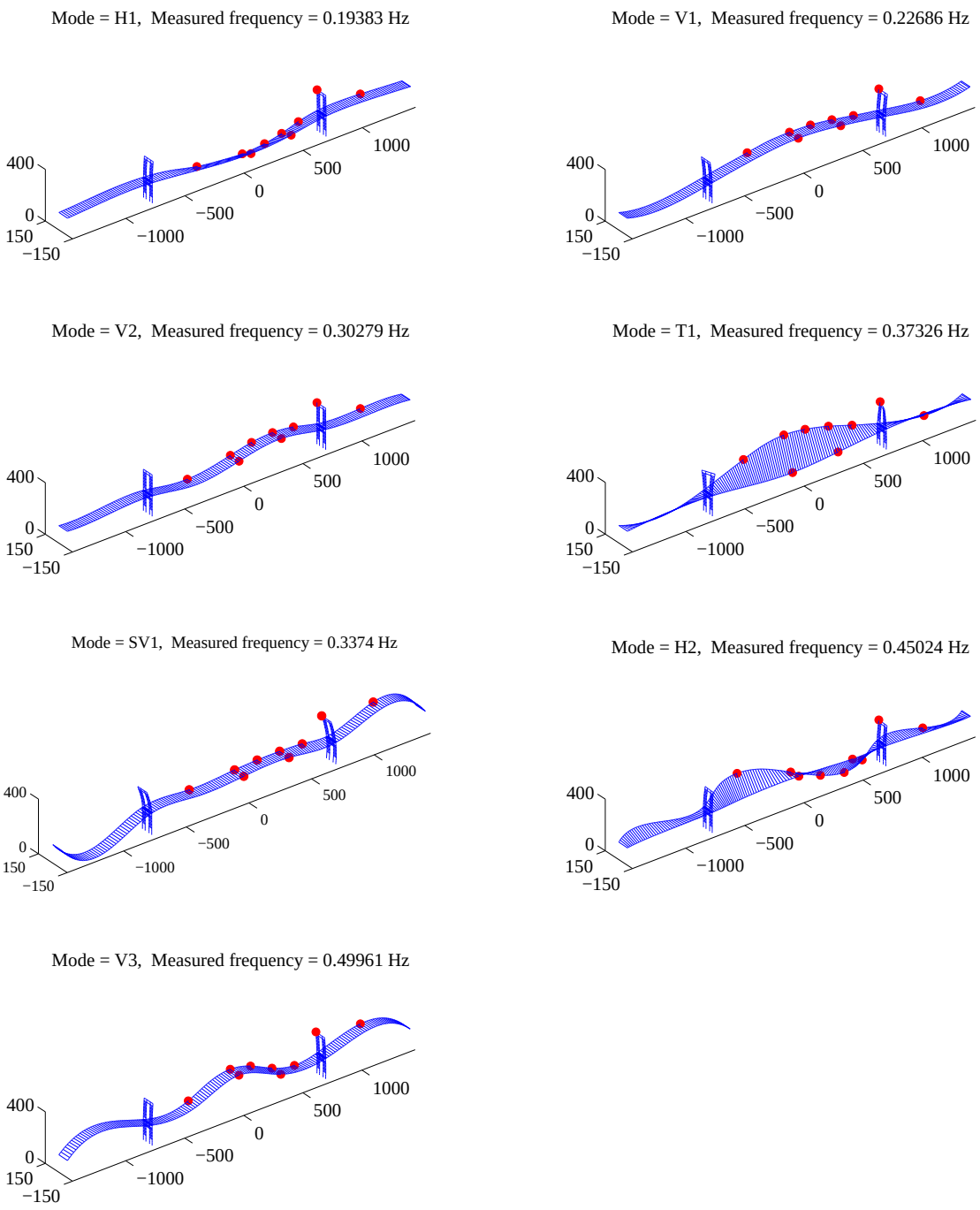

Figure 2.2: Identified mode shapes from the measured data.

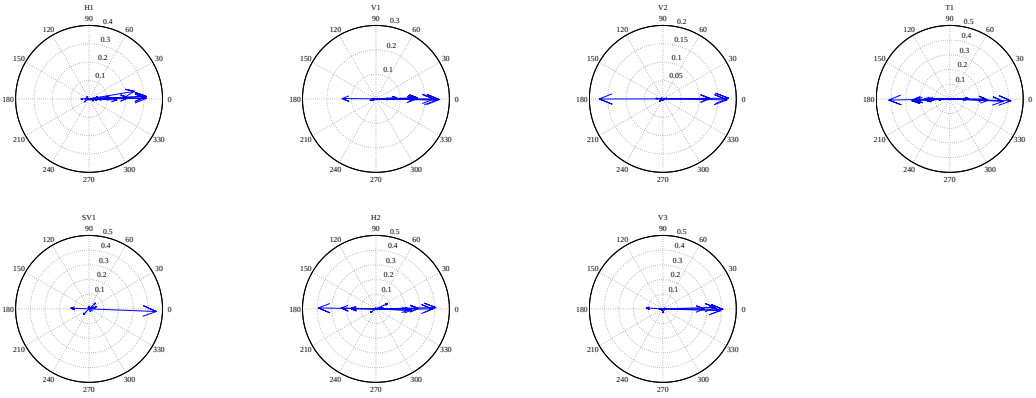

Figure 2.3: Polar plots for mode shapes.

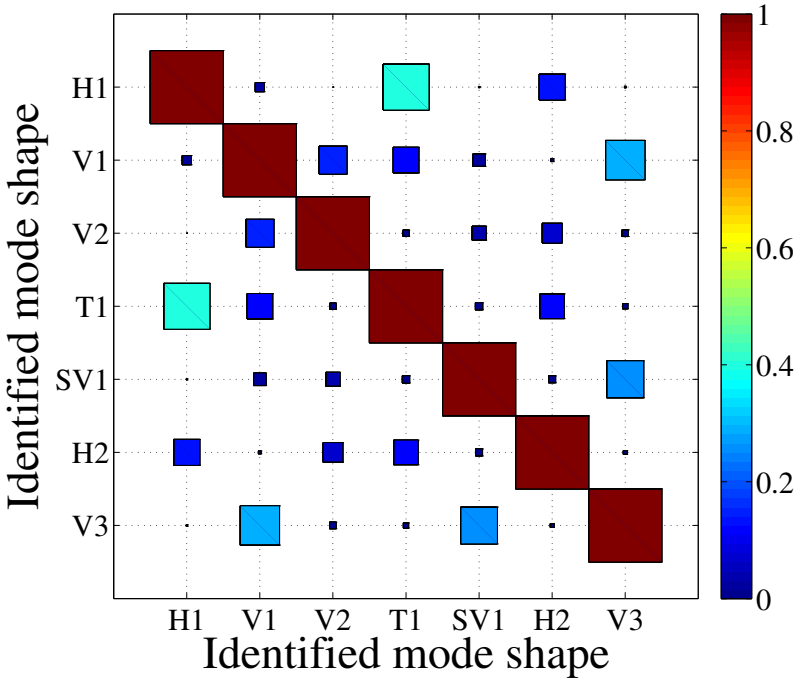

Figure 2.4: AutoMAC matrix of the identified mode shapes.

necessary. One must decide which element types should be used, how many degrees-of-freedoms should be considered for each element, and whether the size of meshes is dense enough or not. Since there are many bolted and welded connections between structural components, it is essential to decide whether pin-connections or rigid connections are suitable for various connections in the FE model. A great deal of information about the details of bridges such as the dimension of cross sections, the geometry of structures, and the material property of structural components should be provided to develop a precise FE model.

The initial FE model of the suspension bridge under consideration here was developed using ABAQUS (*ABAQUS/CAE user's manual : version 6.4*, 2003), which is shown in Figure 2.5. Based on only partial design drawings of the bridge, the geometry of the FE model was carefully prescribed. Since it was not modified during updating, very careful attention was paid to its original definition in the FE model. The information about the dimension of the cross sections was somewhat limited. When information was lacking, reasonable guesses were made based on photographs. For the structural components whose information was available, the cross-sectional area and the bending moment of inertia of the steel sections were calculated based on the drawings. For the physical parameters of the structural components, the material

Figure 2.5: Initial FE model of a large suspension bridge.

properties of A36 steel was used. The mass density (ρ) was 7800 kg/m^3. The Young's modulus (E) was 200 GPa. The Poisson's ratio was 0.26.

For the element types in the FE model, the suspension cables and the suspenders were modeled with truss elements with no capability of carrying compression forces. Beam elements with six degrees-of-freedoms (DOFs) were used for chords, floor beams, columns, trusses, and lateral bracings. In the FE model, there were 19632 beam elements, 1464 truss elements, and 18614 nodes. Nonstructural components such as asphalt layers, pedestrian walks, and subway rails were not included. The steel sections were connected by bolted and welded connections so that it was necessary to decide whether they were pin-connected or rigidly connected in the model. The suspenders were pin-connected to the bottom chords of the deck as mentioned in the design drawings. Pinned-connections between the lateral bracing elements and the chords were used. The columns and the floor beams were rigidly connected to the chords.

The influence of the soil was taken into account in the FE model. Translational and rotational linear springs in the three directions (vertical, transverse, and longitudinal) were located at the bottom of the tower pylons and at the end of the deck. Only translational springs in the longitudinal direction were applied to the end of the suspension cables. Hinges were also included in the FE model to release some DOFs due to thermal movement (Caltrans, 2012). A typical hinge model (Priestley, Seible, & Calvi, 1996) was used to provide freedom to rotate about the transversal and vertical direction. The longitudinal forces in the hinge elements were released in order to give freedom to move when there was an out-of-phase movement in the expansion joints. After releasing the DOFs, rotational springs were added at the hinge location. The initial coefficients for the soil springs were 7.30 GN/m for translational springs and 0.68 $GN{\cdot}m/rad$ for the rotational springs. By trying several different numbers for

the spring coefficients, the initial values were chosen such that the natural frequencies of the FE model were reasonably close to the identified ones.

Natural frequencies calculated from the initial FE model are shown in Table 2.2. Initially, the natural frequencies of the initial FE model were mostly higher than the identified natural frequencies. This could be due to the omission of non-structural components, the idealization of connections, and/or incorrect values of the initial physical parameters. Furthermore, the information about the dimensions of cross sections was somewhat limited, thus producing more modeling errors in the initial FE model. In practice, it is desirable to develop an initial FE model as precisely as possible to achieve the best model updating result because such a model can provide a better starting point for a given updating problem. The MAC value is used here to show the correlation between the identified mode shapes and those from the FE model. The MAC value ranges from 0 to 1, and when two mode shapes are identical, the MAC value becomes unity. The MAC values between the identified and computed mode shapes are shown in Table 2.2.

Table 2.2: Natural frequencies computed from the initial FE model and the MAC values between the identified and computed mode shapes.

Mode		Natural Frequency	MAC value			
		Hz				
		Initial FE model	3AM	8AM	12PM	5PM
H1	First lateral	0.2340	0.9826	0.9821	0.9818	0.9755
V1	First vertical	0.2940	0.9641	0.9665	0.9554	0.9679
V2	Second vertical	0.3520	0.9435	0.9553	0.9509	0.9428
T1	First torsional	0.3840	0.7429	0.8082	0.7720	0.7824
SV1	First side-span vertical	0.4520	0.8448	0.8234	0.8674	0.8186
H2	Second lateral	0.5390	0.8502	0.8343	0.8467	0.8562
V3	Third vertical	0.5980	0.8683	0.8561	0.8584	0.8622

Chapter 3

Sensitivity-based Model Updating

FE models are widely used in structure management systems to simulate the dynamic behavior of structures not only under day-to-day operating conditions, but also under extreme and hazardous loading conditions. However, the dynamic characteristic of an FE model might differ from those identified from measurements of a structure. An FE model whose dynamic characteristic is different from a real structure might fail to produce a reliable prediction. As can be seen in Chapter 2, the modal properties of an initial FE model are quite different from the identified natural frequencies since the FE model is developed based on only partial design drawings. The primary focus of model updating is to identify physical properties of an FE model which minimize discrepancies between the measurements of a real structure and the corresponding outputs of an FE model. An updated FE model, which has less discrepancies with measurements, can provide more physically meaningful insights for the physical parameters of structural components and can make more reliable predictions under various loading conditions.

3.1 Introduction

FE models are widely used to predict the dynamic behavior of structures. However, the performance of the prediction is questionable when there are relatively large differences in modal properties (natural frequencies, damping ratios, and mode shapes) between an FE model and a real structure. Although an FE model may be carefully developed based on precise technical design data and best engineering judgment, there are inevitable modeling errors in an FE model due to simplifications and idealized connections. Uncertain geometry, material properties, and boundary conditions also present challenges in developing a highly accurate FE model.

Model updating is a technique that tunes FE models to match with measured data. It is of significant practical importance due to the need for decreasing inevitable modeling errors in FE models and the potential possibility of detecting damage in structures. Although it was originally developed in the mechanical and aerospace engineering fields, in the last decade it has been applied to civil structures such as bridges (Q. Zhang, Chang, & Chang, 2001; Brownjohn & Xia, 2000; Brownjohn, Moyo, Omenzetter, & Lu, 2003; Reynders, Teughels, & De Roeck, 2010; Teughels & De Roeck, 2004; Mosquera, Smyth, & Betti, 2012), footbridges (Živanović, Pavic, & Reynolds, 2006, 2007; Moaveni & Behmanesh, 2012), and buildings (Moaveni, Conte, & Hemez, 2009; Bakir, Reynders, & De Roeck, 2007, 2008). In these applications, it has been very successful at tuning the physical parameters of FE models to produce fewer discrepancies between updated and identified modal properties. It subsequently becomes possible to more reliably predict the dynamic behavior of structures. Some authors (Reynders et al., 2010; Teughels & De Roeck, 2004; Bakir et al., 2007) have successfully pinpointed the location of the damage based on their damage scenarios by model updating. A summery for model updating can be found in (Mottershead,

Link, & Friswell, 2011).

Model updating techniques can be classified into two categories (one-step methods and iterative methods) (Levin & Lieven, 1998). One-step methods, which are also called global methods, directly modify the global mass and stiffness matrices. One of the drawbacks of this methods is that the symmetry, positive-definiteness, and sparseness of the global matrices are often violated. The other drawback can be that such an approach is not appropriate when mass and stiffness matrices are coupled (Q. Zhang et al., 2001). For example, it is not suitable for a suspension bridge because the weight of the suspension bridge is related to both mass and global stiffness. In iterative methods (local methods), the physical parameters of FE models are tuned so that FE models can preserve the above-mentioned characteristics of the global mass and stiffness matrices. As a result, FE models remain physically meaningful.

Sensitivity-based model updating is one of the most popular and successful model updating methods (Mottershead et al., 2011), which belongs to the iterative methods. The main benefit of this method is that the relationship between modal properties and physical parameters becomes more clear through an in-depth sensitivity analysis. During a sensitivity analysis, it can be determined which physical parameters have a significant effect on the dynamic characteristics of structures and which natural frequencies are altered with respect to certain physical parameters.

Model updating is typically framed as an optimization problem in which discrepancies between an FE model and a real structure are minimized. One should carefully consider which optimization algorithm is appropriate a problem based on the smoothness and nonlinearity of objective functions. The interior point method can be a suitable solver because objective functions in model updating are usually smooth and convex near optimal solutions (Moaveni & Behmanesh, 2012). It also has

the desirable capacity to deal with not only the nonlinearity of objective functions, but also the nonlinearity of constraint equations in an optimization problem. Compared to global optimization algorithms, it is not computationally expansive since it is a gradient-based optimization.

The ideas of using the regularization (Friswell, Mottershead, & Ahmadian, 2001) and parameter clustering (Shahverdi, Mares, Wang, & Mottershead, 2009) techniques in model updating are adapted and applied to an updating problem of a bridge model. In this paper, nonlinear constraints are placed on agreements between identified mode shapes and computed ones from an FE model to control those agreements. The sensitivity-based clustering method, which is developed by Shahverdi et al. (Shahverdi et al., 2009) for parameterization in model updating, is applied to a bridge model to find efficient and physically meaningful updating parameters based on the sensitivities of natural frequencies with respect to both mass and stiffness-related physical parameters. The physical meanings of selected updating parameters are also demonstrated.

This chapter is focused on improving mode shape matches with a nonlinear inequality constraint equation and selecting more efficient updating parameters based on sensitivities of natural frequencies corresponding to physical parameters. The chapter is organized as follows. In Section 3.2, the theoretical background of model updating is explained. Section 3.3 provides an overview of the interior point method that is used in this chapter to solve an optimization problem in model updating. In Section 3.4, the FE model of the large suspension bridge is developed and tuned to match the identified modal properties from the dynamic test. In Section 3.5, a nonlinear constraint equation is introduced to regulate the errors in updated mode shapes. In Section 3.6, cluster analysis is conducted to find a better updating parameter. In Section 3.7, conclusions are made.

3.2 Sensitivity-based Model Updating Procedures

In model updating, physical parameters in a FE model are tuned so that natural frequencies and mode shapes from an FE model match with those from measured data. Physical parameters can be Young's modulus, mass density of the materials, and/or spring coefficients. They directly impact natural frequencies and mode shapes of an FE model. The relative changes in the physical parameters are selected as updating parameters. In each element e, the modified physical parameter (X^e) of element e is defined as:

$$X^e = X_0^e \left(1 - \theta^e\right), \tag{3.1}$$

where X_0^e is an initial value for a physical parameter of element e and θ^e is an updating parameter for element e. Model updating is here an inverse problem in which the optimal values of updating parameters are computed to minimize the errors in natural frequencies and mode shapes between an FE model and a real structure. The objective function in this optimization problem includes the residual vectors of natural frequencies and mode shapes. The objective function to be used here in model updating is defined as:

$$\min_{\theta} \quad f(\theta) = \frac{1}{2}\Big(\|\mathbf{r_f}(\theta)\| + \|\mathbf{r_s}(\theta)\| \Big)^2, \tag{3.2}$$

where $f\colon \mathbb{R}^{n_p} \to \mathbb{R}$, $\mathbf{r_f}\colon \mathbb{R}^{n_p} \to \mathbb{R}^{n_t}$, $\mathbf{r_s}\colon \mathbb{R}^{n_p} \to \mathbb{R}^{n_m}$ and $\|\cdot\|$ denotes the Euclidean norm. $\mathbf{r_f}$ is a natural frequency residual vector. $\mathbf{r_s}$ is a mode shape residual vector. n_p and n_t are the number of updating parameters and of dynamic modes considered in updating (targeted dynamic modes), respectively. n_m is equal to the product of the number of targeted dynamic modes and the number of degrees-of-freedoms of the

mode shapes. The natural frequency residual vector ($\mathbf{r_f}$) represents the relative errors in natural frequencies. It is defined as:

$$r_f^i(\theta) = \frac{f_i(\theta) - \tilde{f}_i}{\tilde{f}_i}, \tag{3.3}$$

where $\widetilde{f_i}$ and f_i are identified and computed natural frequencies in Hz, respectively. The residual mode shape vector ($\mathbf{r_s}$) is expressed as:

$$\mathbf{r_s}^i = \text{MSF}\left(\phi_i(\theta), \frac{\tilde{\phi}_i}{\tilde{\phi}_i^{\,r}}\right)\phi_i(\theta) - \frac{\tilde{\phi}_i}{\tilde{\phi}_i^{\,r}}, \tag{3.4}$$

where $\tilde{\phi}_i$ and $\phi_i(\theta)$ are respectively identified and computed mode shape vectors. $\tilde{\phi}_i^{\,r}$ is a reference value, which is the maximum component of the vector $\tilde{\phi}_i$. Since computed mode shapes have a different scale compared to identified mode shapes, the modal scale factor (MSF) is used to change the scale of the computed mode shapes $\phi_i(\theta)$ to minimize the difference with the maximum normalized identified mode shapes in a least-squares sense (Allemang & Brown, 1982). The MSF is defined as:

$$\text{MSF}\left(\phi_i(\theta), \tilde{\phi}_i\right) = \frac{\phi_i^*(\theta)\ \tilde{\phi}_i}{\|\phi_i(\theta)\|^2}, \tag{3.5}$$

where $\square^*$ denotes a complex conjugate transpose. When calculating the residual vectors, it is important to make sure that comparison made between computed and identified natural frequencies were made with frequencies corresponding to the same dynamic mode (Mottershead et al., 2011). This procedure is called as mode paring. The MAC value (Allemang & Brown, 1982) is used in mode paring.

Sensitivity analysis is performed to determine how physical parameters in an FE model affect natural frequencies and mode shapes. Sensitivity analysis can be useful when choosing which updating parameters should be considered in the modification

of FE models. The modal sensitivity matrix with respect to the updating parameter θ_k can be analytically determined by the formulas of Fox and Kapoor (Fox & Kapoor, 1968).

$$\begin{aligned} \frac{\partial \lambda_j}{\partial \theta_k} &= {\phi^{\mathbf{T}}}_j \left[-\lambda_j \frac{\partial \mathbf{M}}{\partial \theta_k} + \frac{\partial \mathbf{K}}{\partial \theta_k} \right] \phi_j \\ \frac{\partial \phi_j}{\partial \theta_k} &= \sum_{h=1}^{H} a_{jkh} \phi_h, \end{aligned} \tag{3.6}$$

where H is the number of dynamic modes which are taken into account in calculating the approximation of mode-shape sensitivities. $\mathbf{M}$ and $\mathbf{K}$ are the FE mass and stiffness matrices. λ_j is jth eigenvalue ($\lambda_j = \omega_j^2$). The factor a_{jkh} is defined as:

$$a_{jkh} = \begin{cases} \frac{{\phi^{\mathbf{T}}}_h \left(-\lambda_j \frac{\partial \mathbf{M}}{\partial \theta_k} + \frac{\partial \mathbf{K}}{\partial \theta_k} \right) \phi_j}{(\lambda_j - \lambda_h)} & \text{if } h \neq j \\ -\frac{1}{2} \phi_j^T \left(\frac{\partial \mathbf{M}}{\partial \theta_k} \right) \phi_j & \text{if } h = j \end{cases} \tag{3.7}$$

The sensitivity matrix can also be calculate numerically by perturbing updating parameters with a small number and determining the differences in the predicted natural frequencies and mode shapes.

3.3 Overview of the Interior Point Method for Optimization

The interior point method (Byrd, Hribar, & Nocedal, 1999) is used to solve the optimization problem in model updating. It is a powerful tool to deal with large nonlinear programming problems. Model updating is a constrained optimization problem because bounds are established for physical parameters to remain in a realistic range. For example, it is unrealistic to have negative Young's modulus or mass density. As a

result, it is necessary to choose an optimization algorithm which can efficiently handle bounds. The interior point method can be appropriate. It can deal with bounds for parameters in an optimization because it includes a trust region method in the algorithm. Furthermore, it is able to handle nonlinearity in constraint equations and objective functions since it incorporates Sequential Quadratic Programming (SQP). One of the drawbacks of gradient-based methods can be that the result of optimizations can depend on initial points. This means that solutions might be caught in local minima and not able to find global minima. However, initial points in model updating are in general not that far away from an optimum solution because initial FE models whose modal properties are not vastly different from identified modal properties are used as initial points. Since the objective functions in model updating are usually smooth and convex near global minima (Moaveni & Behmanesh, 2012), solutions can converge to an optimum solution.

An overview of the interior point method for an optimization problem is provided here. A constrained nonlinear optimization problem can be expressed as

$$\begin{aligned} \underset{x}{minimize} \quad & F(x) \\ \text{subject to} \quad & H(x) = 0 \\ & G(x) \leq 0 \ , \end{aligned} \tag{3.8}$$

where $F\colon \mathbb{R}^r \to \mathbb{R}$, $H\colon \mathbb{R}^r \to \mathbb{R}^p$, $G\colon \mathbb{R}^r \to \mathbb{R}^q$. r is the number of variables. p and q are the number of the equality constraints and the inequality constraints, respectively. $F(x)$ is an objective function. $H(x)$ is an equality constraint equation. $G(x)$ is an inequality constraint equation. After applying a logarithmic barrier function

associated with the inequality constraint, the equation above becomes:

$$\begin{aligned} \underset{x,s}{minimize} \quad & F(x) - \mu \sum_{i=1}^{q} \ln s_i \\ \text{subject to} \quad & H(x) = 0 \\ & G(x) + s = 0, \end{aligned} \tag{3.9}$$

where μ and s are a barrier parameter and a slack variable, respectively. The optimal value x^* for the problem can be obtain by minimizing the Lagrangian defined as:

$$\mathcal{L}(x, s, \Gamma_h, \Gamma_g) = F(x) - \mu \sum_{i=1}^{q} \ln s_i + \Gamma_h^T H(x) + \Gamma_g^T (G(x) + s), \tag{3.10}$$

where $\Gamma_h \in \mathbb{R}^p$ and $\Gamma_g \in \mathbb{R}^q$ are the Lagrange multipliers for the equality constraints and the inequality constraints, respectively. The interior point method is an iterative method, where an approximated solution (x_k) converges to an optimal value x^* as more iterations are performed. At each iteration, subproblems are solved to obtain step vectors ($d_{x,k} = x_{k+1} - x_k$ and $d_{s,k} = s_{k+1} - s_k$) from the current iterates (x_k and s_k) and the Lagrange multipliers for the next iteration (Γ_h^+ and Γ_g^+). d_x, d_s, Γ_h^+ and Γ_g^+ are computed by solving the subproblem defined as:

$$\begin{bmatrix} \nabla^2_{xx}\mathcal{L}_k & 0 & A_h(x_k) & A_g(x_k) \\ 0 & \Sigma_k & 0 & I \\ A_h^T(x_k) & 0 & 0 & 0 \\ A_g^T(x_k) & I & 0 & 0 \end{bmatrix} \begin{bmatrix} d_x \\ d_s \\ \Gamma_h^+ \\ \Gamma_g^+ \end{bmatrix} = \begin{bmatrix} -\nabla F(x_k) \\ \mu S_k^{-1} e \\ -H(x_k) \\ -G(x_k) - s_k \end{bmatrix}. \tag{3.11}$$

In the matrix above, $e = [1, \ldots, 1]^T$ and $S = diag(s^1, \ldots, s^q)$. $A_h(x_k) \in \mathbb{R}^{p \times r}$ and $A_g(x_k) \in \mathbb{R}^{q \times r}$ are the gradients of the constraints. $\nabla F(x) \in \mathbb{R}^r$ is the gradient of the objective function $F(x)$. The Hessian matrix of the Lagrangian with respect

to d_x is defined to be $\nabla^2_{xx}\mathcal{L}_k \in \mathbb{R}^{r\times r}$. $\Sigma_k = \nabla^2_{ss}\mathcal{L}_k \in \mathbb{R}^{q\times q}$ is the Hessian of the Lagrangian with respect to d_s. It is also approximated as $\Sigma_k = \mu S_k^{-2}$ (primal method) or $\Sigma_k = S_k^{-1}\Lambda_g$ (primal-dual system), where $\Lambda_g = diag(\Gamma_g^1, \ldots, \Gamma_g^q)$. $\nabla^2_{xx}\mathcal{L}_{k+1}$ is calculated using Broyden-Fletcher-Goldfarb-Shanno (BFGS) formula:

$$\nabla_{xx}\mathcal{L}_{k+1} = \nabla_{xx}\mathcal{L}_k + \frac{q_k\ q_k^T}{q_k^T\ d_x(x_k)} - \frac{\nabla_{xx}\mathcal{L}_k\ d_x(x_k)\ d_x^T(x_k)\ \nabla_{xx}\mathcal{L}_k}{d_x^T(x_k)\ \nabla_{xx}\mathcal{L}_k d_x(x_k)}, \tag{3.12}$$

where $q_k = \nabla_x\mathcal{L}_{k+1} - \nabla_x\mathcal{L}_k$.

3.4 Application of Model Updating and the Results

It is necessary to determine which dynamic modes are to be included in the model updating process. Lower dynamic modes are generally sufficient to describe the global behavior of structures. In contrast, higher dynamic modes are generally more related to the local behavior of structures. Since more interest was placed on the matching of the global behavior of the structure, the first several dynamic modes are considered in the model updating process. In the model updating process of the bridge, three main-span vertical modes (V1, V2, and V3), two main-span lateral modes (H1 and H2), one main-span torsional mode (T1), and one side-span vertical mode (SV1) are taken into account. In this Chapter, the FE model is updated by targeting the mean of the identified natural frequencies and mode shapes, which is summarized in Table 2.1 and Figure 2.2, respectively.

The choice of the updating parameters is a crucial factor in the success of model updating (Brownjohn & Xia, 2000). It would be ideal for every physical parameters to be adjusted so that the FE model can perfectly match data from a real structure.

However, having too many updating parameters can ultimately yield an unreliable updating result (Hjelmstad, Banan, & Banan, 1995). Consequently, the physical parameters of structural components in an FE model are grouped based on their types, locations, and uncertainties. In the model updating for the bridge, the mass densities were adjusted because the exclusion of the nonstructural components would contribute to a miscalculation of the mass. It was assumed that the mass densities of the structural components located on the main span did not vary along the deck. One updating parameter was used for the mass densities of the main span components. Similarly, two different updating parameters were assigned for the mass densities of the side spans and of the towers. For the selection of the updating parameters associated with the Young's moduli of the superstructure, the global locations of the structural components such as the main span, side spans, and the towers were taken into account. It was also considered whether the structural components are located on the upper or lower deck since the bridge is a double-deck bridge. Moreover, their structural types such as chords, floor beams, columns, lateral bracings, and trusses were also taken into consideration. In addition to the updating parameters for the superstructure, all of the soil and hinge springs in the FE model were included for the updating process because the spring coefficients in the initial FE model were determined by trial and error. The physical parameters associated with the suspension cables were assumed to be fixed, i.e., no corresponding updating parameters. At the end, the total number of the updating parameters was 32. There were 17 and 15 updating parameters for the superstructure and the soil springs, respectively. The selected updating parameters are summarized in Table 3.1.

The interior method was used to minimize the differences between the FE model and the bridge by using the MATLAB optimization toolbox (MATLAB, 2013). The lower and upper bounds for the updating parameters θ^e were chosen to be in the range

between -2 and 0.8. These bounds for the updating parameters θ^e are equivalent to a 80% decrease and 200% increase in the physical parameters X^e. The lower bound (a 80% decrease) for the physical parameters, which was actually calculated by the upper bound of the updating parameters θ^e, was designed to make sure that the physical parameters remained in the realistic range (positive number for material properties). The upper bound of the physical parameters X^e, which was related to the lower bound of the updating parameters θ^e, was determined based on the fact that some dynamic modes started disappearing from the FE model when the physical parameters became close to the bound. The initial updating parameters θ_0 in the optimization were set to zero, which means the initial FE model was the starting point of the updating process. The stopping criteria was defined such that the functional tolerance was 1e-3 and the maximum number of iterations was 30. A flowchart of the model updating procedure considered in this Chapter is demonstrated in Figure 3.1.

The initial model was updated as described in Section 3.2. In Table 3.1, the optimized updating parameters (updated parameters) are shown. Figure 3.2 shows the values of the updating parameters versus the iterations of the optimization process. As mentioned in Section 2.3, the initial information about all of the structural components was somewhat vague, resulting in modifications of physical parameters by up to 52.2%. In order to offset the miscalculation of the mass of the structure due to the omission of the non-structural components and limited information, the mass density of the towers, the main-span, and the side-spans increased by 4.9%, 38.2%, and 52.5%, respectively. Since the technical drawings were quite limited especially for the trusses and chords in the side span, the modifications of those physical parameters were made over a large range within the updating process. The stiffness of the chords and the trusses in the side span seemed overestimated in the initial FE model. As a result, the Young's moduli for these components were reduced between

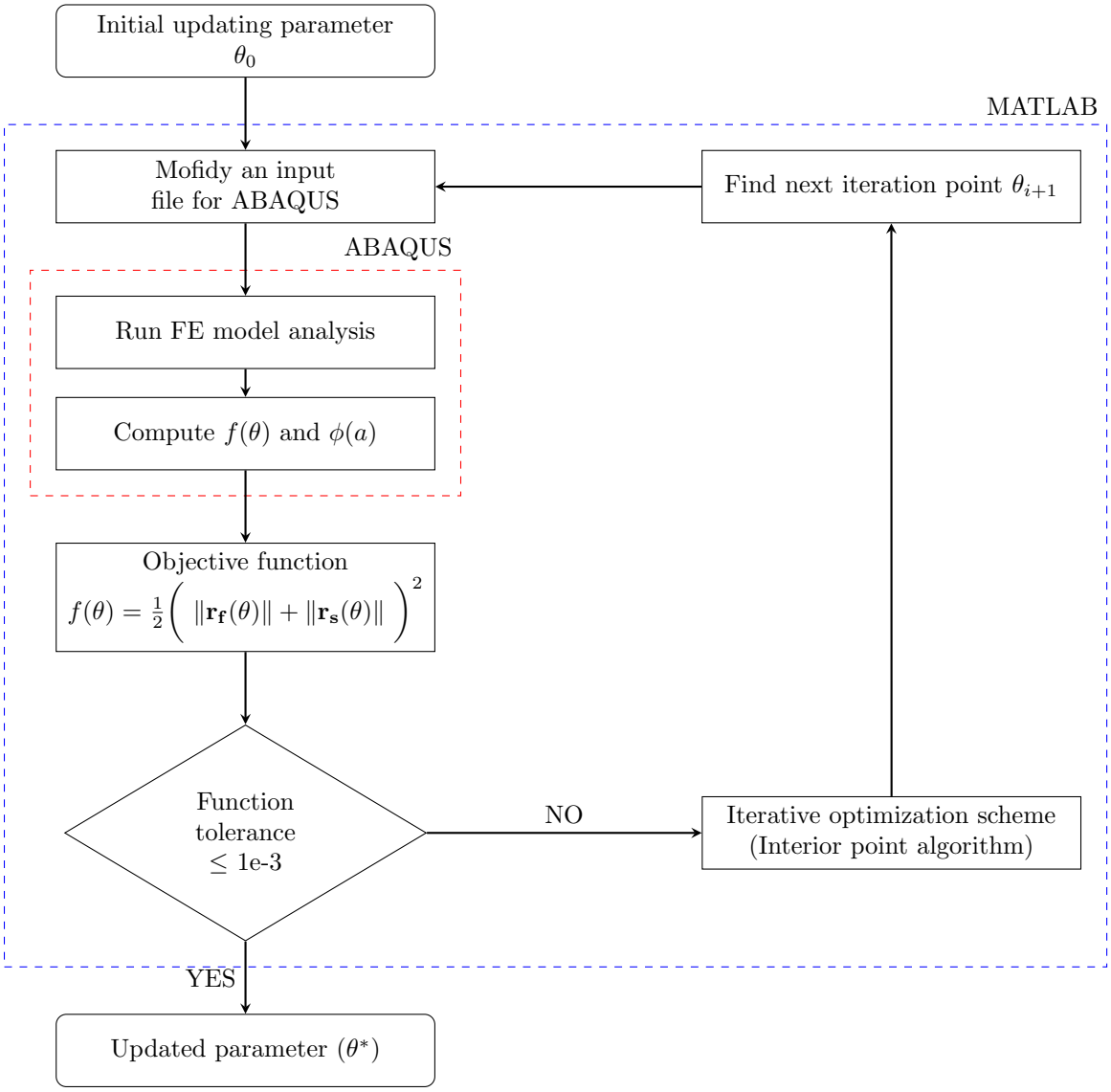

Figure 3.1: Flowchart of the model updating procedure.

Table 3.1: Physical parameters selected for the model updating for the bridge and the optimized updating parameters.

Number	Location	Structural type	Type	Updated parameter
1	Tower	Density	ρ	-0.049
2		Pylons	E	-0.003
3		Bracings	E	-0.071
4	Main span	Density	ρ	-0.382
5		Chords	E	0.023
6		Floor beams	E	-0.064
7		Columns	E	-0.057
8		Bottom lateral bracings	E	0.044
9		Top lateral bracings	E	-0.055
10		Trusses	E	0.018
11	Side span	Density	ρ	-0.525
12		Chords	E	0.271
13		Floor beams	E	-0.064
14		Columns	E	-0.048
15		Bottom lateral bracings	E	-0.089
16		Top lateral bracings	E	-0.059
17		Trusses	E	0.300
18	Hinge	Between towers and main span	k	-0.060
19		Between towers and side span	k	-0.058
20	Deck	Suspension cables	k	-0.060
21		Translational spring in longitudinal	k	-0.047
22		Deck translational spring in vertical	k	-0.061
23		Translational spring in transversal	k	-0.061
24		Rotational spring in longitudinal	k	-0.062
25		Rotational spring in vertical	k	-0.062
26		Rotational spring in transversal	k	-0.057
27	Tower leg	Translational spring in longitudial	k	-0.061
28		Translational spring in vertical	k	-0.068
29		Translational spring in transversal	k	-0.062
30		Rotational spring in longitudinal	k	-0.064
31		Rotational spring in vertical	k	-0.059
32		Rotational spring in transversal	k	-0.061

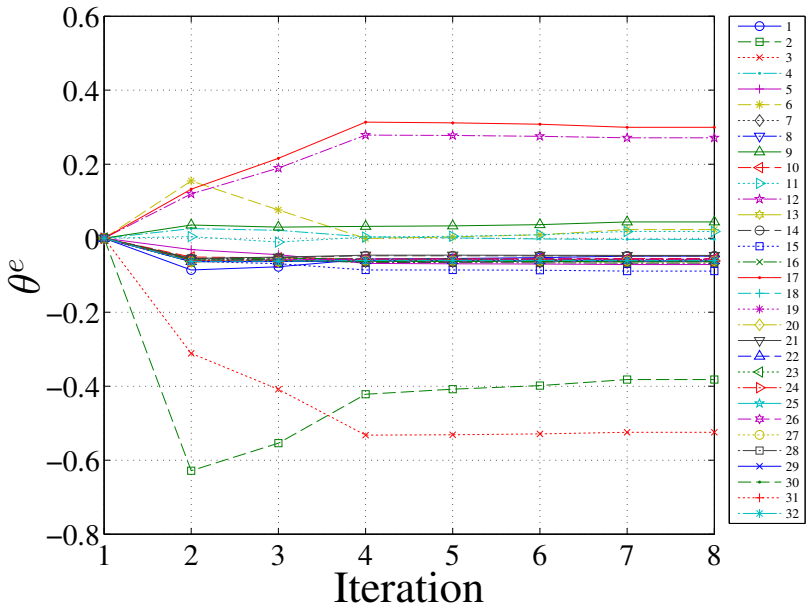

Figure 3.2: Convergence of the updating parameters during the optimization procedure.

27.1% and 30%, respectively. It is noteworthy that, except for above-mentioned physical parameters, parameter modifications were limited to less than 10% including the spring coefficients. These modifications of the mass densities and the Young's moduli permitted the natural frequency of the updated FE model to decrease so that they became closer to the natural frequencies identified from the real measured data.

The updated natural frequencies are summarized in Table 3.2. The MAC paring matrix is shown in Figure 3.3. After updating, the total relative errors dropped down from 59.23 % to 15.77%. Except for the first torsional mode (T1), the differences between the updated and identified natural frequencies were all reduced to below 5%. The reason that the natural frequency of the first torsional mode was not correctly adjusted might be due to the modeling errors which were not modified in the updating such as the geometry of the structure. The MAC values (Allemang & Brown, 1982) between the updated and identified mode shapes were used as an indicator of the

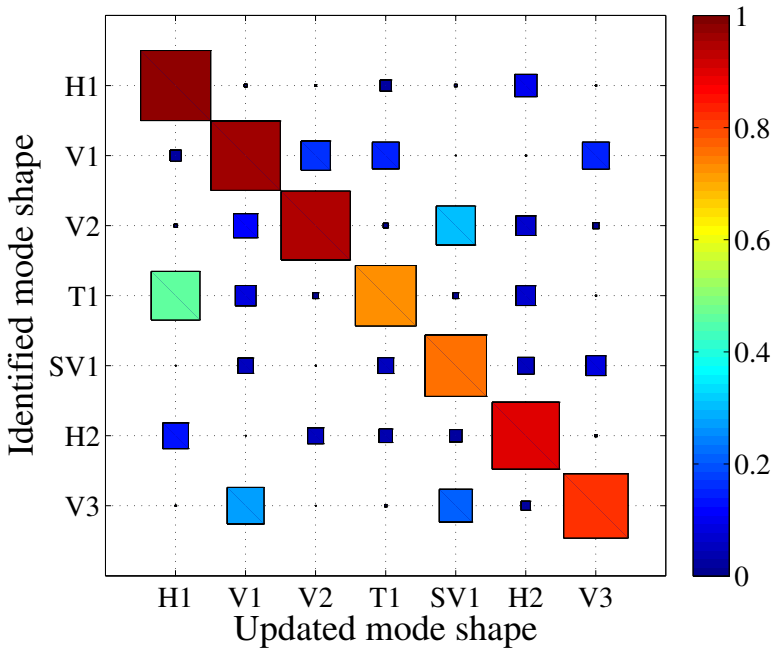

Figure 3.3: MAC pairing matrix between the identified mode shapes and updated mode shapes.

correlation between the two mode shapes. The MAC values are shown in Table 3.2. These MAC values are also shown in the diagonal of the pairing matrix in Figure 3.3. Most of the MAC values improved after the updating, especially for the higher mode shapes. The maximum increase in the MAC values, which corresponded to the third vertical mode (V3), was from 0.735 to 0.828. However, there is a drop in the MAC values of the first side span vertical mode (SV1).

Table 3.2: Identified, initial, and updated natural frequencies and the MAC values between the identified and updated mode shapes.

Mode	Frequency [Hz]					MAC value	
	Measured	FEM model					
		Initial	Relative error	Updated	Relative error	Initial	Updated
H1	0.194	0.236	0.218	0.195	0.006	0.984	0.984
V1	0.227	0.294	0.296	0.238	0.049	0.966	0.963
V2	0.303	0.356	0.176	0.311	0.027	0.979	0.949
T1	0.373	0.384	0.029	0.324	0.132	0.740	0.732
SV1	0.337	0.453	0.343	0.347	0.028	0.880	0.758
H2	0.450	0.539	0.197	0.470	0.044	0.838	0.898
V3	0.500	0.596	0.193	0.519	0.039	0.735	0.828
	Total L_2 norm error [%]		60.00		15.77		

3.5 Regularization: Implementation of a Nonlinear Constraint Equation in Model Updating

3.5.1 Multi objectives in model updating

When defining an objective function in the optimization problem in model updating, it is suggested to consider errors in both natural frequencies and mode shapes. Both natural frequencies and mode shapes are in general sensitive to physical parameters in an FE model. Moreover, some physical parameters can have more dominant effects on mode shapes than natural frequencies or vice versa. Not only that, when model updating is used for damage detection, natural frequencies can be an indicator for whether damage occurs or not; mode shapes can give more details about the localization of damage (Bakir et al., 2007; Teughels & De Roeck, 2004). Both natural frequencies and mode shapes play a significant role in tuning an FE model.

The objective cost function is calculated based on both the natural frequency

residual vectors and the mode shape residual vectors. Different selections of weighting factors for those two residual vectors can result in different model updating results. Well-balanced weights should be determined and applied to the residual vectors to provide acceptable results in both natural frequency and mode shape matches. If the natural frequency residual vectors have too much weight compared to the mode shape residual vectors, updating parameters are forced to have a good match in natural frequencies, making updated mode shapes in an FE model unacceptable. In contrast, if mode shape residual vectors receive more weight, computed natural frequencies can differ from identified ones. As a result, natural frequency residual vectors and mode shape residual vectors should be well-balanced in order to obtain a desirable agreement in both natural frequencies and mode shapes. It is good to notice that the frequency and mode shape residual vectors are equally weighted in Section 3.4.

At the same time, the need for the application of model updating can be also taken into account for the determination of the weights for the natural frequency and mode shape residual vectors. If the application for the FE model is more associated with mode shapes, more weight should be assigned for mode shape residual vectors. If natural frequencies of the FE model are of more interest, natural frequency residual vectors should be more weighted in objective functions. It is also possible that users of updated FE models want to have a threshold for mode shape matches based on the MAC values. To find a model updating result which has MAC values above a predetermined thresholds, many different combinations of weights for natural frequency and mode shape residual vectors can be tried. Multiple model updating results with respect to various weight values can be found by multi-objective optimization schemes, which are well summarized in (Marler & Arora, 2004). The effectiveness and applicability of the multi-objective optimization approaches for a model updating problem are demonstrated by Papadimitriou, Ntotsios, Giagopoulos,

and Natsiavas (2012).

3.5.2 Regularization on a mode shape agreement

Instead of performing multiple optimizations with different weights for frequency and mode shape residual vectors, the regularization technique, which is also known as parameter constraints, is applied to a model updating problem considered here to find a model updating result whose MAC values are above predetermined thresholds. Originally, the use of the regularization technique in model updating is suggested and developed by Friswell et al. (Friswell et al., 2001) in an effort to treat ill-posed parameter estimation problem, which is often encountered in model updating. This technique is adopted and modified to put constraint equations on mode shape agreements. Therefore, the residual vectors of natural frequencies and mode shapes are separately considered in an objective function and a constraint equation, respectively. The agreement of natural frequencies is the primary goal of the model updating process so that natural frequency residual vectors are defined in the objective function. Instead of considering mode shape residual vectors in the objective function, the MAC values between identified mode shapes and computed mode shapes are forced to remain higher than specific MAC values in the constraint equation. It becomes possible to prevent modified mode shapes in an FE model from having low MAC values after updating. When structures consist of many structural components or parts with complicated connections or when FE models have large initial modeling errors, some MAC values between updated and observed mode shapes might fail to remain in an desirable range. This problem can be observed in (Mottershead et al., 2011), where the challenging updating problem associated with many components and connections was tackled and some MAC values between the updated and observed modes are

less than 0.6, a level generally considered to be low. The reason for those low MAC values can be that in their model updating process the relative errors in the natural frequencies and the modification of the updating parameters are minimized, i.e., the MAC values or the errors in the mode shapes are not constrained to be optimized. The regularization technique can help improve a mode shape match when some MAC values are relatively low. The newly defined optimization problem with nonlinear constraints is presented as follows:

$$\begin{aligned} &\underset{\theta}{minimize} \quad f(\theta) \\ &\text{subject to} \quad g(\theta) \leq 0 \text{ (inequality constraint)}, \end{aligned} \tag{3.13}$$

where $f\colon \mathbf{R}^{n_p} \to \mathbf{R}$, $g\colon \mathbf{R}^{n_p} \to \mathbf{R}^{n_t}$. n_p and n_t are the number of updating parameters and targeted dynamic modes, respectively. θ are updating parameters, which are the same as the ones used in Section 3.4. The objective function $f(\theta)$ and the inequality constraint equation $g(\theta)$ are defined as:

$$\begin{aligned} f(\theta) &= \frac{1}{2}\|\mathbf{r_f}(\theta)\|^2 \\ g_j(\theta) &= d_j - MAC_j(\theta), \end{aligned} \tag{3.14}$$

where $\mathbf{r_f}(\theta)$ is the natural frequency residual vector defined in the Eq. 3.3. $MAC_j(\theta)$ is the MAC value between identified and computed mode shapes corresponding to the jth dynamic mode; d_j is a desired MAC level for $MAC_j(\theta)$. By putting the inequality constraint equation $g(\theta)$ into Eq (3.13), the optimization problem can be restated as:

$$\begin{aligned} &\underset{\theta}{minimize} \quad f(\theta) \\ &\text{subject to} \quad MAC_j(\theta) \geq d_j \text{ (inequality constraint)} \end{aligned} \tag{3.15}$$

The FE model of the bridge was updated based on the objective function with

the constraint equation. The differences between the identified natural frequencies and those from updated FE model were minimized by defining them in the objective function. At the same time, the MAC values between the identified mode shapes and those computed from updated FE model were regulated to remain above a desired MAC level. The two desired MAC levels used here were defined as 0.7 and 0.8 ($d_j = 0.7$ and 0.8). The desired MAC levels were equally applied to the first seven dynamic modes. Different desired MAC levels can be applied for different dynamic modes when more importance is placed on certain modes.

3.5.3 Updating results with nonlinear constrains

The results of the model updating based on the suggested method are summarized in Table 3.3. The MAC paring matrices between the identified and updated mode shapes associated with the desired MAC levels 0.7 and 0.8 are presented in Figures 3.4ab, respectively. Figure 3.5 shows the values of the updating parameters versus the iterations of the optimization process with two levels of the MAC constraints. Figure 3.6 shows a comparison between the two sets of optimized updating parameters with respect to the corresponding desired MAC levels and the one that is obtained in Section 3.4. When the desired MAC level 0.7 was used in the constraint equation, the optimization result was quite similar to the updating result in Section 3.4. This is because the MAC values in Section 3.4 were already higher than 0.7. When the desired MAC level of 0.8 was applied, all of the MAC values increased so that they became higher than 0.8. The mode shape of the first torsional mode was significantly improved. However, more total relative errors in the natural frequencies were observed when the desired MAC level increased from 0.7 to 0.8. The total norm error in the natural frequencies increased from 15.85 to 18.77% as the desired MAC level increased.

The biggest change in the frequency error happened in the first vertical mode (V1). After increasing the desired MAC level, the frequency error in V1 became 12.8%. Although there was a trade-off between the natural frequencies and mode shapes, the presence of the inequality constraint equations can be a powerful mechanism to regulate the agreement in mode shapes without trying multiple combinations of different weights for the natural frequency and mode shape residual vectors, especially when some mode shapes failed to have an acceptable match or when more interest was place on mode shape matching.

Table 3.3: Updated natural frequencies and MAC values between the identified and updated mode shapes with the two desired MAC levels (0.7 and 0.8).

Mode	Frequency [Hz]					MAC value	
	Measured	FEM model					
		MAC 0.7 constraint	Relative error	MAC 0.8 constraint	Relative error	MAC 0.7 constraint	MAC 0.8 constraint
H1	0.194	0.189	0.025	0.181	0.066	0.988	0.991
V1	0.227	0.241	0.062	0.253	0.115	0.963	0.964
V2	0.303	0.307	0.014	0.296	0.022	0.963	0.976
T1	0.373	0.323	0.135	0.332	0.111	0.756	0.801
SV1	0.337	0.349	0.034	0.365	0.082	0.814	0.873
H2	0.450	0.459	0.020	0.434	0.036	0.922	0.940
V3	0.500	0.513	0.027	0.501	0.003	0.829	0.818
	Total L_2 norm error [%]		15.85		19.58		

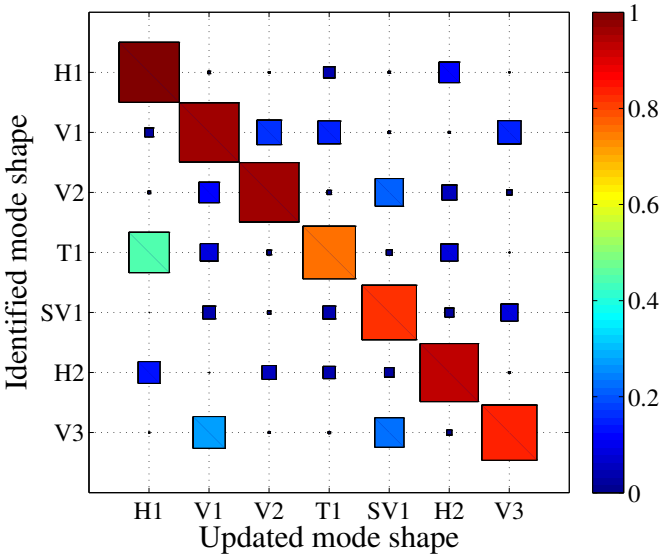

(a)

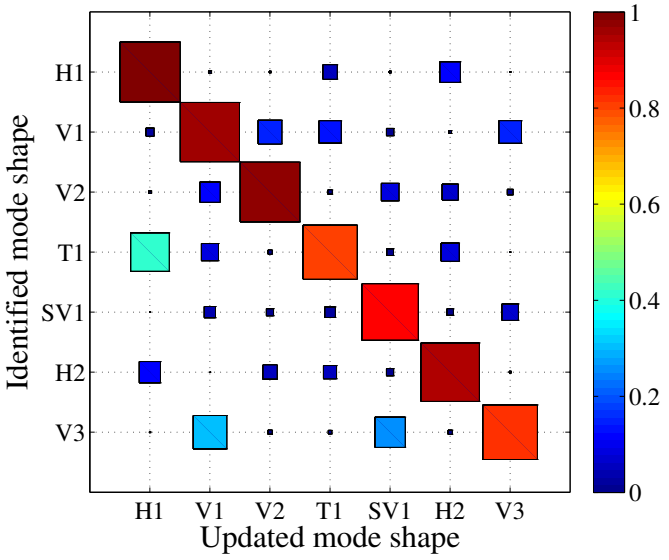

(b)

Figure 3.4: MAC pairing matrices between the identified mode shapes and the mode shapes of the updated models with the MAC constraints: (a) MAC level 0.7; and (b) MAC level 0.8.

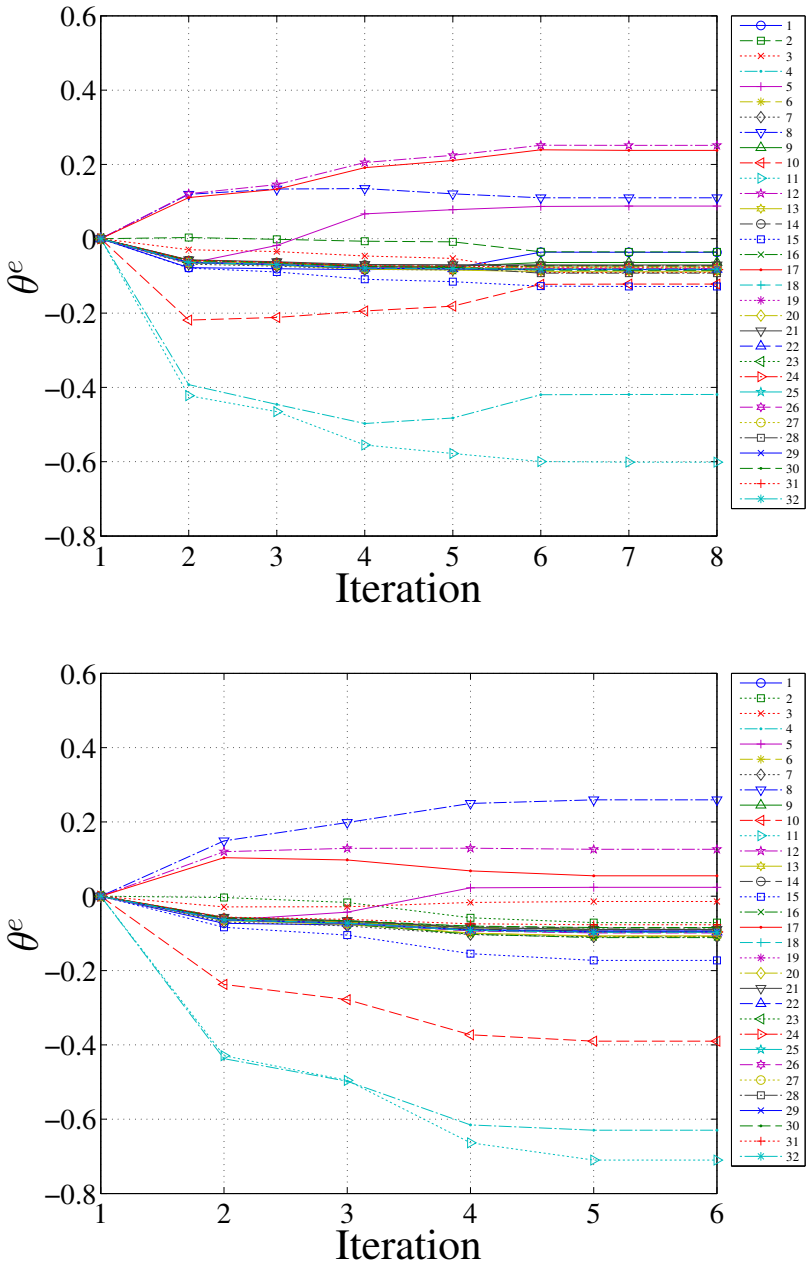

Figure 3.5: Convergence of the updating parameters during the optimization procedure with two levels of the MAC constraints:(a) MAC level 0.7; and (b) MAC level 0.8.

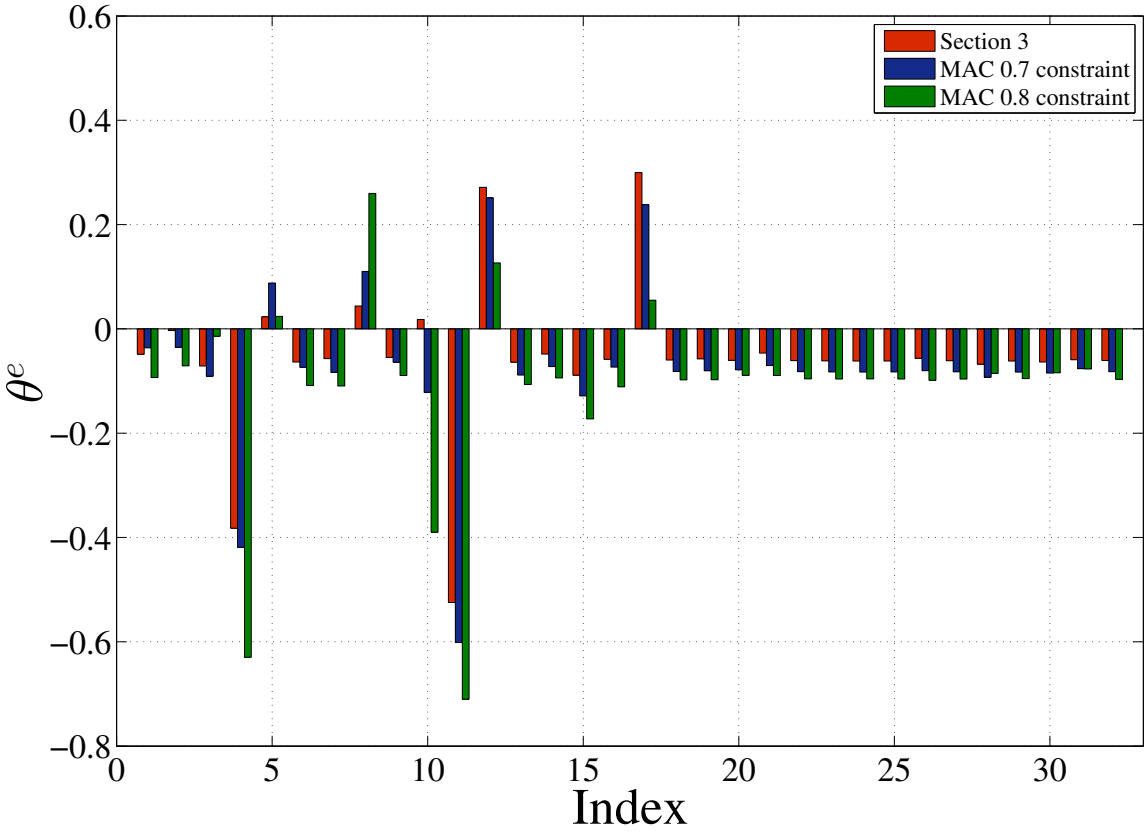

Figure 3.6: Comparison of optimized updating parameters: Section 3, 0.7 MAC level, and 0.8 MAC level.

3.6 Sensitivity-based Clustering for Parameterization in Model Updating

3.6.1 Importance of parameterization in model updating

Selecting very efficient updating parameters from physical parameters is very important to achieving a satisfactory model updating result since they are directly related to the change of the modal properties of FE models. One updating parameter here includes many physical parameters of structural components since there are a large number of physical parameters in the model and it is unrealistic to modify physical parameters piece by piece. In this application, there are 21,096 elements (19,632 beam elements + 1464 truss elements) and each element has a Young's modulus and mass density. This means that there are 42,192 physical parameters. A limited number of updating parameters should be selected from 42,192 physical parameters. The more updating parameters which are included, the bigger the gradient matrices (Jacobian and Hessian matrix) which are computed. The problem is that bigger gradient matrices tend to become ill-conditioned. When the gradient matrices are ill-conditioned, the result of the gradient-based optimization is not reliable. Moreover, the computational cost of the numerical calculation of the gradient matrices linearly increases with the dimension of the updating parameters.

There are some considerations to determine updating parameters. It is obvious that uncertain physical parameters in FE models should be included in the modification during the updating process. Topological and technical consideration in model updating also should be taken into account for the selection of updating parameters. In addition, a further in-depth sensitivity analysis can be carried out to provide more

information about how physical parameters affect natural frequencies of a structure. Shaverdi et al. (Shahverdi et al., 2009) have developed the innovative sensitivity-based clustering method, which leverages clustering analysis and parameter sensitivities, and have validated its benefits with an example of a helicopter airframe. The major benefit of this method is that each updating parameter can have a physical insight since it includes physical parameters whose effects to natural frequencies are similar. In this work, the sensitivity-based clustering method is applied to a full-scaled FE model to systematically determine a more effective selection of updating parameters for the bridge model. Furthermore, the physical meanings of updating parameters selected from the sensitivity-based clustering method are demonstrated, which provides fundamental knowledge of the relationship between natural frequencies and the physical properties of structural components.

3.6.2 Sensitivity analysis on decomposed structural components

The structural components of the FE model were decomposed into the 132 subgroups based on the location and structural type. The main span was partitioned into eight segments along the longitudinal direction. Each side span was divided into four segments along the longitudinal direction. Then, each segment was further decomposed into subgroups based on the structural element type. The towers were divided into three segments along the vertical direction and each segment was divided into the bracing and pylon elements. Both mass densities and Young's moduli of the decomposed 132 subgroup were considered in the analysis. All of the soil and hinge springs (15 spring coefficients) in the FE model were also included for the cluster analysis. 279 physical parameters (132 masses + 132 Young's moduli + 15 spring coefficients)

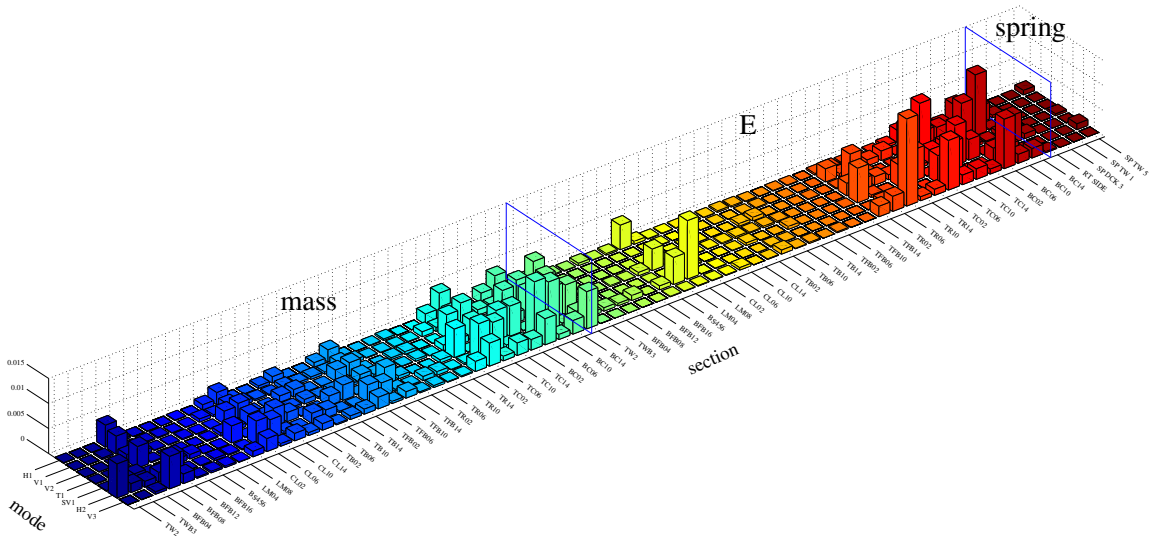

Figure 3.7: Sensitivity to the mass densities and Young's moduli of the decomposed structural components and spring coefficients: 70 out of the 279 physical parameters.

were formed after the decomposition of the FE model.

Then, the sensitivities of natural frequencies corresponding to those 279 physical parameters were calculated as follows:

$$\frac{\partial f_p}{\partial X_q}, \tag{3.16}$$

where f_p is the natural frequencies of p^{th} mode and X_q is q^{th} physical parameters. $q = 1, \ldots, 7$ and $q = 1, \ldots, 279$. For general visualization purposes only, every 4^{th} column of the sensitivity matrix is shown in Figure 3.7. Along the horizontal axis, the indices of the decomposed subgroups are shown with respect to the targeted dynamic modes. The height of the bars is the sensitivity of the natural frequency with respect to the physical parameters. Since perturbing the mass density in the FE model had an opposite effect to the natural frequencies compared to perturbing the Young's modulus and spring coefficient, two parallel cluster analyses were carried out

based on the calculated sensitivities. The first cluster analysis is for the sensitivities associated with the mass densities of the decomposed subgroups. The second is for the sensitivities corresponding to the stiffness-related parameters (Young's moduli and spring coefficients of the decomposed subgroups).

3.6.3 Hierarchical clustering for the sensitivities of natural frequencies

The purpose of cluster analysis is to group closely-spaced sensitivities into a cluster, which means that the distance function should be defined in order to compute the proximity between sensitivities. The distance function used here is the dissimilarity of the sensitivity matrices corresponding to the physical parameters. In other words, two near (short) distanced sensitivities means that the sensitivity matrices corresponding to the physical parameters are similar, i.e., the physical parameters have similar effects to the targeted natural frequencies. Cosine distance (Salton & Buckley, 1988) is used to evaluate the dissimilarity between pairs of sensitivities (α, β), which was defined as:

$$\text{cosine distance}(\alpha, \beta) = 1 - \frac{\alpha^T \beta}{\sqrt{\alpha^T \alpha \cdot \beta^T \beta}} \tag{3.17}$$

After defining the distance function, it was necessary to choose an appropriate clustering algorithm that was applicable to the problem. Many clustering algorithms were available such as hierarchical (Everitt, Landau, Leese, & Stahl, 2011), k-means (Hartigan & Wong, 1979), and DBSCAN (Ester, Kriegel, Sander, & Xu, 1996). The hierarchical clustering algorithm was used here because it enabled one to determine final clusters only based on the maximum distance between the sensitivities which are grouped into the same cluster. k-means clustering was not feasible

because the total number of clusters (k) would need to be predefined in advance. The DBSCAN algorithm would exclude some sensitivities as outliers based on a pre-specified input variable, which is the number of points required to create a cluster. However, the hierarchical clustering algorithm would permit each sensitivity to be grouped into clusters. In the hierarchical clustering, all of the pairwise distances between sensitivities were initially calculated. Then, the sensitivities were grouped into binary clusters based on the proximity of their distance, i.e., based on the similarities of the sensitivities. The binary clusters also became larger by including the closest (the most similar) sensitivities or another binary cluster. This was repeated until a hierarchical tree (one big binary cluster) was formed. Final clusters were determined from a hierarchical tree by specifying the maximum distance between the sensitivities in the same cluster.

The hierarchical binary trees associated with the sensitivities of the physical parameters of the subgroups are shown in Figure 3.8. The vertical line (height) represents the distance between the merged binary clusters. In the horizontal axis, there are 30 leaf nodes, representing binary clusters into which the sensitivities of the subgroups are already grouped. The final clusters are determined by cutting each hierarchical tree at the distance 0.2, which means all of the dissimilarities of the sensitivities in the same final cluster are less than 0.2. At the end, the 279 sensitivities corresponding to the physical parameters of the decomposed subgroups are grouped into 22 clusters. 5 clusters included sensitivities with respect to the mass densities of the subgroups. 17 clusters included the sensitivities corresponding to Young's moduli and/or spring coefficients. Each cluster was defined as a updating parameter defined in Eq. 3.1, which means that 22 updating parameters were selected from the sensitivity-based cluster analysis. The first five updating parameters ($\theta_1 - \theta_5$) are mass densities. The other updating parameters ($\theta_6 - \theta_{22}$) are stiffness-related parameters.

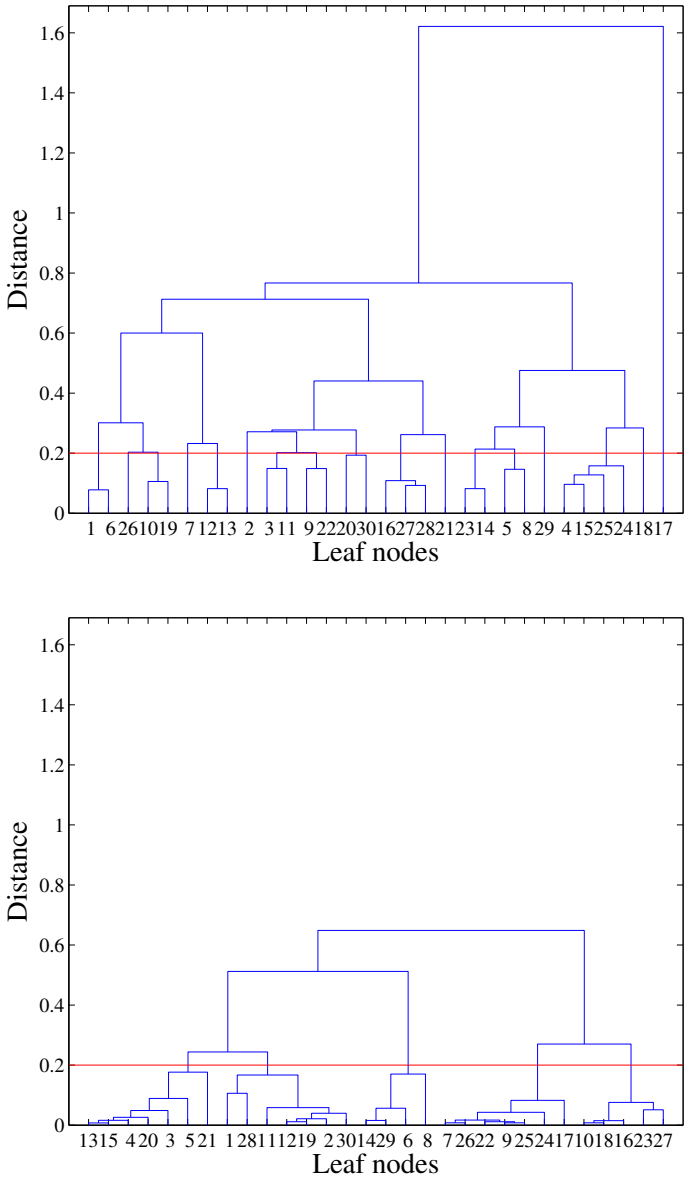

Figure 3.8: Hierarchical binary cluster tree with 30 leaf nodes: (a) Young's modulus & spring coefficient; and (b) Mass density.

3.6.4 Updating parameters selected by the sensitivity-based clustering and the interpretation of their physical meanings

To visualize the difference between mass clusters and stiffness-related clusters (Young's modulus and spring coefficient), the locations of the structural components corresponding to the physical parameters and the respective sensitivity matrices are shown in Figures 3.9 and 3.9. The sensitivities corresponding to the mass densities were grouped mainly based on the longitudinal location of the structural components along the bridge, rather than their structural type. As shown in Figure 3.9, the mass clusters included the mass densities of all structural components regardless of their structural types. In contrast, the stiffness-related clusters grouped the similar sensitivities depending on both the longitudinal locations and the structural types. The structural components that correspond to the physical parameters grouped into cluster 6, 7 and 22 were presented respectively in Figure 3.10. The corresponding sensitivity matrices grouped into cluster 6, 7, and 22 are shown in Figures 3.10bdf, respectively. The Young's moduli of the trusses and chords located at the main span were included in cluster 6, which means that the types of structural components affected the result of the clustering. It is noteworthy that spring elements were included in these clusters. In cluster 6, the hinges (rotational spring) between the main-span deck and the towers were included. In cluster 22, the soil springs located at the end of the deck (the translational spring in the longitudinal direction and the rotational spring in the transversal direction) and the hinges connecting towers with the side span were included.

It was quite clear to see that the physical parameters grouped into the same cluster

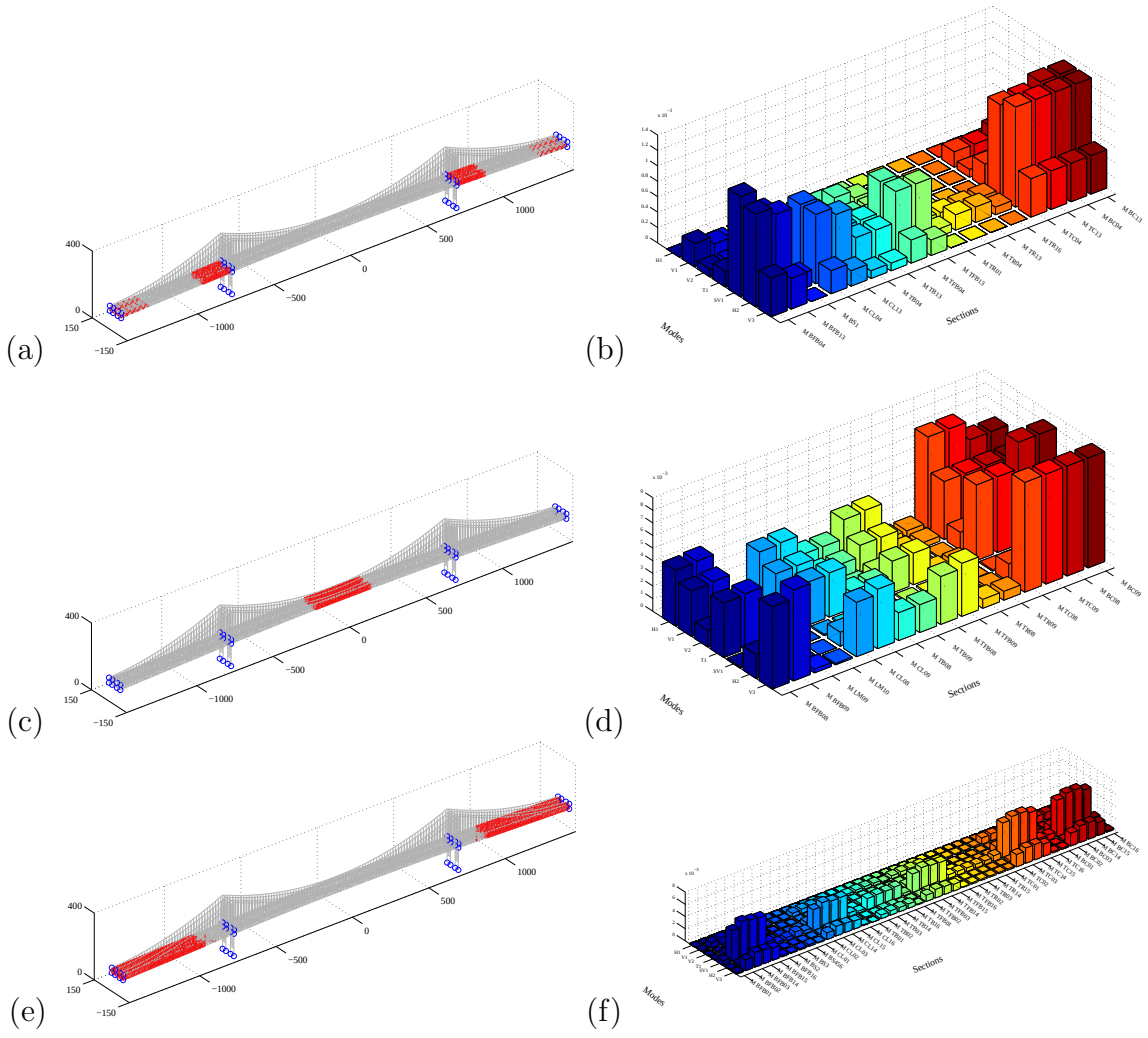

Figure 3.9: Cluster analysis result of mass densities: the locations of the structural components in the clusters and the corresponding sensitivity matrices: (a) topological locations of cluster 2; (b) sensitivity matrix of cluster 2; (c) topological locations of cluster 3; (d) sensitivity matrix of cluster 3; (e) topological locations of cluster 5; and (f) sensitivity matrix of cluster 5.

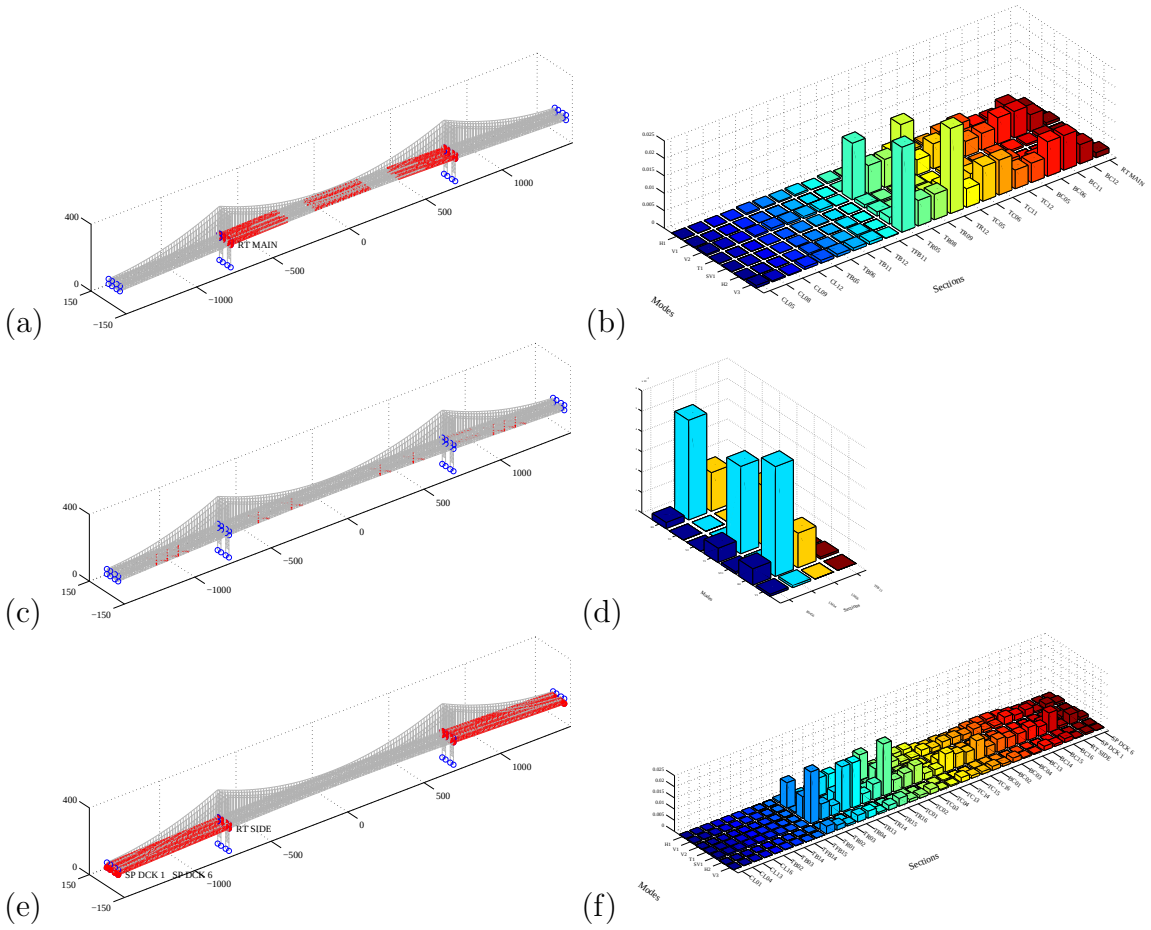

Figure 3.10: Cluster analysis result of stiffness-related parameters: the locations of the structural components in the clusters and the sensitivity matrices: (a) topological locations of cluster 6; (b) sensitivity matrix of cluster 6; (c) topological locations of cluster 7; (d) sensitivity matrix of cluster 7; (e) topological locations of cluster 22; and (f) sensitivity matrix of cluster 22.

had similar effects on the targeted natural frequencies. Although the clusters were determined only based on the numerical values of the sensitivities, without providing any information of the corresponding locations of the structural components, the grouped physical parameters were physically meaningful. The physical parameters in cluster 6 had more dominant effects on the natural frequencies of the second and third vertical modes (V2 and V3) since the Young's moduli of the chords and trusses located at the main span were included for this cluster. The structural components in cluster 22 were likely to affect the natural frequencies of the first side-span vertical mode (SV1) and the first vertical mode (V1) because the physical parameters of the structural components mainly located at the side spans.

Based on the sensitivity matrix shown in Figure 3.7, it was found that the most sensitive structural types were chords (TC and BC), lateral bracing (LM and BS), trusses (TR), and towers (TW). When it came to the soil springs at the bottom of the tower pylons, the translational springs in the vertical direction (SP TW2) and the rotational spring in the longitudinal direction (SP TW4) dominantly affected the natural frequencies. Among the soil springs at the end of the deck, the translational springs in the longitudinal direction (SP DCK1) and the rotational springs in the transversal direction (SP DCK6) were sensitive. Furthermore, if the structural components were in symmetrical locations, they had almost identical sensitivities due to the symmetry of the bridge. This phenomenon can be observed in Figures 3.9 and 3.10. For example, the sensitivity of the trusses at the left side span (TR01, TR02, TR03, and TR04) were identical to the sensitivity of the ones at the right side span (TR16, TR15, TR14, TR13) because 01, 02, 03, and 04 were respectively the symmetrical locations with 16, 15, 14, and 13. Similarly, the bottom chords at the main-span that were close to the left tower (BC05) were also identical to the counterpart in the right side (BC12).

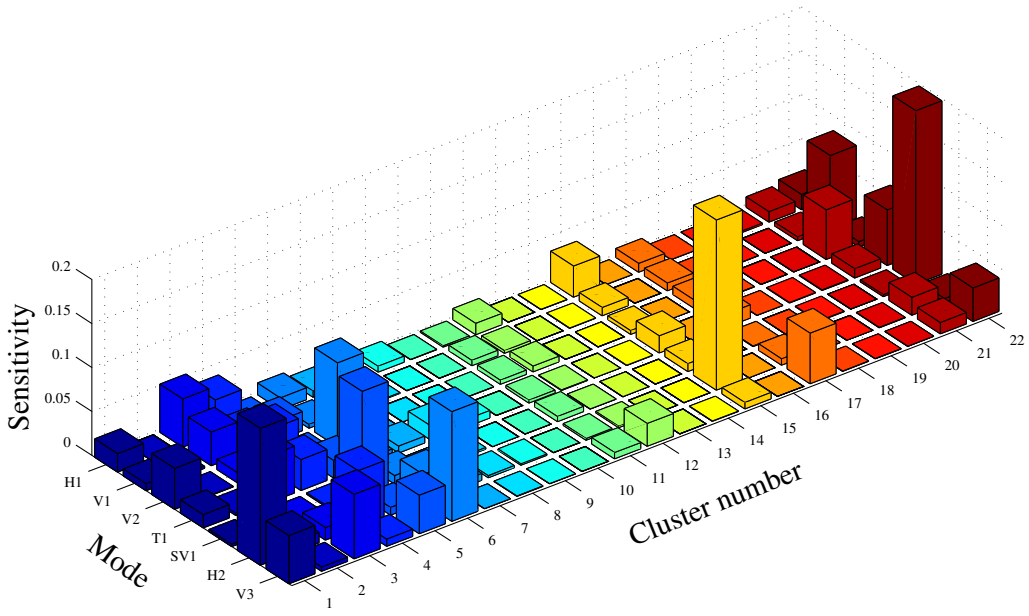

Figure 3.11: Sensitivity matrix of clusters.

The sensitivity matrix of the clusters is represented in Figure 3.11. The cluster numbers are shown in the horizontal axis with respect to the targeted natural frequencies. As mentioned before, cluster 6 is more sensitivity to the second and third vertical modes (V2 and V3). Cluster 22 is more likely to change the natural frequencies of the first side-span vertical (SV1) and the first vertical (V1) modes. Cluster 15 dominantly affects the natural frequency of the second lateral mode (H2). The physical parameters in this cluster are the Young's moduli of the lateral bracings at the middle of the main span, the lower parts of the towers, and some soil springs at the tower leg. Cluster 17 includes the Young's moduli of the chords and the trusses located at the quarter point of the main span so that it has more effect on the third vertical mode (V3). When it comes to the mass clusters (from cluster 1 to 5), the

effects on the targeted frequencies change based on the longitudinal location along the bridge.

3.6.5 Updating results with sensitivity-based clustering

Compared to the updating parameters defined in Section 3.4, sensitivity-based cluster analysis yielded fewer updating parameters, but was more efficient since each updating parameter included the physical parameters whose effects on the targeted natural frequencies were similar. In Table 3.4, the model updating results with two different sets of the updating parameters were compared. Figure 3.12 shows the values of the updating parameters, which are determined by the sensitivity-based clustering method, with respect to the iterations of the optimization process. The MAC pairing matrix between the identified and updated mode shapes was shown in Figure 3.13.

The updating parameters determined by the sensitivity-based cluster analysis led to a decrease in the total L_2 norm error from 15.77 to 14.62%. The better MAC values were achieved with the updating parameters from the cluster analysis. The significant improvement was achieved for the third vertical mode (V3), where the MAC value increased from 0.828 to 0.947. The only MAC value which did not increase was the second lateral mode (H2). However, the values remained quite similar to the result without the cluster analysis. The MAC values were high enough to provide a reasonably good correlation with the identified mode shapes. Although fewer updating parameters were used, the improvement in the updated natural frequency was possible because the cluster analysis permitted each updating parameter to have a similar effect on the targeted natural frequencies.

Table 3.4: Comparison of the results in updating with cluster analysis and without cluster analysis.

Mode	Frequency [Hz]					MAC value	
	Measured	FE model[a]	Error	FE model[b]	Error	FE model[a]	FE model[b]
H1	0.194	0.195	0.006	0.192	0.009	0.984	0.984
V1	0.227	0.238	0.049	0.243	0.071	0.963	0.967
V2	0.303	0.311	0.027	0.295	0.026	0.949	0.978
T1	0.373	0.324	0.132	0.330	0.116	0.732	0.751
SV1	0.337	0.347	0.028	0.349	0.034	0.758	0.834
H2	0.450	0.470	0.044	0.451	0.002	0.898	0.873
V3	0.500	0.519	0.039	0.515	0.031	0.828	0.947
	Total L_2 norm error [%]		15.77		14.62		

[a] The updated model with updating parameters defined in Section 3.4
[b] The updated model with updating parameters chosen by the sensitivity-based cluster analysis

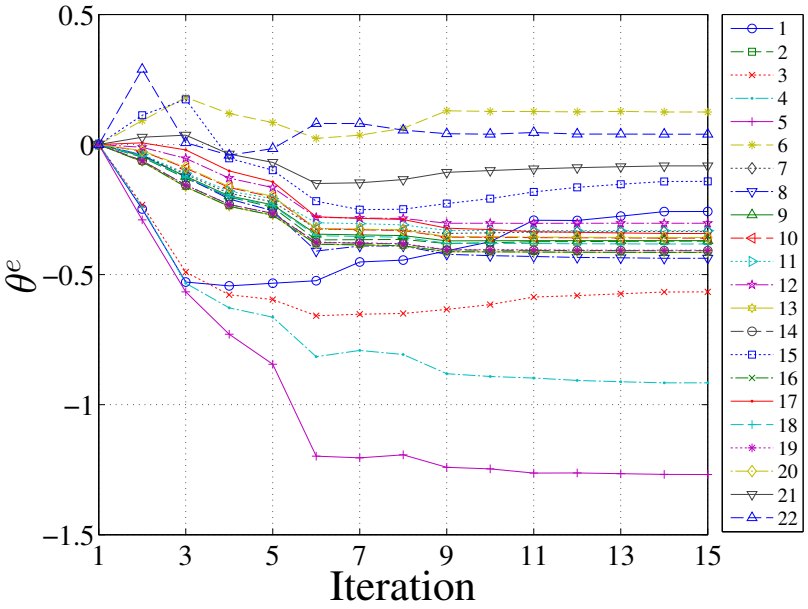

Figure 3.12: Convergence of the updating parameters, which are determined by the sensitivity-based clustering method.

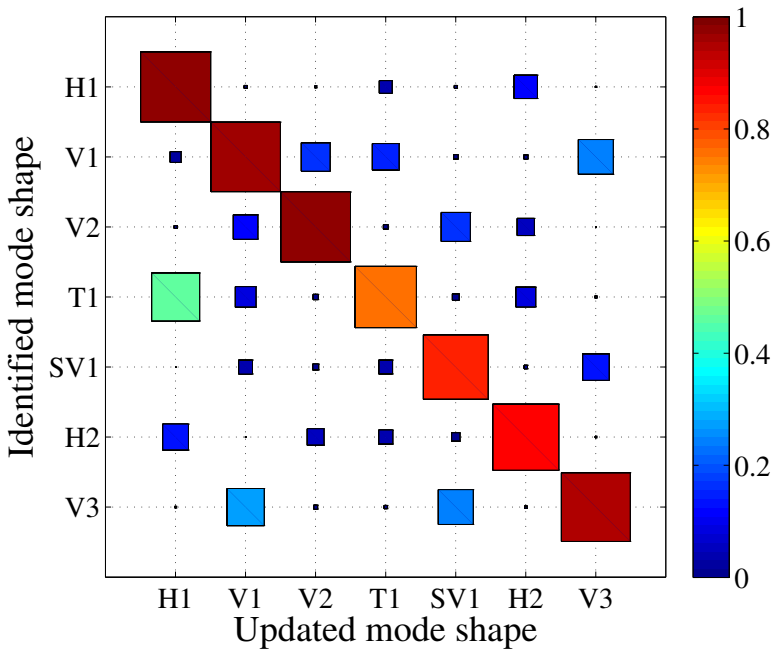

Figure 3.13: MAC pairing matrix between the identified mode shapes and the mode shapes of the updated model with updating parameters determined by the sensitivity-based clustering.

3.7 Conclusions

3.7.1 Importance of system identification technique in model updating

In model updating, it is assumed that identified modal properties from dynamic tests are correct because the FE models of structures are tuned to match them. Since model updating techniques cannot be a remedy for a observational deficiency, the most careful attention should be paid when identifying modal properties from measure data. Moreover, when vibration data measured from an ambient dynamic test of a bridge are used for system identification, measurement noise and environmental effects should be properly considered during a monitoring period. Through the model updating exercises visited in this chapter, unsatisfactory updating results were observed with the first torsional mode. This can be because the three torsional modes of the bridge deck were identified, but they had different in-phase or out-of-phase motions with the suspension cables and different interactions with main span and side spans as well. Those interactions were revealed by accurate GPS sensors installed on the bridge, which is not used for the study here. However, the FE model considered here was not able to produce all those three modes since the interactions between the suspension cables and the deck (nonlinear geometry) was not modeled. Therefore, one of the identified torsional modes was set as a target in the model updating process, which led to unsatisfactory updating results with the first torsional mode. It was concluded that modeling error due to unmodeled physical properties cannot be recovered by the model updating practice.

3.7.2 Nonlinear constraints in balancing between natural frequencies and mode shapes

The regularization technique has been adopted and applied to the model updating of a bridge model to control the agreements between mode shapes from measurements and ones from an FE model. By forcing the MAC values to remain above a certain level, nonlinear inequality constraint equations prevent computed mode shapes from unacceptably deviating from identified mode shapes. Two model updating exercises using the regularization technique were carried out with the full-scaled bridge model. The use of the nonlinear constraints in the optimization process was successful in maintaining the MAC values between the computed mode shapes and the identified mode shapes within a prescribed desirable range. Although there is a trade-off in the natural frequencies versus the mode shapes, this method can be useful when some updated mode shapes do not have a relatively good match. The placement of constraints on a mode shape agreement also can be practically beneficial when a priori knowledge is given on the the quality of mode shape measurements due to limited sensor placements and/or measurement noise level. In this chapter, the ability of the regularization technique to constraint mode shape agreements is demonstrated using a full-scaled FE model and real measured data. More study should be done to understand what level of overall agreements can be achieved by the use of nonlinear MAC constraints when a model updating problem is subjected to different levels of modeling errors, different configurations of sensor placements, and different noise levels.

3.7.3 The selection of the modal parameters sensitivity-based clustering analysis

Sensitivity-based clustering analysis was conducted to determine the efficient sets of the updating parameters. The physical parameters grouped in the same updating parameter had similar effects on the targeted natural frequencies. The more efficient selection of the updating parameters led to the better model updating result, compared to the result with the updating parameters selected using engineering judgment. It was observed that the sensitivity-based clustering method grouped physical parameters that are located in the symmetrical positions along the longitudinal direction into the same updating parameter. However, modeling errors do not necessary to be the same for those symmetrically-positioned physical parameters, e.g., damage can be propagated into one side of a structure. When the model updating techniques is used for structural damage detection, grouping symmetrically-positioned physical parameters into the same parameter is not preferred since it can pose a difficulty in localizing possible structural damage. This behavior of the sensitivity-based clustering analysis, which groups physical parameters without taking their structural spatial information into consideration, can be a drawback of this method. Therefore, the sensitivity-based clustering method should be developed further to overcome its possible drawback.

3.7.4 The results of four model updating exercises

In this chapter, four model updating exercises with the regularization and sensitivity-based clustering techniques are visited. The performances of the updated models are evaluated based on the error estimates in the natural frequencies and the MAC values. The performances of the updated model should not be generalized only based on those

error estimates since neither measure data and a model cannot be unique. When it comes to choosing the best model among possible candidates, engineering judgment is still required. The prediction capability of an updated model estimated by the cross validation technique also can be taken into consideration of model selection.

Chapter 4

Bayesian Model Updating

This chapter explores the Bayesian model updating approach, which belongs to a probabilistic scheme in model updating. Compared to the deterministic approach, which is addressed in the previous chapter, the probabilistic model updating approach has some advantages. The probabilistic approach has a more robust capability to deal with uncertainties associated with an updating problem and ability to provide distributions of physical parameters of a model. However, the Bayesian model updating of a full-scale FE model based on real measurements is rare due to the complexity of a model and the uncertainties of measurements. This chapter explores the applicability of Bayesian model updating to a full-scale model.

4.1 Introduction

In general, model updating can be classified into two approaches: deterministic model updating and stochastic model updating. The first approach determines a unique solution by solving an optimization problem, which minimizes discrepancies in modal properties or structural responses between FE models and real structures. Various

optimization algorithms such as the Gauss-Newton algorithm with a trust region, interior point algorithm, and genetic algorithm are used to solve optimization problems associated with model updating (Moaveni & Behmanesh, 2012; Bakir et al., 2007; Mosquera et al., 2012). The second approach finds multiple solutions based on a probabilistic scheme. There are several advantages of having multiple solutions. Multiple solutions permit the determination of whether problems are globally identifiable, locally identifiable or unidentifiable cases. In globally and locally identifiable cases, solutions can be obtained from the dominant peaks of the posterior probability distributions of updated parameters. In unidentifiable cases, invariant parameter regions can be identified based on flat regions in posterior distributions. Furthermore, multiple solutions not only enable the evaluation of the uncertainties of the FE model's updated parameters, but also quantify the propagation of these updating parameters' uncertainties into modal properties and/or structural responses. Estimated statistical information plays an important role in the prediction of future responses and reliability of structures.

Many uncertainties arise in model updating because of possible modeling assumptions in the development of FE models and variations in measured data. These uncertainties should be properly considered and managed during the updating process to produce a more accurate updated FE model. In general, there are two types of uncertainties: epistemic and aleatory. Epistemic uncertainties account for unknowns due to the lack of knowledge. In model updating, these uncertainties include uncertain material properties and geometry because of limited knowledge, as well as joint stiffness, boundary conditions, and unmodeled nonlinear behavior arising from the simplification of FE models. Deterministic model updating methods are the appropriate choice only when dealing with epistemic uncertainties. Aleatoric uncertainties represent unknowns that can only be determined by statistical measurement. These

unknowns might differ for each repetition of the same experiment or measurement such that their physical outcomes are best described using statistical measures such as mean, variance, and higher-order statistical moments. The engineering tolerance associated with the physical properties of structural components is incorporated into aleatoric uncertainties. Moreover, variations in natural frequencies and mode shapes that are identified from real measured data are good examples of aleatoric uncertainties. Variations of identified modal properties due to environmental effects such as temperature (Peeters & De Roeck, 2001; Sohn, 2007) and traffic (Brewick & Smyth, 2013) are commonly observed during structural dynamic tests. Stochastic model updating methods can more efficiently manage aleatoric uncertainties.

Bayesian model updating is a popular stochastic model updating method. It has a significant advantage because of its robustness in dealing with uncertainties and ability to provide distributions of updating parameters. The statistical framework of Bayesian model updating was developed by (J. Beck & Arnold, 1977; J. L. Beck & Katafygiotis, 1998) and employed later by (J. L. Beck & Au, 2002) using the adaptive simulation method. Bayesian model updating necessitates solving multi-dimensional integration problems, which might be analytically challenging, especially when many updating parameters are modified during an updating process. The Markov chain Monte Carlo (MCMC) method, which is a stochastic simulation method, is widely used to numerically solve a multi-dimensional integration problem by generating a series of random samples that target a posterior probability density function (PDF) (Robert & Casella, 2005; Ching, Muto, & Beck, 2006; Muto & Beck, 2008). In MCMC simulations, many sampling techniques have been developed such as Metropolis Hastings (MH) (Metropolis, Rosenbluth, Rosenbluth, Teller, & Teller, 1953; Hastings, 1970), transitional Markov chain Monte Carlo (TMCMC) (Ching & Chen, 2007), and hybrid Monte Carlo (HMC) (Duane, Kennedy, Pendleton, & Roweth, 1987) methods.

Although Bayesian model updating provides several advantages, in the research literature it is mostly applied to problems with numerically simulated data and relatively simple models. For research, simulated data and simple models are preferred because they allow researchers to have more control over problems with respect to the level of measurement noise and modeling errors. In contrast, full-scale FE models are widely used in industry to more precisely study structural behaviors under extreme loading conditions such as during earthquakes and hurricanes, as well as day-to-day operating conditions. However, the application of Bayesian model updating to large-scale operational civil structures with real data is very rare because of existing challenges (Behmanesh & Moaveni, 2015). The application of Bayesian model updating to full-scale and real measured data is more challenging because the level of uncertainties associated with modeling errors increases when many idealized connections, boundary conditions, and unknown material properties are included in FE models. In addition to the complexity of full-scale models, real measured data pose challenges because of unknown measurement noise and variations in identified natural frequencies and mode shapes.

In this chapter, Bayesian model updating of a full-scale FE model is conducted in an effort to expand its application to more practical and real problem. Specifically, the target is to minimize discrepancies in natural frequencies and mode shapes between the FE model and real measured data. 22 updating parameters, each of which modifies physical parameters whose effects on target natural frequencies are similar, are determined using sensitivity-based clustering. To generate samples for the posterior PDF, the HMC method is used since it is a powerful method for dealing with a high-dimensional parameter space and highly-correlated parameters. Then, the uncertainties of the updated parameters and the propagation of those uncertainties into the natural frequencies and mode shapes of the updated model are investigated.

Confidence intervals for the updated parameters and modal properties of the updated model are estimated at the end.

The chapter is organized as follows. Section 4.2 overviews the theoretical background of Bayesian model updating. In Section 4.3, HMC simulation is explained. Section 4.4 addresses the results of the Bayesian model updating of the full-scale FE model. In Section 4.5, the conclusions of the study are presented.

4.2 Overview of the Bayesian Model Updating Framework

In the Bayesian approach, the plausibility that each model class $\mathcal{M}$ is associated with data $\mathcal{D}$ is quantified by a joint probability density function, which is known as a posterior PDF. By Bayes' theorem, the posterior PDF is expressed as

$$p\left(\theta \mid \mathcal{D}, \mathcal{M}\right) = c^{-1} p\left(\mathcal{D} \mid \theta, \mathcal{M}\right) p\left(\theta \mid \mathcal{M}\right), \tag{4.1}$$

where θ is an updating parameter vector, and $c = p\left(\mathcal{D} \mid \mathcal{M}\right)$ is a normalizing constant that makes the integration of a posterior PDF over the parameter space become unity. $p\left(\theta \mid \mathcal{M}\right)$ is the prior PDF that provides the initial plausibility of the parameters θ associated with model class $\mathcal{M}$. In other words, the prior PDF is an assumed initial distribution of the updating parameters θ. $p\left(\mathcal{D} \mid \theta, \mathcal{M}\right)$ is the likelihood function, which is generally an error estimate (measure-of-fit) in model updating. The data $\mathcal{D}$ provides information about the updating parameters θ so that the estimation of the probability of the updating parameters θ becomes more accurate based on the given data $\mathcal{D}$. In this application, $\mathcal{D}$ represents the identified natural frequencies and mode shapes determined from the real measured data. The more data included in the

likelihood function in model updating, the more accurate is the model update result that can be achieved (Behmanesh & Moaveni, 2015). The posterior PDF $p\left(\theta \mid \mathcal{D}, \mathcal{M}\right)$ accounts for an updated distribution of parameters θ based on the assumed prior PDF and the given data $\mathcal{D}$.

Bayesian model updating requires that a multidimensional integration problem be solved. As an example, the normalizing constant c in Eq. 4.1 necessitates a multidimensional integration over the parameters space, which is defined as follows:

$$c = p(\mathcal{D}|\mathcal{M}) = \int p(\mathcal{D}|\theta, \mathcal{M}) p(\theta|\mathcal{M}) d\theta. \tag{4.2}$$

Since only one FE model is considered here, the model class $\mathcal{M}$ is dropped hereafter. Multidimensional integrations are also involved with the calculations of the marginal probability distributions of the updating parameters θ and the predictive PDF. When the dimensions of the parameter space becomes large, multidimensional integrations may be challenging when using an analytical approach. One solution is to use Laplace's method of asymptotic approximation. However, this requires a Gaussian assumption for the posterior PDF, which might not be reasonable in some cases. The most popular method for dealing with multidimensional integration problems is the stochastic simulation method. MCMC is a robust and efficient simulation technique for Bayesian model updating problems. MCMC generates sequence samples (a Markov Chain) that are consistent with a target posterior PDF. The main advantage of the MCMC method is that posterior samples can be generated by targeting an unnormalized posterior PDF, which means that the posterior PDF can be estimated without knowing the scaling factor, e.g., the normalizing constant c, of the posterior distribution. In the model updating problem, high probability regions of the posterior PDF are usually observed, where high probability is concentrated into a small volume

of the parameter space. This requires that posterior samples in the high probability regions be sufficiently generated by the MCMC methods to accurately estimate the posterior PDF.

The most well-known MCMC method is the MH method (Metropolis et al., 1953; Hastings, 1970). The drawbacks of this method are that the generation of samples can be inefficient in high probability regions, as well as in high dimensional problems. To overcome these drawbacks, the TMCMC method was introduced (Ching & Chen, 2007), which uses a sequence of intermediate PDFs that converge to a targeted PDF as the iterations continue. In each iteration, reweighting and resampling is performed to generate samples for an intermediate PDF, which can be used for the next iteration. For generating samples in a high probability region, the TMCMC method has advantage over the MH method due to its use of a sequence of intermediate PDFs. Furthermore, the TMCMC method is able to estimate a normalized constant c. However, the TMCMC method also has the potential to experience problems in higher dimensions (Cheung & Beck, 2009).

4.3 Overview of Hybrid Monte Carlo Simulations

The HMC method (Duane et al., 1987), which is also known as the Hamiltonian Monte Carlo, is the MCMC method that is most robust in dealing with high-dimensional problems (Cheung & Beck, 2009; Hanson, 2001). Many MCMC methods rely on a random-walk proposal distribution to generate the next consecutive sample from current samples in the Markov chain, which results in a slow exploration of the target PDF. For example, the MH method requires a prohibitively large number of samples to precisely construct the proposal PDF. The HMC method adopts a molecular dynamic (MD) trajectory in combination with the acceptance rule from the MH method.

The use of a dynamic trajectory enables the HMC method to avoid the random-walk behavior in samples, which is its major advantage. The avoidance of random-walk behavior permits the Markov chain to more efficiently search for a target distribution. The advantage of the HMC method becomes even more pronounced when parameters are highly correlated and the problem is highly dimensional.

In the HMC method, a fictitious dynamical system describes an object's motion in terms of its location $\theta \in \mathbb{R}^N$ and momentum $\mathbf{p} \in \mathbb{R}^N$ at a certain state t. The location θ values are the uncertain parameters within the targeted distribution $\pi(\theta)$, which is the posterior PDF in the model updating. The total energy of the dynamical system is conserved over time and is known as the Hamiltonian $H(\theta, \mathbf{p})$, which is the sum of the potential energy $U(\theta) = -\ln \pi(\theta)$ and the kinetic energy $K(\mathbf{p}) = \mathbf{p}^T \mathbf{M}^{-1} \mathbf{p}/2$. The mass matrix $\mathbf{M} \in \mathbb{R}^{N \times N}$ is a positive definite matrix.

A canonical distribution is used to relate the target PDF $\pi(\theta)$ to the Hamiltonian function $H(\theta, \mathbf{p})$. The canonical distribution for the Hamiltonian energy becomes

$$p(\theta, \mathbf{p}) \propto exp(-H(\theta, \mathbf{p})) = exp(-U(\theta))exp(-K(\mathbf{p})) = \pi(\theta)exp(\mathbf{p}^T \mathbf{M}^{-1} \mathbf{p}/2). \quad (4.3)$$

As shown in Eq. 4.3, $\pi(\theta)$ is independent of the distribution for the momentum $\mathbf{p}$. This also means that Hamiltonian dynamics can be used to generate samples targeting the joint canonical distribution $p(\theta, \mathbf{p})$ because $\pi(\theta)$ is proportional to $p(\theta, \mathbf{p})$. A common choice for the distribution of $\mathbf{p}$ is a zero-mean Gaussian distribution with a covariance matrix M. Furthermore, the target distribution $\pi(\theta)$ also can be an unscaled probability distribution since $\pi(\theta)$ is proportional to the joint distribution $p(\theta, \mathbf{p})$.

Hamiltonian dynamics are used as a proposal function for a Markov chain to generate samples that are consistent with the target PDF. According to Hamilton's

equations, the changes of θ and $\mathbf{p}$ over time t are determined by the partial derivatives of the Hamiltonian, which are:

$$\frac{d\mathbf{p}}{dt} = -\frac{\partial H}{\partial \theta} = -\nabla U(\theta), \tag{4.4}$$

$$\frac{d\theta}{dt} = \frac{\partial H}{\partial \mathbf{p}} = \nabla K(\mathbf{p}) = \mathbf{M}^{-1}\mathbf{p}. \tag{4.5}$$

For any time interval δt, the evolutions of θ and $\mathbf{p}$ can be numerically solved by Euler's method, a modified Euler's method, or the leapfrog method (Van Gunsteren & Berendsen, 1988). The leapfrog method is generally preferable and yields a better result in HMC simulations, as compared to the other methods (Neal, 2011), and is defined as follows:

$$\mathbf{p}\left(t + \frac{\delta t}{2}\right) = \mathbf{p}(t) - \frac{\delta t}{2}\nabla U\left(\theta(t)\right), \tag{4.6}$$

$$\theta(t + \delta t) = \theta(t) + \delta t\, \mathbf{M}^{-1}\mathbf{p}\left(t + \frac{\delta t}{2}\right), \tag{4.7}$$

$$\mathbf{p}\left(t + \delta t\right) = \mathbf{p}\left(t + \frac{\delta t}{2}\right) - \frac{\delta t}{2}\nabla U\left(\theta(t + \delta t)\right). \tag{4.8}$$

The algorithm of the HMC method is summarized in Figure 4.1. In each iteration, the momentum variable $\mathbf{p}$ is randomly generated from a predetermined distribution. In this application, the momentum variable p follows $\mathcal{N}(\mathbf{0}, \mathbf{M})$, where $\mathbf{M} = diag(0.3)$. It is worth mentioning that $\mathbf{p}$ is introduced as an auxiliary variable in order to facilitate the Markov chain path. One practical difficulty associated with the HMC method is the need for selecting suitable values for the step-size δt and the number of

Algorithm: Hybrid Monte Carlo

Input : Predetermined $\pi(\theta), \mathbf{M}, \delta t,$ and L, N
Output: N samples of θ

initialization: Set an initial location state θ_0, $i = 1$ and $j = 1$;
while $i < N$ **do**
  Sample $\mathbf{p}(t) \sim \mathcal{N}(\mathbf{0}, \mathbf{M})$;
  $\theta(t) = \theta_i$ and ;
  Repeat the leapfrog method L times with the step-size δt, starting from the current state $(\theta(t), \mathbf{p}(t))$;
  Obtain proposed states $\theta^* = \theta(t + L\delta t)$ and $\mathbf{p}^* = \mathbf{p}(t + L\delta t)$;
  Draw a random number $x \sim \mathcal{U}(0, 1)$;
  if $x \leq min(1, exp(H(\theta(t), \mathbf{p}) - H(\theta^*, \mathbf{p}^*))$ **then**
    $\theta_i = \theta^*$;
    $i = i + 1$;
  else
    $\theta_{rejected,j} = \theta^*$;
    $j = j + 1$
  end
end

Figure 4.1: Algorithm for the HMC method.

leapfrog steps L. The length of the trajectory at each iteration, represented as $L\delta t$, should permit samples to efficiently explore all of the distribution domain, rather than conduct a random walk. The two hyper-parameters mentioned above can be determined by considering an acceptance rate for the proposed states as well as the convergence of samples into a stationarity. Like the MH method, the HMC method also has an acceptance rule for a candidate sample. The optimal acceptance rate for the HMC method was proven to be 65% (Neal, 2011), which is higher than the optimal 23% acceptance rate for the MH method. Since it is practically challenging to identify δt and L such that the acceptance rate of the samples is identical to the optimal acceptance rate, an interval between 60% and 70% can be a reasonable range for an acceptance rate when $L > 1$. Computational expenses increases significantly with an increasing number of parameters θ and a value of L, due to the need to calculate partial derivatives.

4.4 Bayesian Model Updating of a Full-scale FE Model

4.4.1 Likelihood function and prior PDF

The updating parameter θ considered for Bayesian model updating here is the ones that determined by the sensitivity-based clustering method, which is defined in Section 3.6. In the likelihood $p(\mathcal{D} \mid \theta)$, the error function is modeled as a Gaussian distribution with a zero mean and an unknown variance σ^2. It is assumed that the errors in the natural frequencies and mode shapes are independent and the errors from different dynamic modes are also independent. The likelihood function used in

this application becomes

$$p(\mathcal{D} \mid \theta) = \frac{1}{(2\pi\sigma^2)^{N_m N_0/2}} \; exp\left(-\frac{1}{2\sigma^2}\sum_{j=1}^{N_o}\sum_{i=1}^{N_m} \; J_i(\theta, \mathcal{D}_j)\right), \tag{4.9}$$

where N_m is the number of dynamic modes considered in the updating process and N_o is the quantities of data set $\mathcal{D}$ included in the analysis. In this updating problem, the n_m value is 7 and N_0 is 4. It is noteworthy that the terms involving the unknown variance σ^2 in Eq. 4.9 are scaling factors of the posterior PDF. Without knowing the exact values of σ, posterior samples can be generated by the MCMC method since an unscaled distribution can be targeted to construct samples for the posterior PDF.

The error (measure-of-fit) function $J(\theta, \mathcal{D})$ is defined as the discrepancy between the identified natural frequencies and mode shapes from the measured data and those from FE models. Instead of matching the measured responses with the predicted ones from the FE model, which requires running many iterations of the FE model with respect to the number of response data points, the natural frequencies and mode shapes are used in the error estimation because this requires only one iteration of the FE model to evaluate an error function. However, when modal properties are used as targets in model updating, mode pairing should be properly carried out, which means that comparisons of modal properties obtained from measured data and FE models should be made only when they correspond to the same dynamic mode. $J_i(\theta|\mathcal{D}_j)$ is an error function with respect to the i^{th} mode and j^{th} set of data, which is defined as follows:

$$J_i(\theta, \mathcal{D}_j) = {r_f^i}^2(\theta, \mathcal{D}_j) + {\mathbf{r_s}}^i(\theta, \mathcal{D}_j)^T \; {\mathbf{r_s}}^i(\theta, \mathcal{D}_j). \tag{4.10}$$

$r_f \colon \mathbf{R}^{n_p} \rightarrow \mathbf{R}^{n_t}, \mathbf{r_s} \colon \mathbf{R^n} \rightarrow \mathbf{R^m}$. r_f is a natural frequency residual vector. $\mathbf{r_s}$ is a mode shape residual vector. n_p and n_t are the number of updating parameters and of the

dynamic modes considered in updating (targeted dynamic modes). n_m is equal to the product of the number of targeted dynamic modes and the number of DOFs of the mode shapes. The natural frequency residual vector $r_f^i(\theta, \mathcal{D}_j)$ represents relative errors in the natural frequencies with respect to the i^{th} dynamic mode and the data set $\mathcal{D}_j$, and is defined as

$$r_f^i(\theta, \mathcal{D}_j) = \frac{f_i(\theta) - \tilde{f}_{i,j}}{\tilde{f}_i}. \tag{4.11}$$

$\tilde{f}_{i,j}$ and $f_i(\theta)$ are the identified and computed natural frequencies of the i^{th} mode, respectively. The residual mode shape vector $\mathbf{r_s}^i(\theta, \mathcal{D}_j)$ is

$$\mathbf{r_s}^i(\theta, \mathcal{D}_j) = \text{MSF}\left(\phi_i(\theta), \frac{\tilde{\phi}_i}{\tilde{\phi_i}^r}\right)\phi_i(\theta) - \frac{\tilde{\phi}_i}{\tilde{\phi_i}^r}, \tag{4.12}$$

where $\tilde{\phi}_i$ and $\phi_i(\theta)$ are respectively the identified and computed mode shape vector. $\tilde{\phi_i}^r$ is a reference value, which is the maximum component of the vector $\tilde{\phi}_i$. Since the computed mode shapes have a different scale than the identified mode shapes, a modal scale factor (MSF) is used to change the scale of the computed mode shapes $\phi_i(\theta)$ in a such way that the difference with the maximum normalized identified mode shapes is minimized, with respect to the least-squares perspective (Allemang & Brown, 1982). The MSF is defined as

$$\text{MSF}\left(\phi_i(\theta), \tilde{\phi}_i\right) = \frac{\phi_i^*(\theta)\ \tilde{\phi}_i}{\|\phi_i(\theta)\|^2}, \tag{4.13}$$

where $\square^*$ denotes a complex conjugate transpose.

The prior PDF $p\,(\theta)$ is assumed to be an independent Gaussian distribution, and the means are equal to the values that minimize $-ln(p(\mathcal{D}|\theta))$. The standard deviation is 0.3, such that the prior PDF can reflect higher uncertainties for the updating

parameters. It is worth noting that the updating parameter θ_c cannot be less than -1, where the corresponding physical parameter X^c becomes negative, such as the Young's modulus, spring coefficient, and mass density. Negative physical parameters lead to an FE model that does not remain in a physically meaningful range. In this model updating, the bounds that ensure the updating parameters remain physically meaningful are taken into consideration. The likelihood function becomes zero when $\theta < 1$. This condition is equivalent to one in which there is zero probability of having negative values for the physical parameters after model updating.

4.4.2 Generated posterior samples by the HMC simulation

The HMC simulation generates 2000 posterior samples that are consistent with the unscaled posterior PDF, which is proportional to the product of the likelihood function and the prior PDF. In the simulation, the initial location state θ_0 is determined in a such way that it minimizes potential energy $U(\theta)$. This initial state enables the Markov chain to start around a high probability region of the target PDF, making the exploration of the target PDF more efficient (Cheung & Beck, 2009). The interior point method (Byrd et al., 1999) solves the optimization problem of finding the initial state θ_0. In the leapfrog method, the gradient of the potential energy with respect to θ is calculated numerically to determine a proposal state. The two hyper-parameters L and δt in the HMC simulation are selected to be 2 and 0.1, respectively. These selected hyper-parameters lead to an average acceptance rate of 70%, which is within the reasonable interval [60% to 70%]. The posterior 2000 samples are the accepted samples, as based on the acceptance rule of the HMC method. Accepted posterior samples (θ_1 - θ_{22}) are shown in Figure 4.2. The y-axes of the plots are the updating parameters defined in Eq. 3.1.

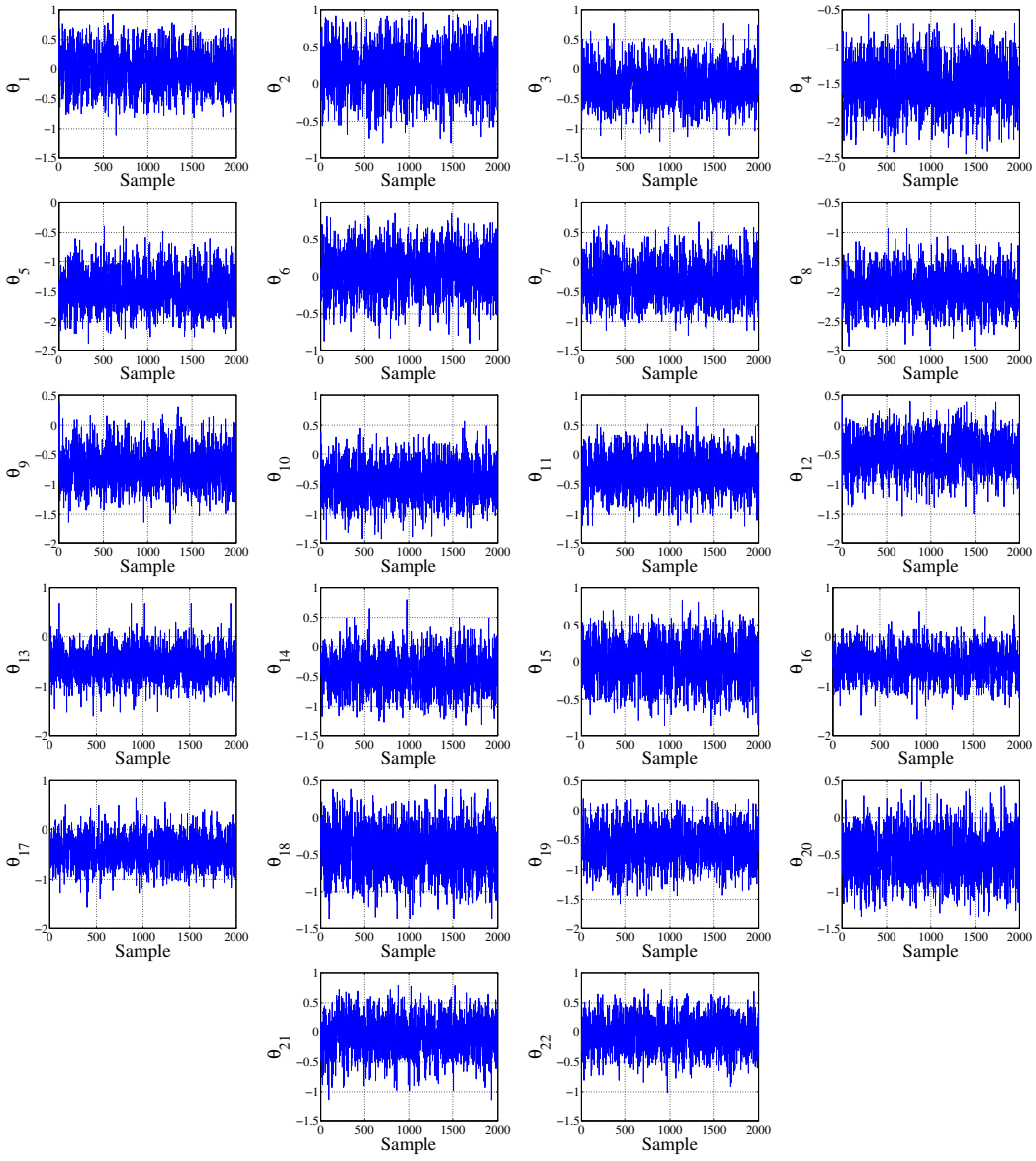

Figure 4.2: Posterior samples (θ_1 - θ_{12}) generated by HMC simulation.

Moving means and standard deviations of the samples are calculated to verify the convergence of the Markov chain to stationarity. A window length of 400 data points was used in the calculation of the moving means and standard deviations. The moving means and standard deviations associated with θ_3, θ_6, and θ_{22} are shown in Figure 4.3. The y-axes of Figures 4.3ab are an updating parameter defined by Eq. 3.1 and a standard deviation. The first 200 samples are in the burn-in period where the samples converge to stationarity. After the burn-in period, the mean values converge to parameters that minimize the error between the measured data and the FE model. The standard deviation also converges to a certain value depending on the reduction of the uncertainty after model updating. The burn-in samples are excluded in the estimation of the posterior PDFs. Furthermore, there is no random walk behavior in the generated samples, i.e., there is no significant zig-zag behavior in the moving means, which, as mentioned above, is the main benefit of using the HMC method. The samples from the HMC method are more efficient and robust since they have relatively stable moving means and standard deviations.

4.4.3 Correlation between updating parameters

The correlation between the updating parameters is also studied based on the generated posterior samples. It is found that all updating parameters are uncorrelated, which is the same as the assumption of independent distributions in the prior PDFs. Three examples of the pairwise posterior samples are shown in Figure 4.4 to demonstrate that the three updated parameters (posterior samples) θ_3, θ_6, and θ_{22} are uncorrelated. It can be clearly seen that there is no linear or nonlinear relationship between these two parameters. The correlation coefficient matrix for all the updating parameters is shown in Figure 4.5. In the figure, the x and $y-$axes are indexes of

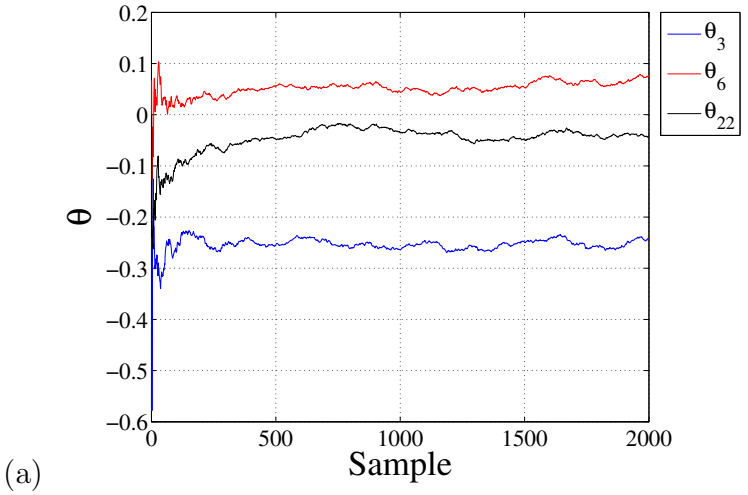

(a)

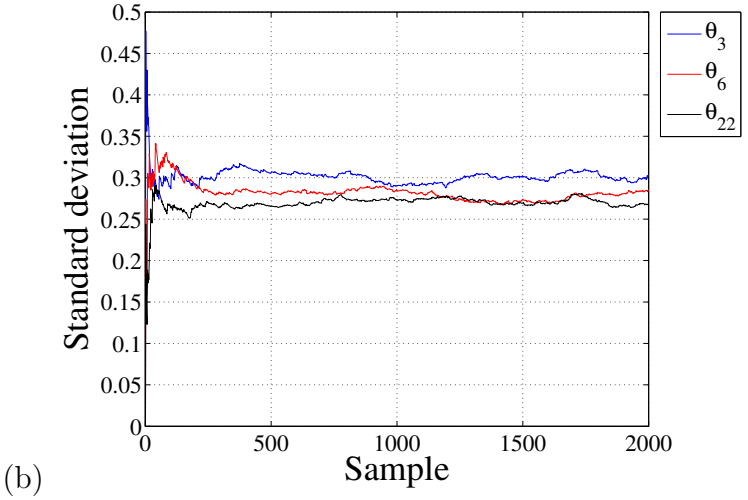

(b)

Figure 4.3: Convergence to stationarity for selected updating parameters (θ_3, θ_6, and θ_{22}): (a) moving averages; and (b) moving standard deviation.

the updating parameters. All off-diagonal values of the correlation coefficient matrix are less than 0.1, which means that the updated parameters are uncorrelated with each other. It is noteworthy that an assumption that is made for the prior PDFs (independent Gaussian distributions in this study) does not necessarily lead to uncorrelated updating parameters (posterior samples). For example, in the study done by (Cheung & Beck, 2009), it was observed with the posterior PDFs that some stiffness parameters were highly correlated and non-Gaussian, which were different from the independent Gaussian prior PDFs. The ability of Bayesian model updating to capture correlations between updating parameters can provide meaningful physical insights for a proper parameterization in model updating.

4.4.4 Probabilities of the updated parameters and the variations of the natural frequencies and mode shapes of the FE model

The posterior samples, excluding the burn-in samples, are used to estimate the probabilities of the updated parameters. Histograms of the updated parameters θ_3, θ_6, and θ_{22} are shown in Figure 4.6. Kernel density estimation with a normal kernel function is carried out to obtain the marginal PDFs and the cumulative distribution functions (CDFs) of the updated parameters. The estimated marginal PDFs and CDFs of the updated parameters θ_3, θ_6, and θ_{22} are shown in Figure 4.7. It is obvious that some updated parameters (the posterior PDFs) do not exactly follow a Gaussian distribution although Gaussian assumptions are made in the likelihood function and the prior PDF. Bayesian updating using Laplace's asymptotic approximation (J. L. Beck & Katafygiotis, 1998), which assumes a Gaussian distribution for the posterior PDFs, cannot be appropriate for this problem since the estimated marginal posterior PDFs

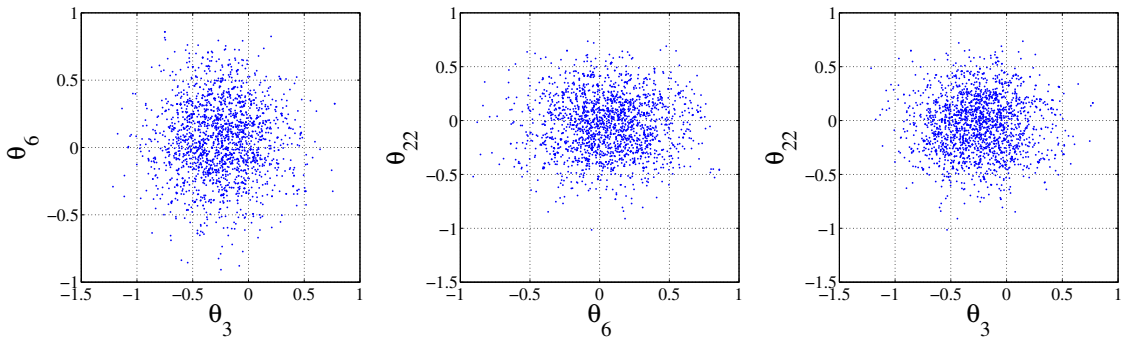

Figure 4.4: Pairwise plots for selected posterior samples (θ_3, θ_6, and θ_{22}).

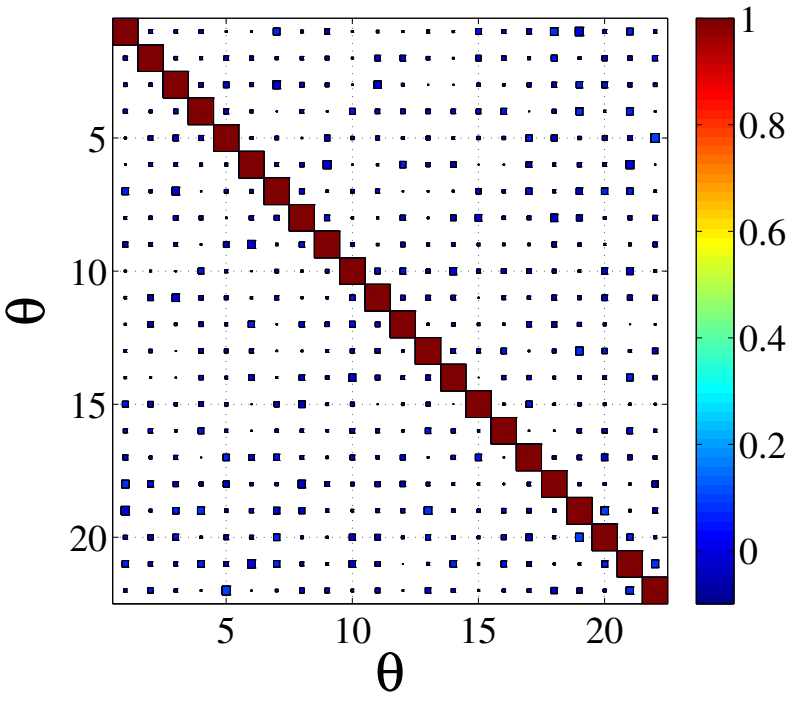

Figure 4.5: Pairwise plots for selected posterior samples (θ_3, θ_6, and θ_{22}).

are non-Gaussian. Understanding the non-Gaussian behavior of the posterior PDF is important for making robust predictions of structural responses and reliabilities.

Based on the estimated marginal CDFs, 95% confidence intervals are calculated for the updated parameters (posterior samples), as shown in Figure 4.8. The mean values of the updated parameters are marked with circles. The $x-$axis of the figure is the index of the updating parameter θ. The $y-$axis is the values of the updated parameters, which are defined by Eq. 3.1. The updating parameters whose values are equal to zero account for the initial physical parameters of the FE model. The negative values of the updated parameters mean that the corresponding physical parameter values increase during the modification.

After the Bayesian model updating, a reduction in the uncertainties associated with the updating parameters is observed. The standard deviations of the updated parameters are summarized in Table 4.1. Compared to the prior uncertainties, the posterior uncertainties (standard deviations) are reduced, since the data sets $\mathcal{D}$ in the likelihood function provide information about the distribution of the parameters θ. The uncertainties of the updated parameters θ_6, θ_{15}, and θ_{22} are reduced more than those of the other parameters. The parameters that have greater reductions in their uncertainties are the stiffness-related parameters, which also make comparatively more dominant contributions to the target natural frequencies, i.e., the natural frequencies of the FE model are more sensitive to those parameters. The sensitivities of the natural frequencies corresponding to the updating parameters are shown in Figure 4.9. Some of the mass density updating parameters ($\theta_1 - \theta_5$) also have a dominant effect on the target natural frequencies. However, the uncertainty reduction associated with the mass densities is relativity low, despite the sensitivity of the natural frequencies to the mass densities. A relatively smaller degree of reduction in the mass parameters was also observed in (Cheung & Beck, 2009).

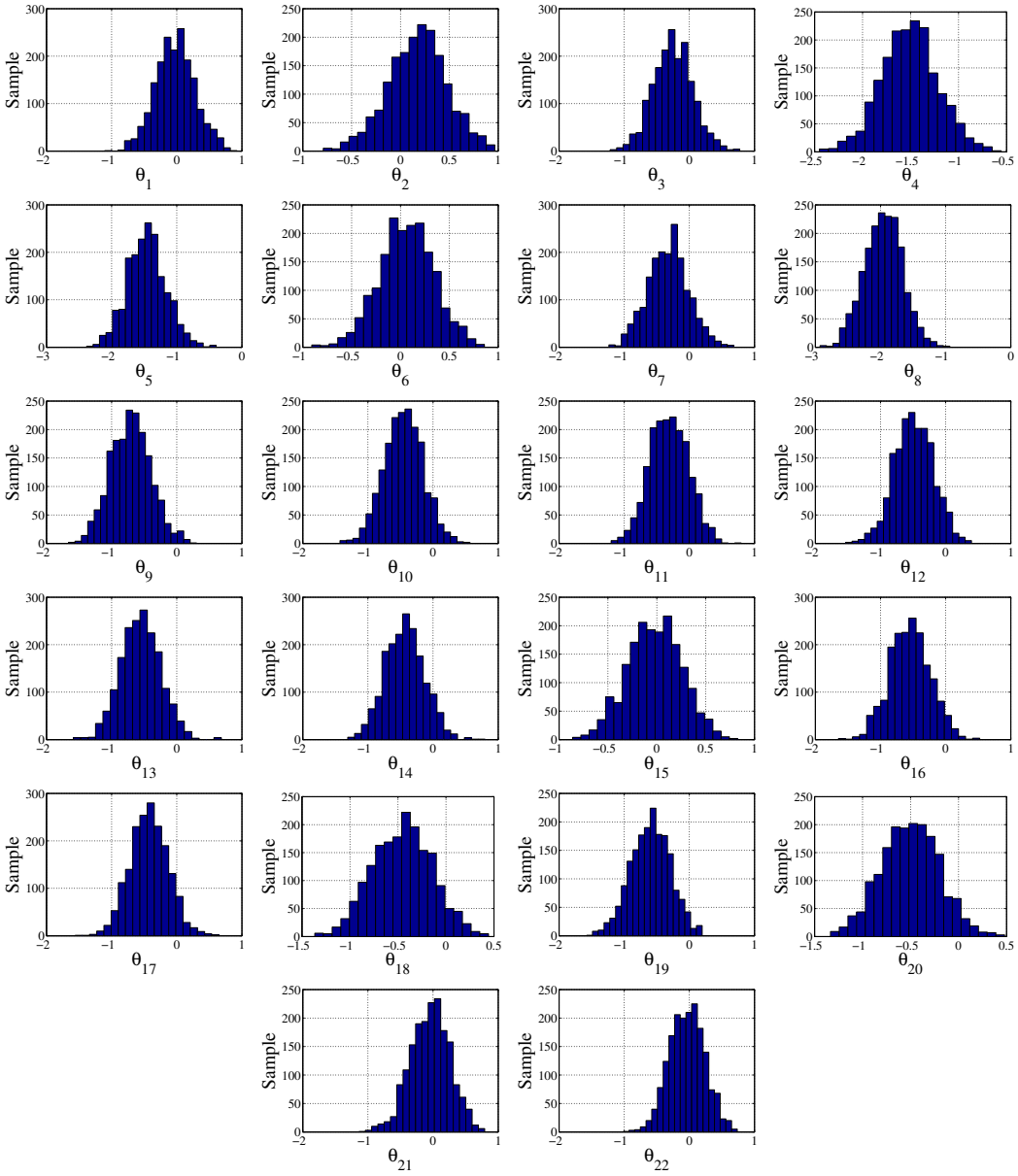

Figure 4.6: Histograms of the updated parameters (posterior samples) θ_1 - θ_{22}.

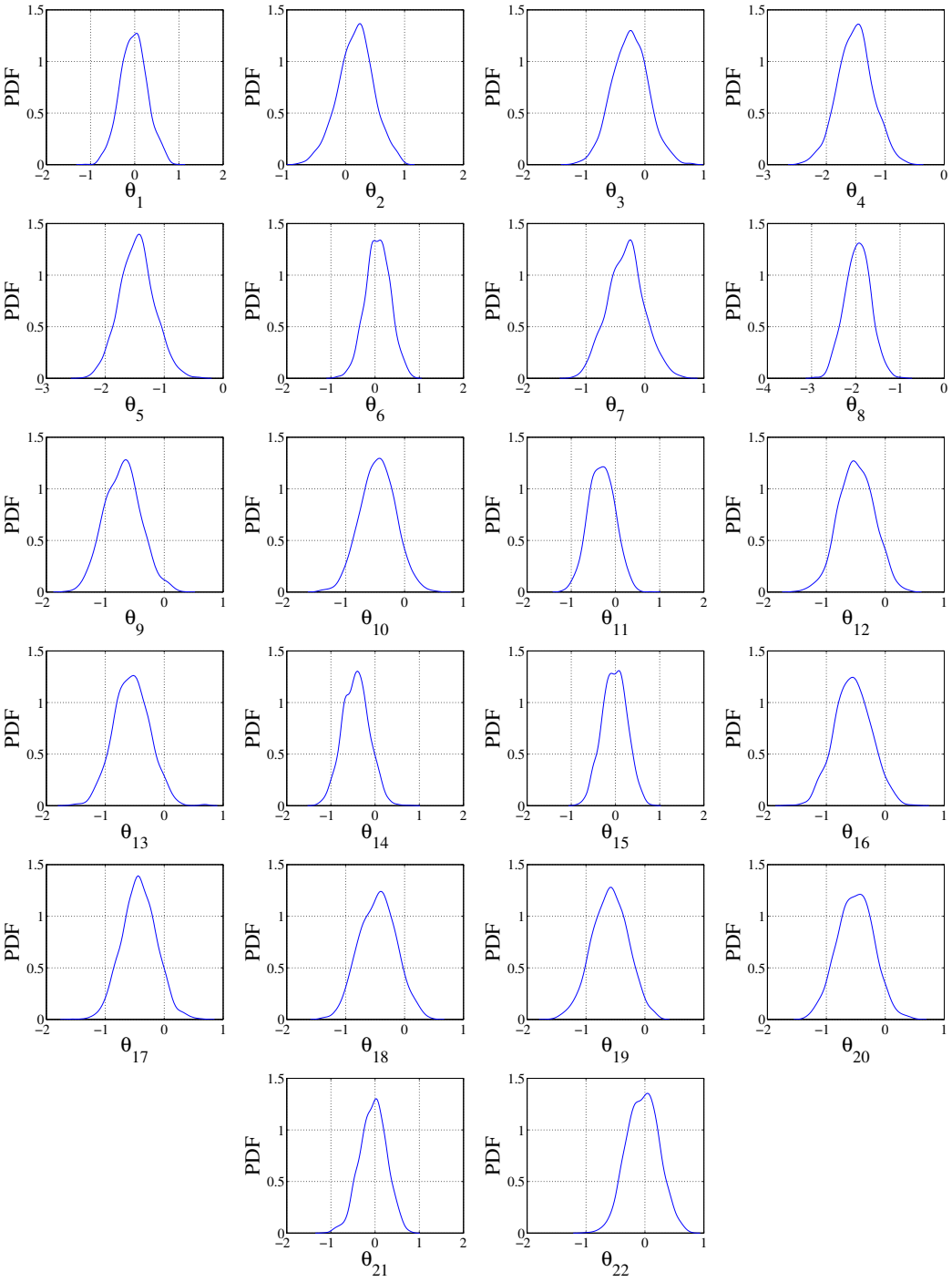

Figure 4.7: Kernel density estimation: PDFs of updated parameter θ_1 - θ_{22} estimated by KDE.

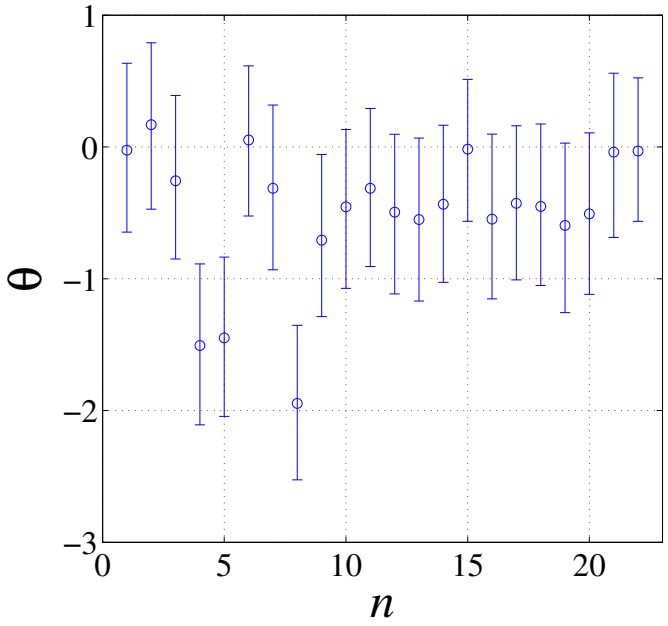

Figure 4.8: 95% confidence intervals for the updated parameters (posterior samples).

Table 4.1: Statistical results of the posterior samples and uncertainty reductions after Bayesian model updating (the standard deviations of the prior PDFs is 0.3).

Parameter	Mean	STD	MAP	Parameter	Mean	STD	MAP
θ_1	-0.025	0.311	0.025	θ_{12}	-0.495	0.300	-0.532
θ_2	0.169	0.300	0.254	θ_{13}	-0.551	0.307	-0.494
θ_3	-0.256	0.300	-0.258	θ_{14}	-0.435	0.296	-0.398
θ_4	-1.507	0.298	-1.453	θ_{15}	-0.017	0.267	0.015
θ_5	-1.449	0.296	-1.427	θ_{16}	-0.548	0.306	-0.576
θ_6	0.053	0.278	-0.043	θ_{17}	-0.428	0.292	-0.442
θ_7	-0.314	0.301	-0.250	θ_{18}	-0.452	0.307	-0.388
θ_8	-1.946	0.291	-1.920	θ_{19}	-0.596	0.313	-0.570
θ_9	-0.708	0.299	-0.625	θ_{20}	-0.507	0.305	-0.601
θ_{10}	-0.455	0.299	-0.431	θ_{21}	-0.040	0.304	0.034
θ_{11}	-0.314	0.297	-0.280	θ_{22}	-0.031	0.272	0.050

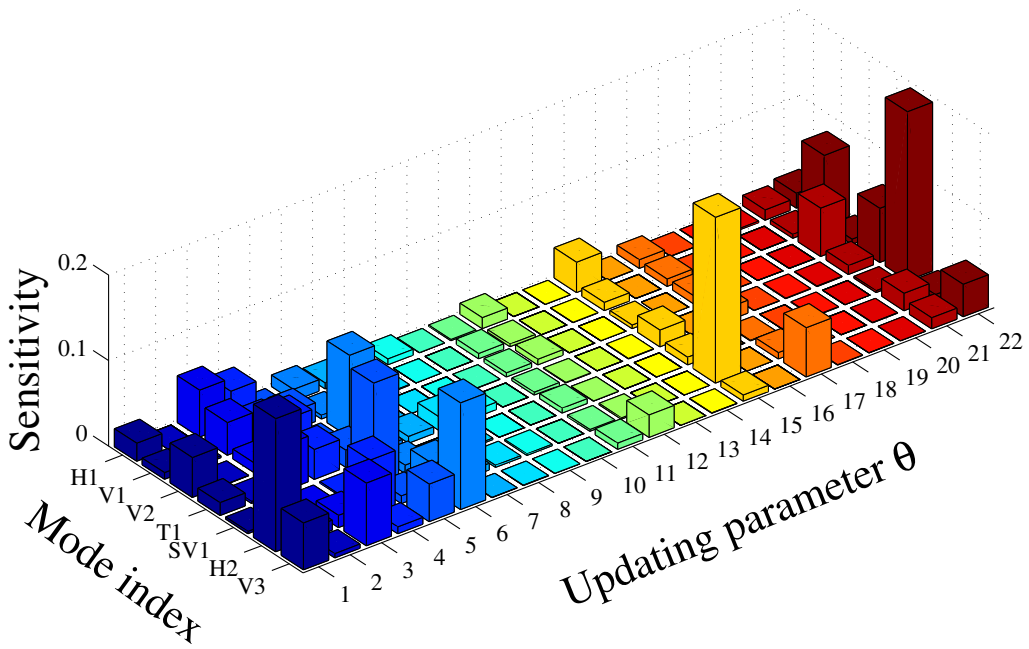

Figure 4.9: Sensitivity matrix of natural frequencies with respect to updating parameters θ (more uncertainty reductions for θ_6, θ_{15}, and θ_{22} as shown in Table 4.1).

The generated posterior samples are also used to study how the uncertainties of the updated parameters are propagated into the uncertainties of the natural frequencies and mode shapes of the FE model. The ability to compute the propagation of the uncertainties (the variabilities of the modal properties of the model) is one of the advantages of the multiple solutions of Bayesian model updating. Figure 4.10 shows histograms of the natural frequencies computed from the FE model and the corresponding marginal PDFs obtained by the kernel density estimation. The $x-$axis is the natural frequencies of the FE model. Two $y-$axes are shown in the figure: one is the number of the samples and the other is a probability based on the kernel density estimation. Figure 4.11 shows histograms and the marginal PDFs associated with the MAC values between the identified mode shapes and those computed from the FE model. Relatively fewer variations in the natural frequencies and the mode shapes are observed in the lower dynamic modes because the higher dynamic modes are more sensitive to the perturbation of the parameters.

4.4.5 Modeling error reductions after Bayesian model updating

Maximum a posteriori (MAP) estimation is carried out to select the updating parameters that minimize the modeling errors of the initial FE model. The maximum values of the marginal posterior PDFs, which are the MAP estimates, are summarized in Table 4.1. Table 4.2 compares the natural frequencies and the MAC values between the initial FE model and the updated model based on the MAP estimates. The second column of the table shows the mean values of the identified natural frequencies from the measured data. The third and fifth columns of the table are the natural frequencies from the initial FE model and the updated FE model, respec-

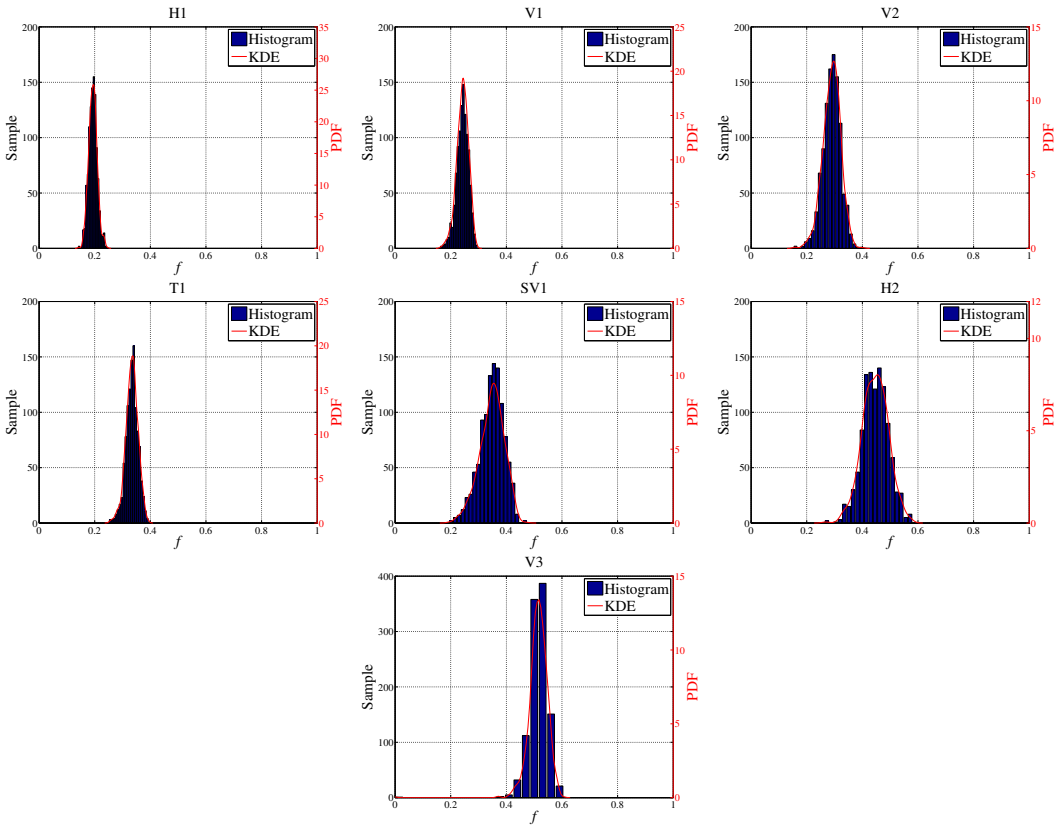

Figure 4.10: Variation of the natural frequencies of the FE model for selected modes (H1, V1, V2, T1, SV1, H2, and V3): histograms and PDFs estimated by KDE.

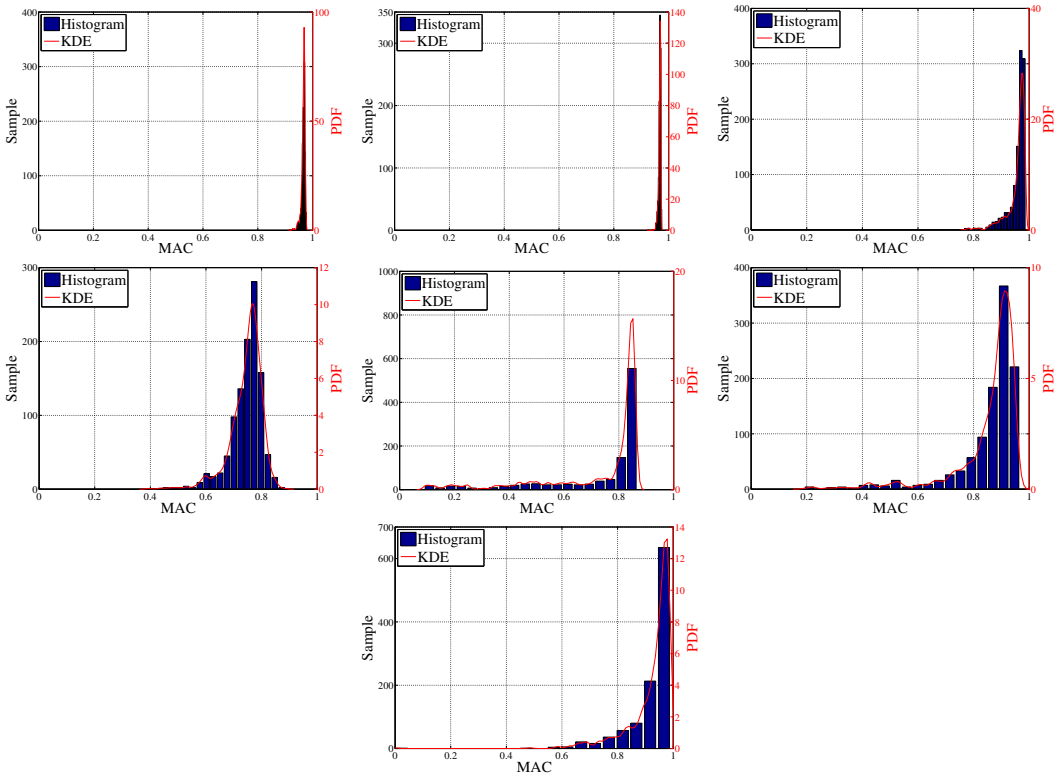

Figure 4.11: Variation of the MAC values between the identified model shapes and those from the FE model for selected modes (H1, V1, V2, T1, SV1, H2, and V3): histograms and PDFs estimated by KDE.

tively. It is clear that most of the initial discrepancies in the natural frequencies significantly decrease during the model updating process, although the match in the natural frequencies of the first torsional mode is not satisfactory. An unsatisfactory updating result with the first torsional mode is also observed with the deterministic model updating of the same bridge model under considered here; a possible reason for the unsatisfactory updating result is provided in Section 3.7. The means of the MAC values calculated between the four identified mode shapes and those from the initial FE model are summarized in the seventh column of the table. Compared to the initial MAC values, the mode shape matches are also improved during the model updating process, especially for the higher modes.

Table 4.2: Natural frequencies and the MAC values of the FE model after Bayesian model updating.

Mode	Frequency				MAC value		
	Hz						
	Identified	Initial FE	Relative error	MAP	Relative error	Initial FE	MAP
H1	0.194	0.2340	0.207	0.197	0.017	0.981	0.968
V1	0.227	0.2940	0.296	0.241	0.063	0.963	0.969
V2	0.303	0.3520	0.162	0.303	0.001	0.948	0.962
T1	0.373	0.3840	0.029	0.335	0.103	0.776	0.746
SV1	0.337	0.4520	0.340	0.341	0.012	0.839	0.763
H2	0.450	0.5390	0.197	0.456	0.013	0.847	0.867
V3	0.500	0.5980	0.197	0.524	0.049	0.861	0.986
	Total relative error		1.428		0.256		

4.5 Conclusions

In this study, a full-scale FE model with 22 updating parameters is updated using the Bayesian model updating scheme. The sensitivity-based cluster analysis is

a robust method for selecting an efficient set of updating parameters based only on the physical definition of the parameters. The updating parameters selected by the analysis enabled the grouping of the physical parameters whose effects on the target frequencies are similar. The HMC simulation successfully generated samples for the high-dimensional problem under consideration here. Furthermore, the posterior samples from the HMC simulation were more effective since there is no random walk behavior in the samples.

The multiple solutions obtained by Bayesian model updating permit the estimation of not only the probabilistic measures of the updated parameters, but also the uncertainty propagation of those parameters to the natural frequencies and mode shapes of the FE model. In general, providing multiple solutions to users of FE models is beneficial, since the best solution for meeting the particular application needs and technical considerations can be chosen between a number of possible solutions given by the Bayesian model updating. The MAP estimates of the updating parameters (posterior samples) lead to an FE model whose natural frequencies and mode shapes are in better agreement with those from measured data.

In the Bayesian model updating here, four measured data sets provided information about the distributions of the updating parameters. Although the estimation of the probabilities of the updating parameters and the variabilities of the modal properties of the FE model can be improved by including more data into the problem, this was not able to do here so due to the limited availability of measured data. Also, the assumed prior PDF in this study depended on the optimization solution of the error function to yield a better assumptions about the updating parameters, because of the limited measured data and the large initial modeling error. A different assumption for the prior PDF, such as a uniform distribution, can be used to compare an updating result for a different selection of assumptions. Furthermore, a Bayesian two-stage

formulation (Au & Zhang, 2016; F.-L. Zhang & Au, 2016), which has the capability of considering structural modeling errors during an updating process can be applied to the FE model updating practice.

Chapter 5

Temperature Effects on Natural Frequencies

In real-world applications of vibration-based damage detection methods, it becomes fundamentally very important to distinguish changes in the dynamics of structures due to structural damage from those due to the environmental effects. Modal properties of structures are widely used as damage sensitive features which indicate changes in physical properties due to structural damage or degradation. However, civil structures are under various operational and environmental conditions, such as traffic, wind, humidity, and most importantly temperature, which also change modal properties of structures in addition to structural damage. Changes in natural frequencies due to the environmental effects have also been observed with the identified natural frequencies of the bridge considered here, which are demonstrated in Section 2.2. Changes in modal properties caused by the environmental effects can mask counterparts due to structural damage, resulting in an unreliable structural damage assessment. Therefore, it is fundamentally important to understand the relationships between the environmental effects and modal properties.

5.1 Background

Variations in modal properties due to environmental and operational conditions such as wind, traffic, humidity, and temperature have been rigorously investigated in the last few decades (Peeters & De Roeck, 2001; Kim, Yun, & Yi, 2003; Sohn, 2007; Moser & Moaveni, 2011; Magalhaes, Cunha, & Caetano, 2009; Macdonald & Daniell, 2005; Xu, Chen, Ng, Wong, & Chan, 2010). Among those environmental and operational effects, temperature is, in general, the most influential source for the variations in natural frequencies of structures (Zhou, Ni, & Ko, 2010; Moser & Moaveni, 2011). The variations in natural frequencies due to temperature have been widely observed with real measured data over daily and annual cycles. The first three natural frequencies of the Alamosa Canyon Bridge varied about 5% over 24 hours (Cornwell, Farrar, Doebling, & Sohn, 1999). The natural frequencies of the Ting Kau Bridge fluctuated in the range of 1.7 and 6.7% over a year period as temperature changed between 3 and 53°C (Zhou et al., 2010; Hua, Ni, Ko, & Wong, 2007; Ni, Hua, Fan, & Ko, 2005). The first six natural frequencies of the Dowling Hall Foot Bridge varied by 4-8% over a 16 week period as temperature ranged from -14 to 39°C (Moser & Moaveni, 2011). During a sixteen-day monitoring of the Tianjin Yonghe Bridge, the natural frequencies of the first and fourth bending modes fluctuated by 3.155 and 1.470%, respectively, when ambient temperature ranged from -11.5 to 3.7°C (Li, Yao, Yao, & Xu, 2010). A bilinear behavior in the relationship between temperature and natural frequencies, where a kink is located around 0°C, is observed in data sets measured from the Z24 Bridge (Peeters & De Roeck, 2001) and the Dowling Hall Footbridge (Moser & Moaveni, 2011). The temperature effect on natural frequencies is also observed from a laboratory test. Xia, Hao, Zanardo, and Deeks (2006) conducted an ambient dynamic test on a reinforced concrete slab for nearly two years and found that natural

frequencies of bending modes decreased 0.13 - 0.23% as temperature increased by 1°C. Kim, Park, and Lee (2007) carried out a series of forced vibration tests on a small-scale bridge model subjected to various temperature and found that the first four natural frequencies decreased by 0.64, 0.33, 0.44, and 0.22%, respectively when temperature increased per unit degree. Balmès et al. (2008) performed a laboratory test with a clamped beam within a climatic chamber and demonstrated that the first four natural frequencies increased by 16, 8, 5, 3% as an ambient temperature decreased by 17°C.

Regression analysis has been conducted to understand the relationships between natural frequencies and temperature changes. Linear, nonlinear, and machine learning models have been used to model the temperature effects on natural frequencies. Sohn et al. (1999) presented an adaptive filter consisting of multiple linear regression models and demonstrated its applicability using data measured from the Alamosa Canyon Bridge. Xia et al. (2006) applied a linear regression model to temperature versus natural frequency data obtained from a laboratory test and observed that there was a good linear correlation between average temperature and natural frequencies. Peeters and De Roeck (2001) applied an autoregressive model with exogenous inputs (ARX) model to one-year continuous monitoring data of the Z24 Bridge in an effort to consider time-dependent temperature effects on natural frequencies such thermal dynamics. Moser and Moaveni (2011) compared the performances of linear, bilinear, ARX, and polynomial models based on continuous monitoring data sets of the Dowling Hall Footbridge and concluded that a fourth-order polynomial model without cross terms performed the best. Ni et al. (2005) and Ni, Zhou, and Ko (2009) applied the support vector machine (SVM) and neural network models, which are machine learning models, to long-tern monitoring data of the Ting Kau Bridge and intensively studied their generalization capabilities.

In this section, the full-scale FE model, which is described in Section 2.3, is used

to conduct a controlled simulation-based study on temperature effects on natural frequencies. Thermal prestress induced due to temperature changes is used to model temperature effects on natural frequencies. A method that randomly generates spatial temperature variations over a bridge model is introduced. With randomly generated temperature variations and prestress modeling, data sets of natural frequencies with respect to various spatial temperature variations are obtained by the FE model. Based on simulated data sets (temperatures versus natural frequencies), linear regression and three machine learning methods (SVM, neural network, and random forest) have been used to describe the relationships between temperatures and natural frequencies.

5.2 Modeling of thermal effects on natural frequencies

Temperature changes in structural components affect local and global stiffness matrices of a structure and thus cause natural frequency fluctuations over different temperature conditions. Modeling how temperatures alter the stiffness of a structure is required to simulate temperature effects on the natural frequencies. One of ways to model this is through the use of a temperature-dependent modulus of elasticity, which is adapted in a simulation of a simple bridge model conducted by Yan, Kerschen, De Boe, and Golinval (2005). In this approach, the relationships between an elasticity modulus (Young's modulus) of a material and temperature are assumed. Then, elasticity moduli of structural components of an FE model are calculated and changed with respect to the corresponding temperatures of structural components. The other approach to model temperature effects on natural frequencies is through imposing thermal prestresses to structural components. The temperature effect mod-

eling using thermal prestress is demonstrated by Balmès, Corus, Siegert, et al. (2006). In this approach, changes in the temperatures of structural components generate a thermal expansion of structural materials based on the thermal expansion coefficient α and a temperature change ΔT. If boundary conditions of structural components are fixed, a thermal expansion induces thermal stress.

As an example, free vibrations of a prestressed Euler-Bernoulli beam are governed by the partial differential equation shown as

$$EI\frac{\partial^4 W(x,t)}{\partial x^4} + m\frac{\partial^2 W(x,t)}{\partial t^2} - N\frac{\partial^2 W(x,t)}{\partial x^2} = 0, \tag{5.1}$$

where $x \in [0, l]$; E is the modulus of elasticity; I is the second moment of area for the cross section; $W(x,t)$ is the deflection of the beam; m is the mass per unit length; and N is the quasistatic axial load. When a beam has a simple support at both ends, the boundary conditions become

$$W(x,t)|_{x=0,l} = 0. \tag{5.2}$$

Since the boundaries are constrained and the beam cannot expand, the axial load N can be induced due to the temperature change ΔT, which is given as follows:

$$N = A\sigma_T, \quad \sigma_T = E\epsilon_T, \quad \varepsilon_T = \alpha\Delta T, \quad \Delta T = T_{ref} - T, \tag{5.3}$$

where A is cross sectional area; σ_T is the thermal stress; ε_T is the thermal strain; and T_{ref} is the reference temperature that is measured when no prestress is imposed. The third term of the left-hand side of Eq. 5.1 accounts for the contribution of prestress (axial load) for the beam formulation. By solving Eq. 5.1 with the boundary conditions (Eq. 5.2), one can obtain the i^{th} eigenvalue w_i^2 of the prestressed beam, which

is

$$w_i^2 = \sqrt{\frac{EI(i\pi/L)^4 + N(i\pi/L)^2}{m}}. \tag{5.4}$$

It is clear to see that the natural frequency w is the function of the axial load N which is calculated from the thermal stress σ_T.

To include the modeling of thermal effects using thermal prestress in the FE model under consideration here, thermal prestress σ_T for each element of the FE model is calculated based on the thermal expansion coefficient α and the corresponding temperature T. T_{ref} is set to be the mean of air temperatures corresponding to the identified natural frequencies demonstrated in Section 2.2. The thermal coefficient α is defined to be 1.1×10^{-5}. Then, calculated prestresses for all structural components of the FE model are defined as initial conditions. Since thermal stress causes the P-Delta effect, geometrical nonlinearity needs to be considered in this simulation. The modeling of the temperature effects on natural frequencies using thermal prestress is verified with an FE model of a simply supported prestressed beam by comparing its natural frequencies with analytic solutions which is given in Eq. 5.4.

The modeling of the thermal effects on the natural frequencies using thermal prestress is compared with one using temperature-dependent Young's modulus. In this comparison, the temperatures of the deck of the FE model are uniformly changed from 0°C to 40°C with an increment of 1°C. When it comes to the modeling of the thermal effects using the temperature-dependent Young's modulus, it is assumed that the Young's modulus of each element of the FE model is to linearly change due to the temperature change ΔT. The Young's modulus of each element E^e is calculated as:

$$E^e = E_{ref}(1 - \beta\Delta T), \tag{5.5}$$

where E_{ref} is the Young's modulus corresponding the reference temperature T_{ref} and β is the reduction factor, which is assumed to be 2.521×10^{-4} based on ASME B31.b (ASME, 2007). The natural frequencies of the FE model are calculated based on the temperature-dependent Young's moduli estimated from the temperature changes ΔT. For the modeling of the thermal effects using thermal prestress, prestress σ_T for each element due to the thermal expansion is calculated by Eq. 5.3 and is defined as an initial condition in the FE model analysis. By taking the thermal prestress field into account, the corresponding natural frequencies are evaluated with respect to the spatially-uniform temperature changes from 0°C to 40°C.

Table 5.1 summarizes the variations in the natural frequencies associated with the two modeling approaches when the FE model is subjected to the spatially-uniform temperature changes of the deck, as well as the variations in the identified natural frequencies. It was found that the relationships between the uniformly-distributed deck temperatures and the natural frequencies are fairly linear. Thus, the natural frequencies corresponding to 0 and 40°C are summarized in the table. The second and third columns demonstrate the results of the modeling using thermal prestress. The fifth and sixth columns show the results using the temperature-dependent Young's modulus. The maximum relative changes versus natural frequencies at the reference temperature T_{ref} are shown in the fourth and seventh columns of the table. The variations in the identified natural frequencies are calculated versus their means. It is noteworthy that the variations in the identified natural frequencies are not only due to temperatures, but also due to traffic. No significant variations in the mode shapes are observed with the simulations using both modeling approaches. This is also observed with real measured data in the other studies (Xia et al., 2006; Moser & Moaveni, 2011; Balmès et al., 2008).

The thermal prestress modeling provides a more reasonable result, compared to

Table 5.1: Variation in the natural frequencies associated with the thermal effects using thermal prestress and temperature-dependent Young's modulus.

Mode	Theraml prestress			Temperature-dependent Young's modulus			Identified
	Frequency [Hz]		Variation [%]	Frequency [Hz]		Variation [%]	Variation [%]
	40°C	0°C		40°C	0°C		
H1	0.1918	0.2022	3.1900	0.1976	0.1983	0.2524	6.2814
V1	0.2428	0.2547	2.8920	0.2494	0.2504	0.2400	4.0776
V2	0.2843	0.3046	4.1660	0.2958	0.2972	0.3033	1.2219
T1	0.3172	0.3260	1.6770	0.3217	0.3230	0.2790	0.3416
SV1	0.3352	0.3495	2.5240	0.3428	0.3445	0.3199	1.4151
H2	0.4564	0.4679	1.5150	0.4623	0.4639	0.2374	0.6386
V3	0.5083	0.5259	2.0860	0.5179	0.5198	0.2312	1.5813

the one using the temperature-dependent Young's modulus. This is due to two following reasons. First, it produces a more realistic magnitudes of the frequency variations. In contrast, the magnitudes of the frequency variations obtained by the modeling with the temperature-dependent Young's modulus are too small to account for the thermal effects on the natural frequencies. Furthermore, the other reason is that the thermal prestress modeling provides more meaningful variations for dynamic modes. From the identified natural frequencies, the first torsional (T1) and the second lateral mode (H2) have relatively fewer variations, compared to the other modes. This phenomenon is also observed with the simulated results using the thermal prestress modeling, which means that the natural frequency variations obtained by the thermal prestress modeling are more representative of the observed variations in the natural frequencies. Therefore, the thermal prestress is used for the modeling of the thermal effects on the natural frequencies hereafter.

5.3 Spatial variations in temperatures over the bridge

When studying the temperature effects on natural frequencies, it is important to properly consider the spatial variations of temperatures across a bridge. The temperatures of structural components can be different with respect to their structural locations and the orientation of the sun. The bridge under consideration here is roughly oriented from east to west. During the morning, the east side of the bridge can receive the larger amount of solar radiation, compared to the other side of the bridge, resulting in higher temperatures on the east side. In the afternoon, this can be opposite (higher temperatures on the west side of the bridge). It is also possible to have relatively higher temperatures on the main span based on the orientation of the sun. Temperature distributions across the bridge also can be similar when there is no significant sunlight on the bridge due to weather conditions or at night. The spatial variations of temperatures have been widely observed with real measurements of temperatures (Moser & Moaveni, 2011; Zhou et al., 2010). Zhou et al. (2010) observed that the maximum temperature difference across the deck of the Ting Kau Bridge was 22.49°C.

In this study, no direct measurements of temperatures of the structural components are available. Therefore, the temperatures distributions of the structural components are randomly generated so that temperature versus natural frequency data can be obtained by the FE model analysis with the thermal prestress modeling. To consider more realistic spatial temperature variations across the bridge model, 22 parameters ($T_1 - T_{22}$) for temperature distributions are defined along the longitudinal direction of the bridge. Figure 2.5 shows the topological locations of the parameters $T_1 - T_{22}$. It is assumed that temperatures of the structural components that are assigned to the same parameter are identical.

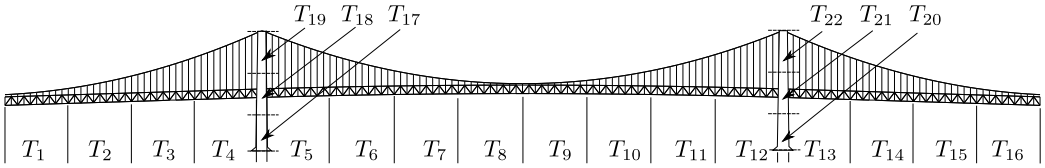

Figure 5.1: Locations of 22 parameters for temperatures of the structural components ($T_1 - T_{22}$).

The objective of the random generation of temperature fields is to obtain a physically-meaningful gradient across the bridge model. In other words, some temperature parameters T can have higher values than the others or they can have similar values. At the same time, it is desired to have some correlations between adjacent temperature parameters. First, it is assumed that a random temperature field $T_1 - T_{22}$ follows $\mathcal{N}(\mu_T, \Sigma_T)$, where $\mathcal{N}$ denotes a multivariate Gaussian distribution; $\mu_T \in \mathbb{R}^{n_T}$ is a vector containing mean values; $\Sigma_T \in \mathbb{R}^{n_T \times n_T}$ is the covariance matrix; and n_T is the number of the randomly generated temperature fields (here, $n_T = 22$). In each realization, the mean values μ_T is randomly generated. First, μ_{T_8}, which is the mean value corresponding to T_8, is drawn by the uniform distribution ranging between 0 and 40°C. Then, μ_{T_1} and $\mu_{T_{16}}$ are drawn by the Gaussian distribution whose mean is μ_{T_8} and standard deviation is 4°C, which are the mean values for the both ends of the bridge. Based on randomly drawn μ_{T_1}, μ_{T_8}, and $\mu_{T_{16}}$, μ_{T_i} $(i = 2, \ldots, 7, 9, \ldots, 15, 17, \ldots, 22)$ is interpolated along the longitudinal direction. The diagonal values of Σ_T is set to be 2°C and the off-diagonal values are 0.75°C if the corresponding temperature parameters are adjacent to each other; otherwise it becomes zero. The off-diagonal values of the covariance matrix Σ_T are determined to consider the correlation between temperatures of structural components that are within close proximity. As an example, T_{18} is correlated with T_4, T_5, T_{17}, and T_{19}.

10,000 realizations of temperature distributions over the bridge model are gener-

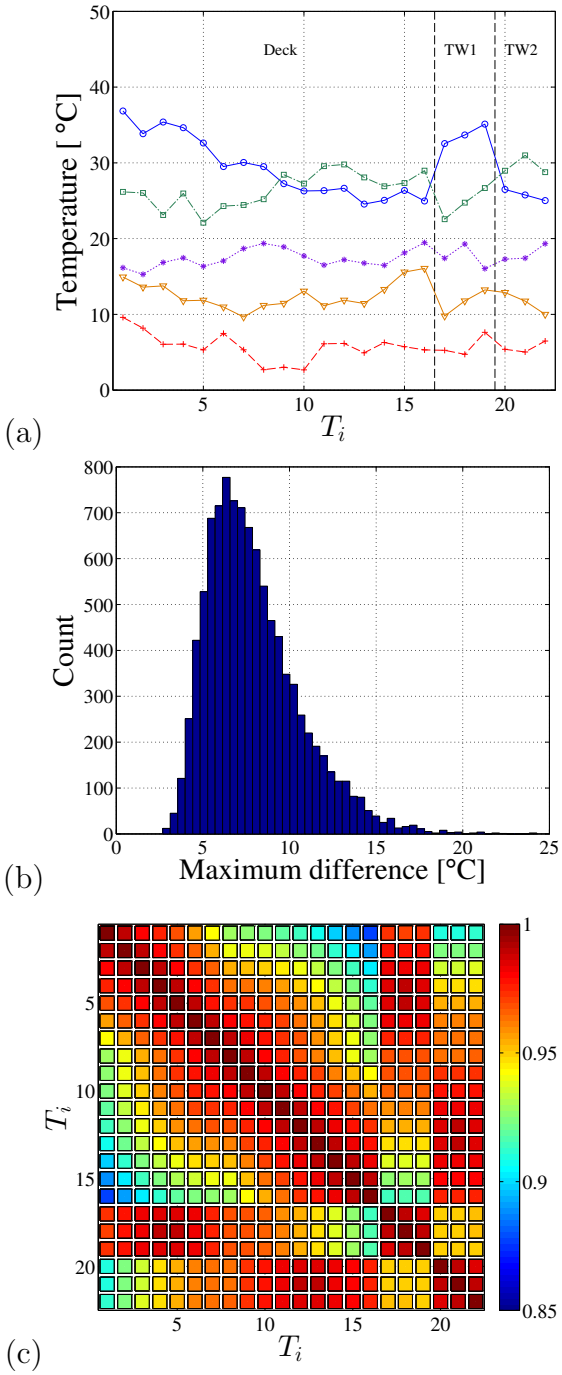

Figure 5.2: Realization of temperature fields: (a) five realizations of the temperature field T_i; (b) histogram of the maximum differences in the realization; and (c) correlation matrix of the generated temperature fields.

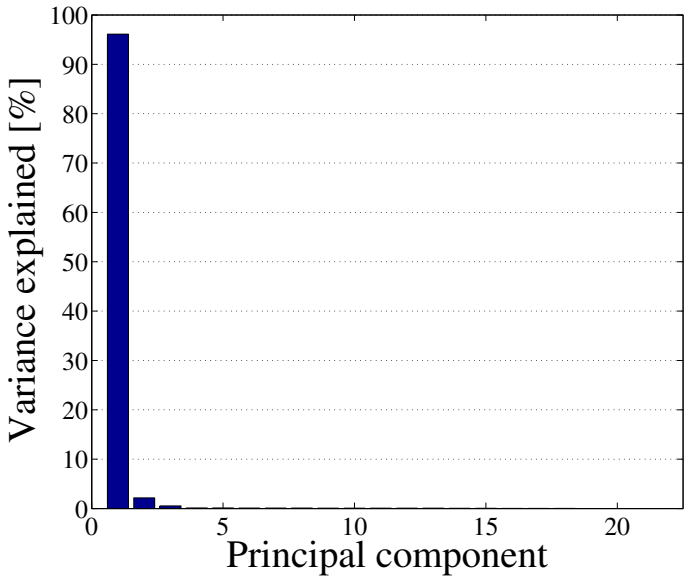

Figure 5.3: Variance of the temperature fields explained by principal components.

ated based on the suggested method mentioned in the previous paragraph. Fig 5.2a shows five examples of the randomly-generated temperature distributions T_i. The various patterns of the temperature variations across the bridge are successfully generated. Fig 5.2b shows the histogram of the maximum difference in each realization. The correlation matrix of the generated temperature distributions is shown in Fig 5.2c. It can be seen that each temperature parameter on the deck is highly correlated with nearby counterparts. The correlations between temperature parameters gradually decrease as the distance between the corresponding structural components increases. The temperatures of the towers are more correlated with the near-neighboring deck components. For example, the temperatures of the one side of the tower $(T_{17} - T_{19})$ exhibit more correlation with the temperatures of the deck components within close proximity $(T_1 - T_8)$ then the other side of the deck.

Principal component analysis (PCA) has been applied to further understand the patterns of the variances in the generated temperature distributions. It transforms an

original set of variables into a set of uncorrelated variables with respect to the orthogonal bases, which are known as principal components. The first principal component accounts for the largest variance of data. The second largest variance is explained by the second principal component, and so on. The amount of variance explained by the i^{th} principal component is estimated by the i^{th} eigenvalue of the covariance matrix of data divided by the total sum of all eigenvalues. For the PCA of the randomly generated temperature distributions, all variables are scaled to have a mean of zero and a standard deviation of one. Fig. 5.3 shows a percentage of variance explained by each principal component. The first and second principal components explain 96.11% and 2.18% of the overall variability of the generated temperature distributions. This is quite similar to what is observed in a study with measured temperature data conducted by Hua et al. (2007), where the first and second principal components explain 94.7% and 4.4% of the variance of measured temperature data of the Ting Kau Bridge, respectively. This indicates that temperature distributions generated by the suggested method have a similar pattern of the variability with real measured data.

The natural frequencies that are affected by various temperatures distributions are calculated by the FE model. All of the structural components that correspond to the same temperature parameter T_i are assumed to have the same temperatures. The temperature changes ΔT are calculated based on the temperature parameters T and the reference temperatures T_{ref}, which are further used for the calculation of prestress distributions for all structural components. It is worth noting that structural components located in the same region can have different prestresses if they have different Young's moduli. The prestress fields of the FE model are calculated with respect to the generated temperature distributions and defined as initial conditions. Then, the natural frequencies corresponding to each realization of the temperature

distributions are evaluated by taking prestress fields into account. In this work, the natural frequencies of the first seven dynamic modes are considered to study the temperature effects.

5.4 Regression analysis

Regression analyses were conducted for two cases: one where no noise was added to the input parameters and output targets and the other where 1% noise was added to the output targets. The input parameters and output targets were linearly scaled to range between -1 and 1. For the cross validation purpose, the data sets were randomly divided into training data and validation data sets, which were 70% and 30% of the whole data, respectively. The training data set was only used for training purposes. The validation data set was used to evaluate the generalization performance of a trained model, which means a trained model should have the same performance for unseen data (validation data). If a trained model was overfitted to training data, it may produce poor prediction for validation data. Linear regression, Random Forest, SVM, and neural network were applied to the input parameters and output targets with no noise and 1% noise to provide comprehensive comparisons between linear and machine learning models for the regression problem considered here.

5.4.1 Learning model: random forest, neural network, and SVM

The random forest technique (Breiman, 2001), an ensemble machine learning method, consists of multiple regression trees. Although this technique requires much less computational cost in the training of a model, data preprocessing, and tunning model

parameters, it is known to have a robust prediction and generalization performance. However, this technique has not been used to model the relationship between temperatures and natural frequencies. Therefore, random forest is considered in the modeling of temperature effects and compared with two popular machine learning methods in this study. A prediction by the random forest technique is determined by taking the average of the predictions from multiple trees. The training of each individual tree is conducted based on the subset of the training data, which is randomly selected with replacement, and a different subset of input parameters. In this application, 70% of the training data were randomly selected and eight input parameters were used for the training of each individual regression tree. The random forests here included 50 trees.

Feedforward neural networks here consist of input, hidden, and output layers. Sigmoid and linear functions are transfer functions for the hidden layer and output layer, respectively. The Bayesian regularization technique, which can produce a smoother fit to the training data and therefore improves the generation performance, is used for the training of the neural networks. One hidden layer, which has fourteen and one nodes for the no noise and 1% noise output target cases, respectively, is located between the input layer (22 nodes) and the output layer (7 nodes). The Akaike information criterion (AIC) (Akaike, 1974) based on the variation data is used to determine the optimal structure of the neural networks.

The SVM (Cortes & Vapnik, 1995) method, where a loss function is adopted to improve generalization performance, is also implemented in this study. It uses the kernel methods that transform data into a higher-dimensional feature space to deal with a nonlinear regression problem. An ε-insensitive loss function and radial-based kernel function were used. Three hyperparameters (the penalty factor C, kernel parameter γ, and margin of tolerance ε) were optimally selected by grid search based

on prediction performances estimated by cross validation.

5.4.2 Result of regression analysis

A linear regression model and the three learning models were trained based on the training data set with no noise and 1% noise output targets. The performance of the four models was evaluated based on root mean square (RMS) errors between the predictions of the models and output target values using the validation data set. The second column of Table 2 accounts for the case where there is no noise in the output targets. In this case, the neural networks and SVM model perform relatively better than the others. The third and fourth columns of Table 2 summarize the performances of the models that are trained with respect to 1% noise output targets. The RMS errors shown in the third and fourth columns are calculated versus 1% noise and no noise output targets, respectively. The RMS errors in the fourth column demonstrate the generalization performance of the four models. Since the RMS errors versus no noise targets (the 4th column) are lower than those versus 1% noise targets (the 3rd column), all of the trained models do not overfit the training data set, which means overfitting of the noise is prevented. Although the prediction capabilities of the four models with 1% noise output targets are similar, the fourth column indicates that the linear and neural network models have a better generalization performance. This can be because there may be no significant nonlinearity between temperature and the natural frequencies based on the simulated data under consideration here. Moreover, the mean of the generated temperature distributions was also investigated as an input parameter for the modeling of temperature effects on natural frequencies with similar results; this also indicates that the relationship between the mean temperature and natural frequencies is fairly linear in this study. The reason that the neural network

model produces a slightly better performance compared to the other machine learning methods can be that the neural network (one node for the hidden layer) is relatively simpler, which also indicates that the level of nonlinearity in the relationship is not that significant.

Part II

Road Surface Monitoring

Chapter 6

Framework of Road Surface Monitoring to Detect Pavement Distress via Multiple Vehicles

In road surface condition monitoring, the current automated pavement distress data collections system provides a reliable resources for road condition management systems. However, the current data collection practice is conducted periodically due to its high cost. There is a practical need to monitor road surface conditions continuously since some pavement distresses such as potholes develop quickly. This chapter presents an innovative data collection framework, which leverages the vibration measurements of multiple vehicles and GPS positioning data.

6.1 Introduction

Smart Growth America and Taxpayers for Common Sense (2014) reported that $16.5 billion was annually spent on repairing the road network from 2009 to 2011 in the

United States. Despite the efforts to provide reliable and safer mobility for motorists, there is still a need to improve the maintenance of road surface conditions. As an example, 37 percent of New York's major roads and highways were rated to being in poor condition (TRIP, 2015). Roads rated in poor condition may include pavement surface distress such as cracks, raveling, shoving, and potholes, which can occur due to material properties of pavement, weather conditions, the amount of traffic, and/or road construction conditions. Especially for a pothole, the four main causes are insufficient thickness of roads, poor drainage system, failures at utility trenches and casting, and miscellaneous paving defects and cracks (Eaton, 1989).

Deteriorated roads also result in New York motorists spending $6.3 bilion annually on extra vehicle operating costs (VOC), which include accelerated vehicle depreciation, additional repair costs, increased fuel consumption, and tire wear (TRIP, 2015). For New York City, this amount is equivalent to $694 per motorists. Defective roads can also cause serious accidents for drivers and pedestrians. Moreover, claims are made against municipalities due to accidents and/on property damage caused by defective roads. As an example, 12,286 property damage defective roadway claims were submitted to New York City between Fiscal Years 2010 and 2015 and 1,549 claims were settled at a cost of nearly $1.5 million (Stringer, 2015). 552 claims were submitted to Cleveland, Ohio in 2013 for the vehicle accidents due to street defects. The city paid $28,760 for the accepted 101 claims out of 552 (Atassi, 2014).

The current state-of-the-art technology uses data collection vehicles equipped with various sensors to automate the data acquisition process and to acquire data in an operating condition. A review of automated pavement distress collection techniques is carried out by McGhee (2004). Profilers, which are instrumented with a laser, acoustic, or infrared sensors, are used to measure profiles of road surfaces. Then, measured profiles are used to determine the International Roughness Index (IRI), a

widely-used and standard pavement condition metric for serviceability (ride-quality). For the maintenance of pavement surface distress, imaging technologies such as area scanning, line scanning, and 3-D laser imaging are used for the distress recording. 3-D laser-sensing imaging sensors are used to map cracking, rutting, shoving, and potholes (Bursanescu, Bursanescu, Hamdi, Lardigue, & Paiement, 2001; Chang, Chang, & Liu, 2005; Li et al., 2010). The images collected by the line scan camera are automatically processed to detect cracks (Gavilán et al., 2011). Area scanning and line scanning cameras are used to reconstruct 3D surfaces via sterovision (Hou, Wang, & Gong, 2007). Pavement video data are used for the automated pothole detection (Koch & Brilakis, 2011; Koch, Jog, & Brilakis, 2012). Data collection vehicles equipped with downward, forward, side, and/or rear-facing cameras collect video; this forms a continuous record of pavement surfaces and is used as part of the distress rating process (Pierce, McGovern, & Zimmerman, 2013).

The current state-of-the-art data collection practice using imaging technologies is able to detect all pavement surface distress such as faulting, rutting, and cracking, providing a reliable data source for the standard rating system used in the road surface maintenance. However, the evaluation of pavement distress by the current automated data collection method is in general conducted periodically due to its high cost. For example, The combined costs of imaging and sensor data range from $24 to $85 per mile (McGhee, 2004). Some pavement distress such as cracking and rutting, in general, develop slowly. Therefore, the current data collection practice which can identify all types of pavement distress can be conducted periodically based on the aging of road surfaces. However, there are street defects which develop more quickly, which might need a more frequent and/or continuous data acquisition approach.

To meet the need to collect data for quickly developing street defects in real-time or near real-time, vibration-based approaches have been suggested (De Zoysa,

Table 6.1: Comparison between the vibration-based and image-based approaches.

	Vibration-based approach	Image (video)-based approach
Size of data	Small	Big
Coverage Area along a lane	Limited to wheel path	Full coverage
Detectable pavement distress	Limited to ones that cause vibrations to vehicles	Most pavement distresses
Computational cost (Storage and processor)	Low	High
Amount of data to produce a reliable data source	Multiple measurement	One-time measurement
Post-processing	Online or near real-time	Usually Batch mode
Data update	Continuous	Periodic

Keppitiyagama, Seneviratne, & Shihan, 2007; Yu & Yu, 2006; Eriksson et al., 2008) to be complementary to the current state-of-the-art data collection practice. Table 6.1 compares the advantages and limitations of the vibration-based and image-based approaches. Although a coverage area of the vibration-based approach is limited to the wheel path of vehicles since tires must hit street defects to capture vibration responses, its main advantage is the small size of the recorded data. The small size of acceleration data permits one to reduce the storage requirements for data logging. Importantly, it also reduces computational expense for data processing, which makes real-time data processing possible. The vibrations of vehicles can be influenced not only by road surface conditions, but also by the dynamic system of the vehicles themselves such as the suspension system, total mass, and vehicle speed. Therefore, a one-time measurement might not be enough to provide a reliable result. A large amount of data is needed to be collected and integrated to improve the reliability of a vibration-based approach. Recently, the potential of vibration-based approaches using connected vehicles have been rigorously investigated. Eriksson et al. (2008) collected data from taxis via a delay tolerant network. The potholes were detected by integrating the results from the patrol vehicles based on locations. Vibration data

collected from the smartphones mounted on vehicles were used to predict a three and a five level gradation of road roughness as defined by the IRI scale (Belzowski & Ekstrom, 2015). The acceleration and suspension deflection data measured from fleet vehicles with aftermarket accelerometers were used to estimate the IRI and to detect potholes (Mixon, Garrett, & Krueger, 2012).

In this study, a framework of the data acquisition and data integration for the vibration-based road surface monitoring is suggested to detect isolated street defects and rough road conditions, which leverages a low-cost sensor and connected vehicle. A mobile data collection kit (also called a vehicle client), which can be simply mounted on any vehicle, has been developed to collect vibration and GPS positioning data. Also, the local data logging algorithm is developed to improve the data storage efficiency in each vehicle client by logging only the data which contain useful information on road surface conditions. Once Internet connection is available, each vehicle client uploads the collected data to a back-end server, where a more precise street defect classification algorithm and a trajectory clustering algorithm are located. The trajectory clustering algorithm is suggested to integrate data from vehicle clients not only based on location, but also based on direction. Data sets that are grouped by the trajectory clustering algorithm can be practically valuable since they can be used to improve a street defect classifier once the corresponding ground truth data become available. The developed system and algorithms are tested on real roads.

In this chapter, the overview of the proposed road surface monitoring system is presented in the next section, followed by the details of the data logging algorithm in each vehicle client. Then, the street defect detection algorithm running at the back-end server is demonstrated. At the end, conclusions are made.

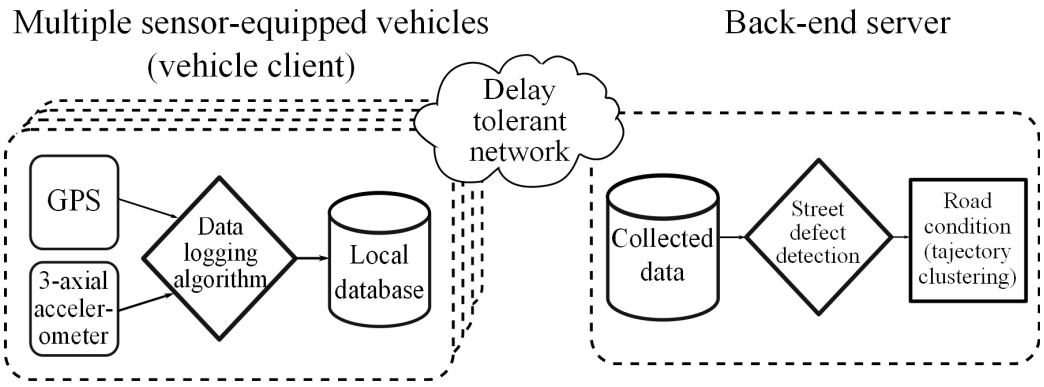

Figure 6.1: Architecture of the proposed road surface monitoring system.

6.2 Road Surface Monitoring System

The architecture of the proposed road surface monitoring system with multiple sensor-equipped vehicles is illustrated in Figure 6.1. It consists of two parts: a vehicle client and a back-end server. In each vehicle client, a triaxial accelerometer, GPS sensor, micro computer, and local storage are included. Since a vehicle client may not have continuous Internet connection, collected data are first cached on local storage by a data logging algorithm embedded in a micro computer. When Internet connection is available, data logged in local storage are transmitted to a back-end server, where data from multiple vehicle clients are combined to identify road surface conditions based on a street defect detection and a trajectory clustering algorithm.

6.2.1 Sensor package with micro computer

In each vehicle client, a triaxial accelerometer and GPS sensor are equipped to collect data. The accelerometer measures the acceleration responses of a vehicle due to road conditions in three spatial directions with a sampling frequency of 125 Hz. The maximum acceleration measurement is ± 8 g. Acceleration measurement resolution

is 976.7 ug. Acceleration white noise standard deviation is 2.8 mg. The driving direction, sideways, and vertical direction are denoted as x, y, and z-axes, respectively. The acceleration responses in the y and z directions are more significantly affected by street defects, therefore they are used for the road surface monitoring here. Those in the x direction are excluded because the accelerations of a vehicle itself have a dominant effect on that direction. The GPS device records time, positioning data, and the speed of the vehicle with a sampling frequency of 10 Hz. The GPS positioning errors are mostly less than three meters. A more detailed description of the positioning errors is provided later. The GPS positioning data enable the localization of street defects. The recorded time provides the information of when the defects are found. Knowing the speed of a vehicle is also important since higher vehicle speeds can cause higher peak values in acceleration responses. Each vehicle client also includes a microcomputer with memory, CPU, local storage, and wireless connectivity. The computational resources are used in the preliminary process of the collected data, which runs in an online fashion. Local data storage spaces are used to cache data until they are transmitted to a back-end server. Wireless connectivity permits the local computer to communicate not only with a back-end server, but also with a smart phone and tablet computer.

6.3 Data Logging Algorithm in Vehicle Clients

Collected data should be cached on local data storage until Internet connection becomes available. However, local data storage space in vehicle clients is limited. This requires the development of an efficient data logging algorithm to manage local storage. When local storage space becomes full, a vehicle client will fail to cache new data until logged data are transmitted into a back-end server. In fact, logging all of the

measured data into local storage cannot be very efficient because only some of collected data contain meaningful information for the detection of street defects. As an example, data that are recorded from smooth road conditions do not have significant excitations in measured signals and are not very useful for detecting street defects. The logging of those data should be minimized to efficiently use local storage.

A *data logging algorithm* was designed that runs on each vehicle client to increase the efficiency of the data logging to local storage. It is an online algorithm, which means that it processes an incoming data point piece-by-piece in a serial fashion. The purpose of the algorithm is to minimize the amount of unnecessary data logging by each vehicle client. There are two main considerations in developing the local algorithm. The first is that it is computationally light since the computational resources of the micro computer are somewhat limited. The second is that the data recorded when passing over street defects must be logged, i.e., only the data collected from smooth roads should be filtered out.

6.3.1 Signal processing of measured data

First, the acceleration data are preprocessed in the microcomputer in order to correct the mean-shifting caused by vehicle movements. The vibration responses that are measured from the sensor-equipped vehicle are not only due to the roughness of road surfaces and street defects, but also due to the movement of the vehicle itself. Since the accelerometer used here measures down to 0 Hz, i.e., can measure constant gravitational accelerations, it is sensitive to the orientation of the axes and gravitational forces. When a vehicle makes a sudden turn or lane change, an inertia force is placed on the accelerometer and produces a mean-shifting in the responses. Driving up or down hills also slightly changes the orientation of the sensor, which accounts

for the slow shifting of the mean values of the recorded accelerations. Those acceleration responses caused by vehicle movements themselves have lower-frequency signals, compared to the responses due to the conditions of road surfaces.

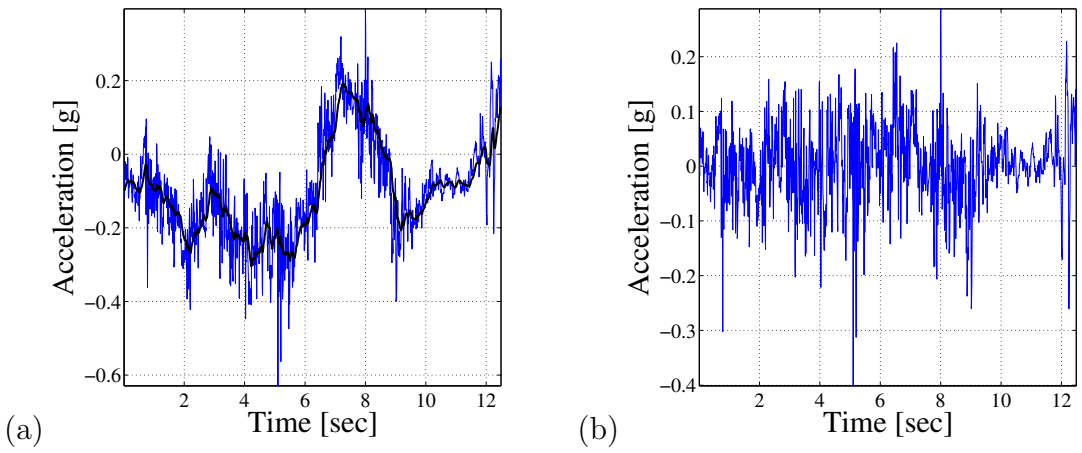

Figure 6.2: Means shifting correction by removing EMA values: (a) acceleration responses in the y direction with the EMA values; and (b) EMA removed acceleration responses in the y direction.

It is important to separate the vibration signals due to the vehicle movements from ones due to road surface conditions. The exponential moving average (EMA) values are calculated and taken out from the original signals. This signal processing performs in an online fashion, which means that a incoming data points are processed piece-by-piece. The EMA values are related to lower-frequency vibration signals, which account for the slow mean-shifting due to the vehicle movement. Removing the EMA values from the acceleration data is equivalent to removing the vibration signal due to the vehicle movement. Although many high-pass filters such as the Butterworth and Chebyshev are available to remove the lower-frequency vibration, the removal of the EMA values is used here to minimize computational expense on a vehicle client since the computational resources of a microcomputer are not as powerful as a regular laptop or computer. In Figure 6.2a, the recorded acceleration data in the y direction

are shown with the EMA values (the black line), which account for the low frequency responses due to the movement of vehicles. By taking out the EMA values, the responses due to the vehicle movements are extracted. The high-passed acceleration data is shown in Figure 6.2b.

6.3.2 Data Logging Mechanism Based on the Level of Vibrations

Since street defects generally produce more vibrations of vehicles, compared to smooth road surfaces, the level of vibrations measured in a specified duration is used for the minimization of data logged from smooth road surfaces. In other words, when the sensor-equipped vehicle vibrates above a certain threshold level, all of the incoming data points are logged to local storage. When the vibrations of a vehicle are less than the threshold level, only some of the incoming data are cached in order to efficiently manage local storage space. The data logging mechanism improves the efficiency of the local data logging. The root mean square (RMS) values are used to calculate the level of vibrations in a specified time window. It is defined as follows:

$$x_{rms} = \sqrt{\frac{1}{n}\left(x_1^2 + x_2^2 + \cdots + x_n^2\right)}, \tag{6.1}$$

where n is the number of points used for the calculation of the RMS value. n is 100 here, which is equivalent to 0.8 seconds. It is noteworthy that the current RMS values are calculated from the previous 0.8 second acceleration data. The RMS values in the y and z directions, which are respectively denoted as RMS_y and RMS_z, are calculated from the acceleration responses whose EMA values are removed.

The data logging algorithm depends on the triggering condition, which is defined

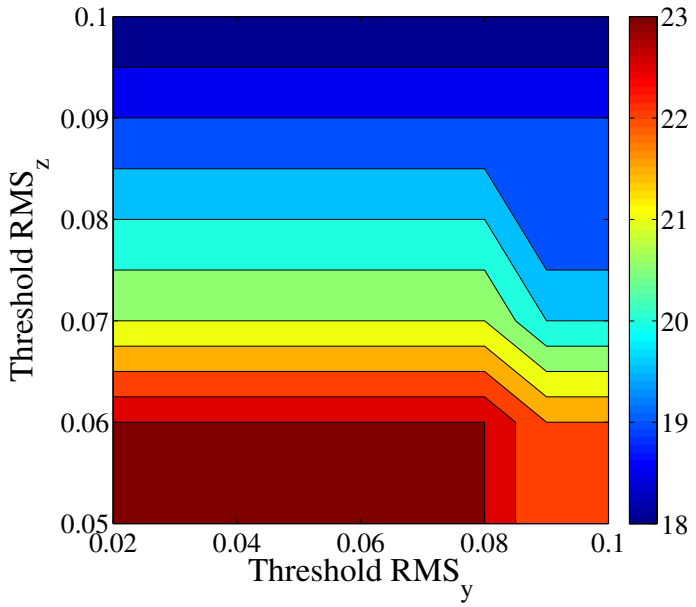

Figure 6.3: Determination of the thresholds based on the preselected actual 23 street defects.

as follows:

$$\text{Triggering condition: } RMS_y \geq 0.08\ g \textit{ and } RMS_z \geq 0.06\ g. \tag{6.2}$$

The triggering condition is based on two thresholds for RMS_y and RMS_z. They are determined based on a priori knowledge of actual road surface conditions. One of the considerations for the local data logging algorithm is that data sets that may contain useful information for the detection of street defects should be logged, i.e., the development of the local algorithm is more focused on minimizing missing data (a type II error). To select thresholds in a conservative way, 23 actual street defects were carefully selected including both severe and moderate ones. Then, data while passing over these street defects were collected. The thresholds for RMS_y and RMS_z versus the number of the data sets that are above the corresponding thresholds are shown in Figure 6.3. When the triggering condition defined in Eq. 6.2 is applied, all

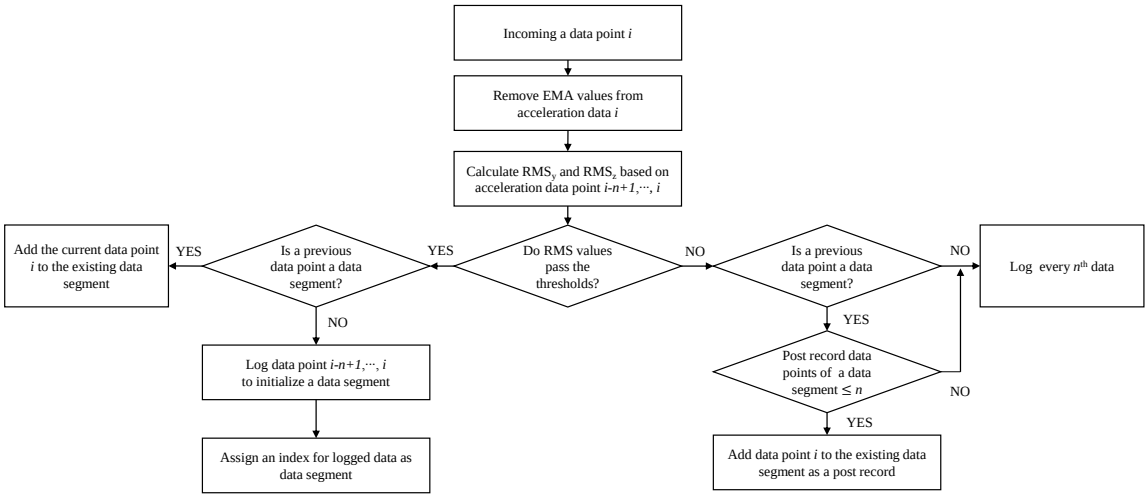

Figure 6.4: Flowchart of the local data logging algorithm.

of the 23 prespecified defects are logged. As the thresholds increase from 0.08 g and 0.06 g for RMS_y and RMS_z, respectively, the local data logging algorithm starts to miss the data logging of the 23 defects. Exceedances of these thresholds correspond to vibrations which are perceptible to the vehicle driver. Since the thresholds are conservatively determined, some data over smooth road surfaces can have RMS values which are slightly above the thresholds and satisfy the triggering condition, which is known as a type I error. This phenomenon can be influenced by the noise level in the acceleration data. In the next section, a trained classifier is applied to deal with the type I error, which is the case of data that are logged over smooth road surfaces, but satisfy the triggering condition.

The flowchart of the local data logging algorithm is shown in FIG 6.4. The data types logged into the local database are preprocessed acceleration responses, GPS positioning data, and the speed of vehicles. The data logging to local storage starts from the 100 data points prior to the data point where the RMS_y and RMS_z began to satisfy the triggering condition. It is important to save those data points because they

are used for the calculation of the RMS values that are above the thresholds. Then, incoming data are recorded while the RMS values remain above the thresholds. Once the RMS values drop below the thresholds, the additional 100 data points from the last data point that satisfies the triggering condition are also recorded. The additional data points have RMS values which are less than the thresholds and account for the vibration responses recorded from the smooth road conditions just after passing possible street defects. The comparison between the additional data points and the data points whose RMS values are above the thresholds permits one to evaluate how much energy is generated due to street defects. After finishing the logging of the additional data points, the data set that is initiated by the triggering condition is defined as a *data segment*. However, the RMS values can exceed the thresholds again while recording the additional 100 data points. In this case, data are continuously recorded until another additional 100 data points whose RMS values are below the thresholds are logged. The extension of the local data logging happens when there are consecutive street defects on roads. It means that one data segment can contain multiple street defect records. In Figure 6.5, one of the logged data segments is shown. This *data segment* does not have the extension of the data logging. At the 0.8 seconds, the RMS_y and RMS_z values start to go above the thresholds. In the region between the 0.8 and 1.5 seconds, the RMS_y and RMS_z values are bigger than the thresholds. After the 1.5 seconds, the RMS_y and RMS_z values fall below the thresholds. These last additional data points from 1.5 seconds to the end stop the logging process for this one *data segment*.

When vehicles travel on smooth roads, there are in general no significant excitations of vehicles and the RMS values are usually less than the thresholds. It is not necessary to log all of the data whose RMS values are below the thresholds into local storage. However, due to the need for tracking of the roads that have been covered

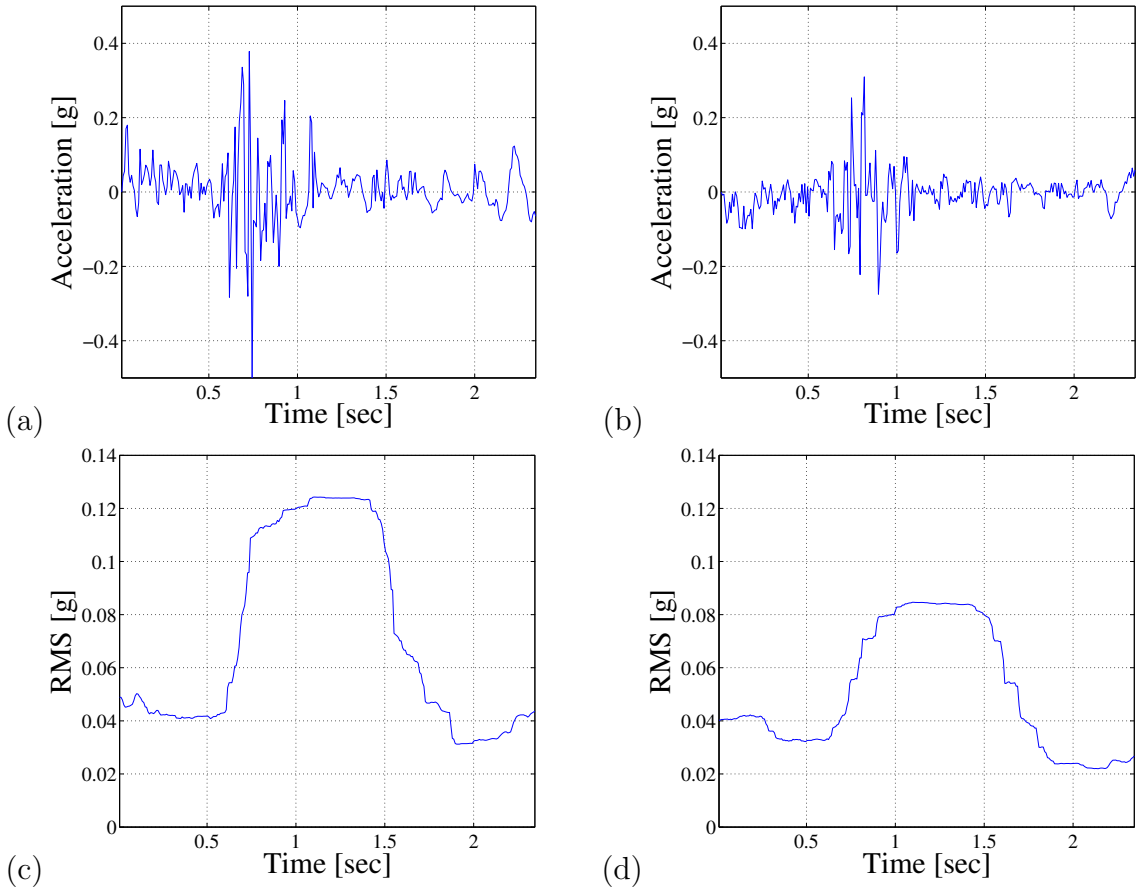

Figure 6.5: Example of a logged data segment: (a) acceleration in the y direction; (b) acceleration in the z direction; (c) RMS_y; and (d) RMS_z.

by the sensor-equipped vehicles, the data that do not satisfy the triggering conditions are logged only once every 0.8 seconds and defined as a *smooth data*. In Figure 6.6, the red lines represent the *data segments* that are logged based on the data logging mechanism which is explained in the previous paragraph. The blue dots are the *smooth data*. 6906 and 170 data points for the red and blue dots, respectably, are logged to cover the path shown in Figure 6.6 using the local data logging algorithm. Without the local data logging algorithm, 28,156 data points would be required to cover the path. In this case, the data reduction ratio due to the local data logging algorithm is 75%. The data reduction ratio is also subjected to road surface conditions. In other words, roads that have more smooth surfaces correspond to a higher filtered-out ratio. The suggested data logging method is very efficient in reducing the amount of logged data in the local database. It performs preliminary evaluation of road conditions based on the predetermined thresholds, which partitions the recorded data into *data segments* or *smooth data*.

6.4 Street Defect Classifier at Back-end Server

The *data segments* from multiple sensor-equipped vehicles are gathered at a back-end server. A street defect algorithm is applied to each *data segment* in order to classify them into the different types of street defects.

6.4.1 Division of logged data into smaller fragments

As mentioned in the previous section, each *data segment* can capture more than one street-defect response. It is necessary to divide *data segments* into smaller pieces with respect to the number of the defects, which are defined as *data fragments*. The division of a *data segment* is performed based on the number of the dominant peaks of the RMS

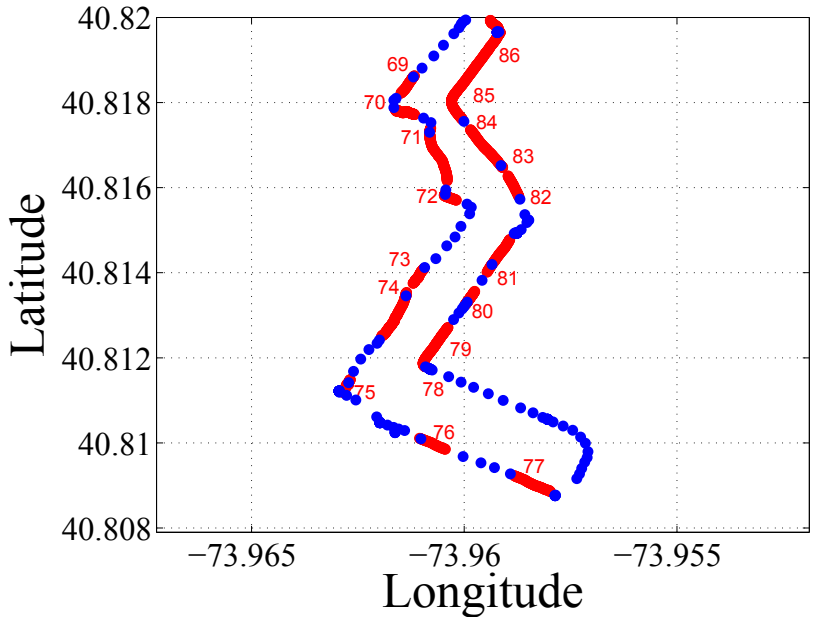

Figure 6.6: GPS locations of the data segments.

values. In Figure 6.7, the measured acceleration responses and the corresponding RMS values in the y and z directions are demonstrated. In this example, the *data segment* is divided into two *data fragments* since two dominant peaks are shown in the RMS values. The first and second *data fragments* are represented as red and black lines, respectively. The last part of the *data segment* (the blue line) has RMS values which are less than the predetermined thresholds. It accounts for the additional 100 data points that stop the record of the *data segment*, which is defined as a *smooth data fragment*. The *smooth data fragment* provides information on the responses just after passing over street defects. The *smooth data fragment* is compared with the *data fragments* belonging to the same *data segment*. In the *data segment* shown in Figure 6.7 the *smooth data fragment* is compared with the *data fragment* 1 and 2 to know how the acceleration responses are affected by two possible consecutive street defects.

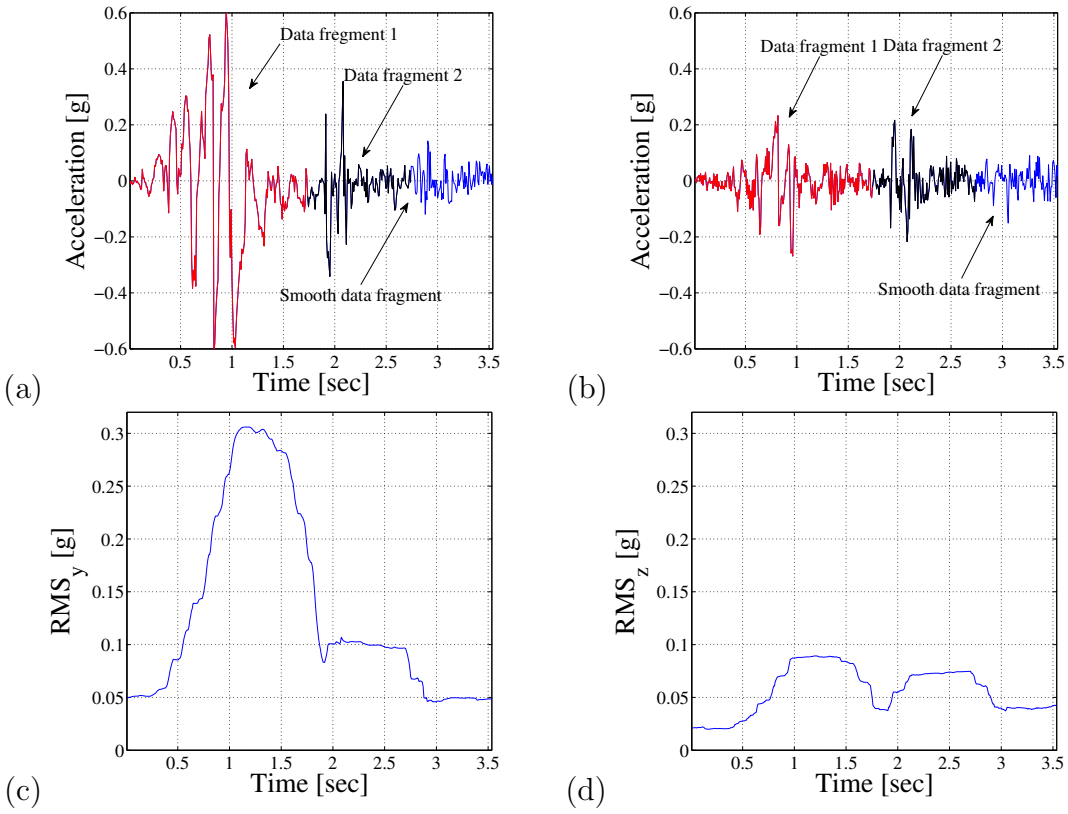

Figure 6.7: Fragmentation of the logged *data segment*: (a) acceleration responses in the y direction; (b) acceleration responses in the z direction; (c) RMS values in the y direction; and (d) RMS values in the z direction.

6.4.2 Output categories of a classifier

At the back-end server, a supervised machine learning technique is applied to classify collected *data fragments* into three different categories (impulse, rough, and smooth classes). These three categories are determined based on the dynamic characteristic of vehicle responses over street defects, not based on a street defect type and/or severity. While looking at the dynamic responses of the collected *data fragments*, the three categories are distinct and therefore used as the output classes of a classifier. Dennis, Hong, Wallace, Tansil, and Smith (2014) mentioned that detecting acute distress events (e.g., potholes) and rough ride events could potentially be obtained with existing technology and infrastructures within 3-5 years. An impulse class accounts for sudden impulse-like vibrations of vehicles. Isolated street defects such as potholes and sunken manholes can be categorized into this class since they produce a jarring experience to vehicles. One example of the acceleration responses classified into the impulse class is shown in Figure 6.8a. A narrow and tall spike, where a certain amplitude is reached during a short period of time, can be observed in the response for the impulse class. Unlike the impulse class, a rough class includes an event where vehicles experience a comparatively continuous vibration, which accounts for a rough ride. The rough ride event can be due to street defects that are not isolated in a small area along the road surface such as defective street cuts, raveling, and shoving. The acceleration responses of the rough class are shown in Figure 6.8b, where the vehicle experiences one-second sustained vibrations. The last one is a smooth class, where no significant vibrations are present in the acceleration responses. As mentioned in the previous section, data over smooth road surfaces might satisfy the triggering condition and be logged as a *data segment*. A smooth class is defined to account for those data. One example of those data segments is shown in Figure 6.8c.

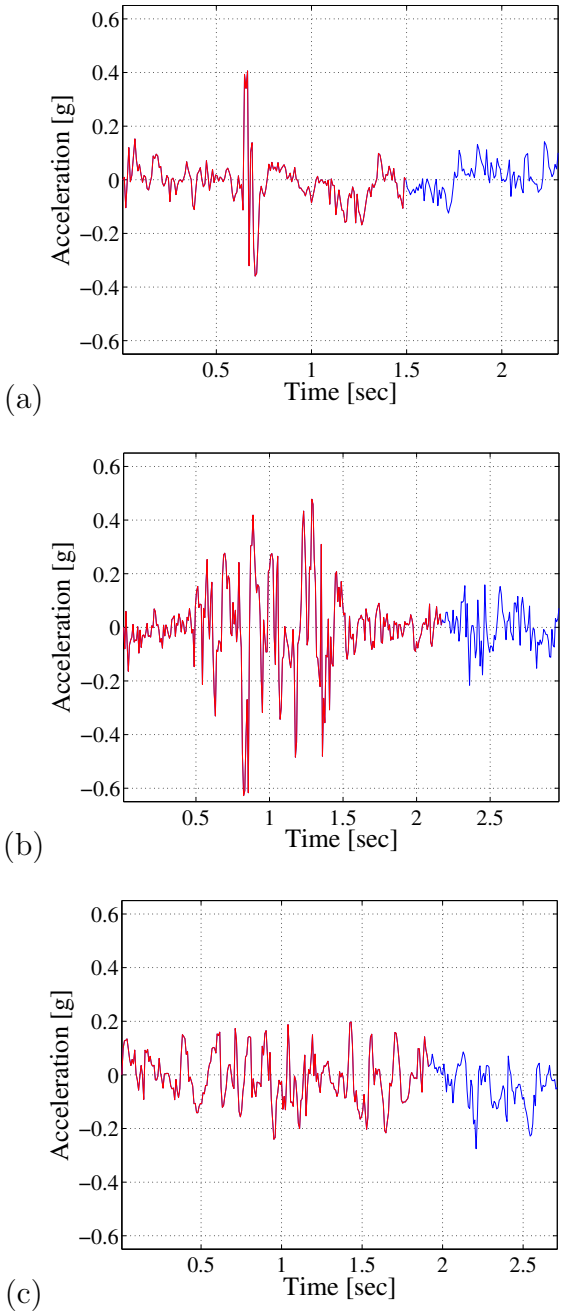

Figure 6.8: Three classes of street defects: (a) impulse class; (b) rough class; and (c) smooth class.

6.4.3 Selection of the input parameters for a supervised machine learning and the manually labeled data for the training of classifiers

The selection of inputs for classification problems is critical to achieving an acceptable result since input parameters are directly related to output classes. A total of 14 inputs are carefully determined for the classification problem under consideration here. The acceleration responses of vehicles are affected not only by road surfaces, but also by the dynamic systems of the vehicles themselves such as the suspension system and total mass. Amador-Jiménez and Matout (2014) show not surprisingly that vehicle sizes have an effect on acceleration responses over the same road surfaces. It is assumed that vehicles that are categorized into the same vehicle type have a relatively similar dynamic system. Since many different types of vehicles such as compact SUVs, mid-size sedans, and buses can be used for the data collection, a vehicle type is chosen as an input. Even when the mobile data collection kits are mounted on the same type of vehicles, they can be placed at the different locations on the vehicle. The acceleration responses of vehicles can be subjected to the transversal and vertical placements with respect to the lane of roads. Eriksson et al. (2008) mentioned that the placement of accelerometers can affect the quality of acceleration signals. Therefore, the mounting location of the mobile data collection kits is also chosen as an input. The two inputs above are categorical inputs. During the real road test, it is also observed that the peaks of the acceleration responses are correlated with the speed of the vehicles. In general, higher vehicle speed produces higher amplitude in the acceleration responses since vehicles traveling at a higher speed have more kinetic energy that produces higher amplitudes over a street defect. The effect of vehicle

speed on acceleration responses is also observed in many studies (Eriksson et al., 2008; Dawkins & Powell, 2011; Mixon et al., 2012; Amador-Jiménez & Matout, 2014; Belzowski & Ekstrom, 2015). As a result, the speed of a vehicle is selected as a numeric input. The length of each data fragment is included to represent the duration of the responses. More inputs are selected from the low-passed acceleration responses of each data fragment. The low-pass filter with a 1 HZ cutoff frequency is applied to remove high-frequency components caused by noise. The maximum absolute values of the acceleration, jerk, RMS, and zero crossing in the y and z direction are also included. The jerk values are the first time derivative of accelerations. The maximum values of accelerations in the y and z directions just after passing street defects (*smooth data fragment* in each *data segment*) are added.

6.4.4 Principal component analysis on numeric input parameters

Each numeric input should have sufficient variability to obtain a reliable classification result. Thus, principal component analysis (PCA) (Jolliffe, 2005) is conducted for the manually labeled data fragments to check whether the selected numeric inputs have reasonable variabilities. Each labeled data fragment consists of 12 numeric inputs, whose high-dimensional data space presents difficulties in visualizing their variances in a lower-dimensional space. PCA is carried out to provide an informative viewpoint with the orthogonal lower-dimensional axises. Since the numeric inputs have different units, they are unit-normalized for the analysis. The numeric inputs are converted into the linearly uncorrelated principal components via an orthogonal transformation. The 421 inputs are shown in Fig. 6.9 with respect to the first two principal components. The blue lines account for the contributions of the inputs

to the two principal components. The maximum values of jerk, acceleration, and RMS have a greater contribution to the first principal component. The maximum accelerations just after passing street defects as well as vehicle speeds are more likely to affect the second principal component, which is orthogonal to the first principal component. The lengths of the blue lines show the amount of variation to the principal components. The maximum jerk and acceleration values have dominant variations to the first principal component. The maximum acceleration values just after passing street defects is the largest coefficient in the second principal components.

A classifier is trained in advance so that it can categorize street defects with respect to the inputs extracted from the collected *data fragments*. For the purpose of training, the 421 *data fragments* with manually-labeled output classes are used. These *data fragments* are collected from the already-known actual street defects, which means a prior knowledge of the input parameters and the output categories is given for the training. 141, 82, and 198 *data fragments* are assigned to the classes of impulse, rough, and smooth, respectively. Based on the inputs and the corresponding output classes of the 421 data fragments, a classifier is trained.

6.4.5 Multilayer neural network for the classification

Multilayer feedforward neural networks (Haykin, 1998) are used to classify the *data fragments* into the three categories of street defects. Figure 6.11 shows the structure of feedforward neural networks. The neural networks consist of the input, hidden, and output layers. The number of nodes for the input and the output layers is 14 and 3, respectively. There are two hidden layers. The first and second hidden layers consist of 10 and 7 nodes, respectively. The sigmoid transfer function (Cybenko, 1989) is used for each node in the hidden layers. The manually labeled *data fragments* are divided

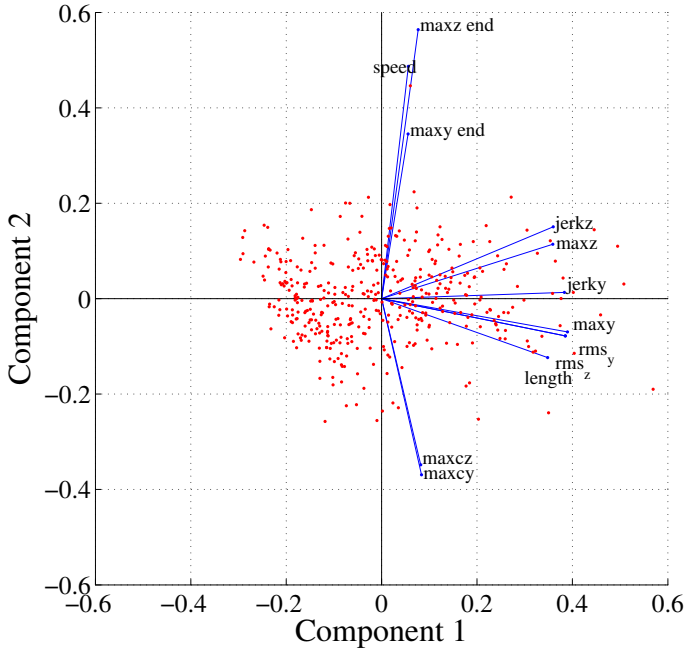

(a)

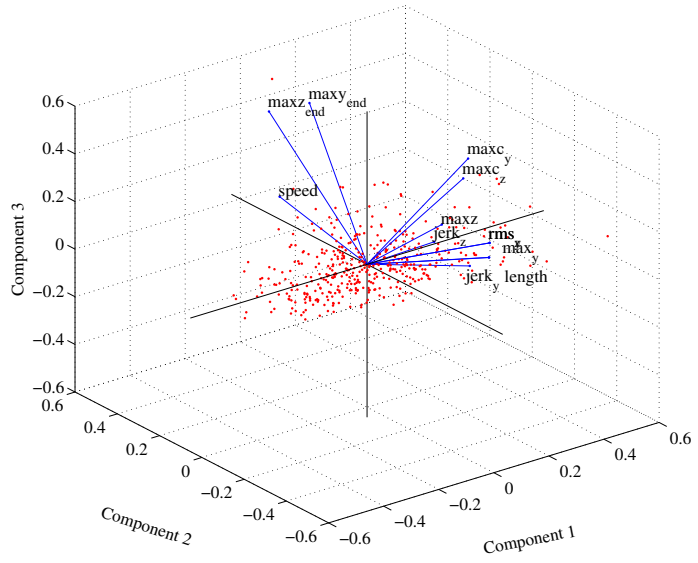

(b)

Figure 6.9: Principal component analysis for manually labeled inputs.

into the training and validation data sets, and represent the 70% and 30% of the entire set of *data fragments*, respectively. The back-propagation algorithm is used for the training of the model. During the training, the adjustable network parameters such as weights and biases are tuned so as to optimize the network performance. The validation confusion matrices for the neural network are shown in Figure 6.10, representing the performance of the trained neural network model. The rows of the matrices are the predicted classes from the trained neural network model. The columns of the matrices represent the actual classes. The prediction accuracy of the trained model is 81.4%, 85.7%, and 87.1% for the impulse, rough, and smooth classes, respectively.

6.4.6 Random forest for the classification

For purposes of comparison, Random forest (Breiman, 2001), which belongs to an ensemble learning method, is also carried out to the classification problem here. Random forest consists of multiple decision trees, which is shown in Figure 6.12. Multiple decision trees are trained based on the subsets of the training data set, which are randomly selected with replacement. This procedure is called as bagging. Because classification results are determined by multiple decision trees, over-fitting to the training data set can be prevented. Another great advantage of random forest is the random selection of input parameters at each splitting of nodes, i.e., a random subset of input parameters becomes a candidates for each splitting of nodes. When determining the subset of input parameters, strong predictors that substantially affect a result of classification are more likely to be selected. The bagging idea of input parameters for each decision tree leads to a better classification result although some inputs are not strong predictors for output classes. In this method, output classes

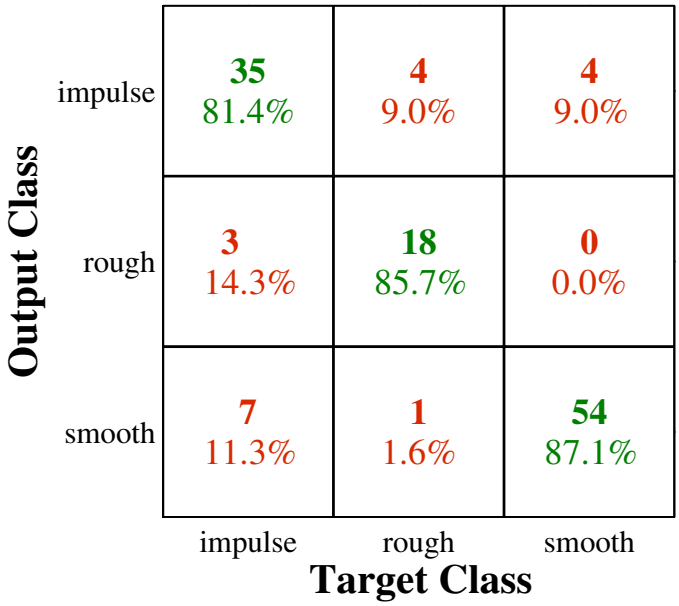

Figure 6.10: Validation confusion matrices of the neural network.

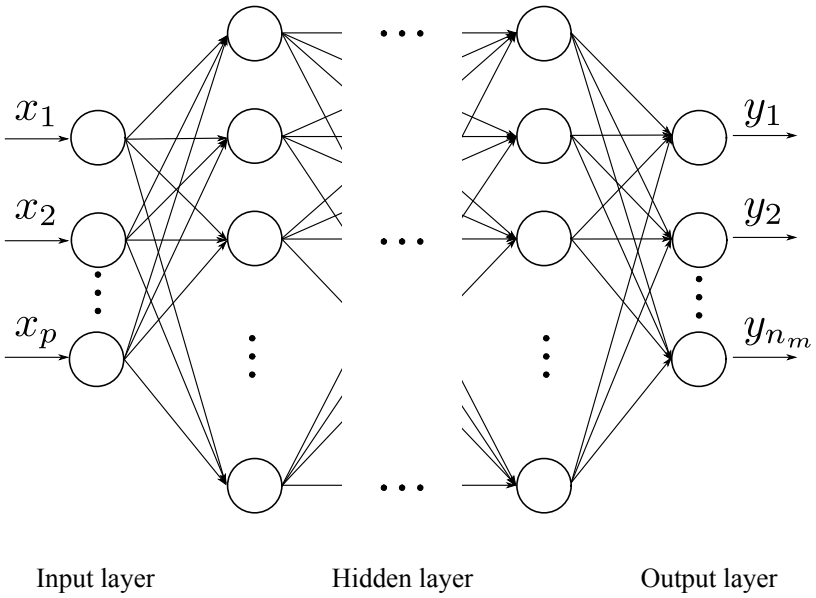

Figure 6.11: Structure of feedforward neural networks.

are determined by taking the majority votes from multiple decision trees.

The same training and validation data sets that are used in the neural network model are used for the random forest model. 50 decision trees are trained with respect to the training data set. The validation confusion matrix associated with the random forest method is shown in Figure 6.13. Compared to the trained neural network model, the predicting accuracies of the random forest are quite similar in the impulse and smooth classes. However, the performance of the neural network is slightly better in predicting the rough class. Furthermore, predictor (variable) importance, which is a measure of the importance of inputs in the decision of output classes, is estimated by the Random forest technique. The estimation of predictor importance shows that the two most significant inputs are the length of data segments and the maximum values of accelerations in the y direction. The speed of vehicles and the zero crossing in the both direction have a relatively lower level of predictor importance, compared to the other inputs. Although the estimation of predictor importance is not rigorously carried out for the trained neural networks since it is not a primary focus of this study, several approaches are available for the neural network to estimate predictor importance (Gavilán et al., 2011). Since the neural network has a slightly better performance than the random forest by comparing their validation confusion matrices, the random forest is not used as a classifier hereafter.

6.4.7 Results of the classification

Three different vehicles collect new data sets to validate the classifiers for street defects. Unlike the training data sets, the output classes of the new data sets are unknown and predicted by the trained neural network. The trained neural network model is applied to categorize the types of street defects. The GPS position data

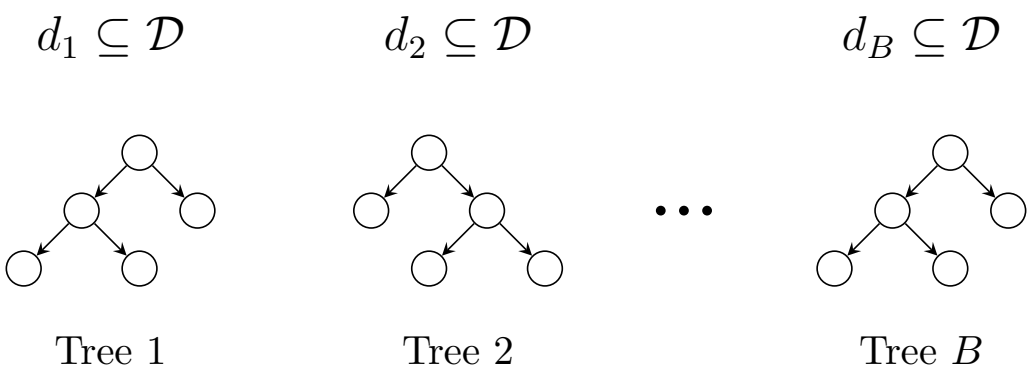

Figure 6.12: Schematic of random forests.

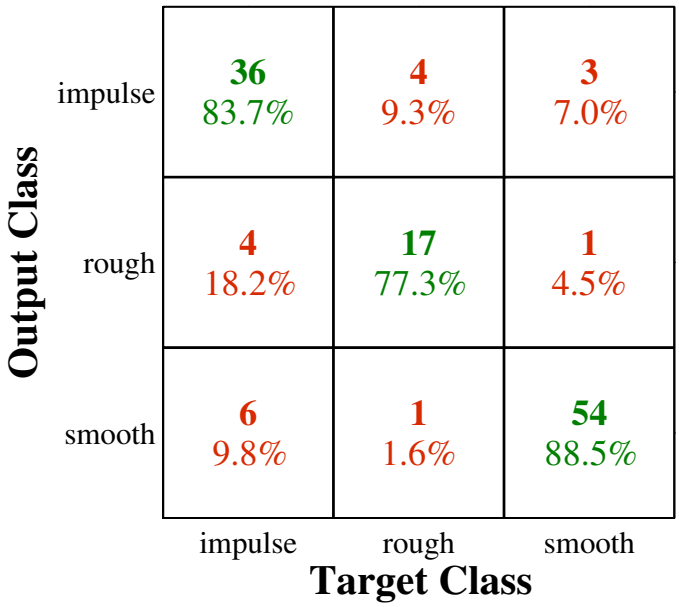

Figure 6.13: Validation confusion matrices of the random forest.

corresponding to the *data fragments* are used for the localization of the classified street defects. The predicted classes are shown in Figure 6.14 with respect to their locations. The red, orange and green lines respectively represent the rough, impulse, and smooth classes predicted from the trained model.

Some driving routes are examined by more than one vehicle. The comparison of the classification results on the route is made in Figure 6.15, where two different vehicles have driven from North to South. Three locations are marked with annotations, which refer to the corresponding ground truth. For these three locations, the two vehicles have traveled on the same lane because there is only one lane in each direction. The initial points of the three locations, which are the Northern parts of the locations, are a quite similar. In the area that is annotated as "Pothole + Rough", there was a pothole and followed by a rough road surface. The vehicle 1 successfully classified them as the impulse and rough classes. Although the rough road was correctly classified by the vehicle 2, the pothole was misclassified as the rough class. The acceleration responses corresponding to these ground truths are shown in Figures 6.16ab. The next validated ground truth is marked as "Manhole + Raveling", where the sunken manhole was located close to the centerline of the road and the raveling was on the shoulder of the road. The vehicle 1 hit the sunken manhole and went over a smooth road, classifying them as the impulse and smooth classes. The vehicle 2 drove closer to the shoulder and classified the raveling as the rough class, while missing the sunken manhole. The corresponding acceleration responses are shown Figures 6.16cd. The ground truth, annotated as "Rough surface", was accurately classified by the two vehicles as the rough class and the acceleration responses are shown in Figures 6.16ef.

As shown in Figure 6.15, the locations of the classification results that do not have annotations are not identical. The differences in their locations can occur when the

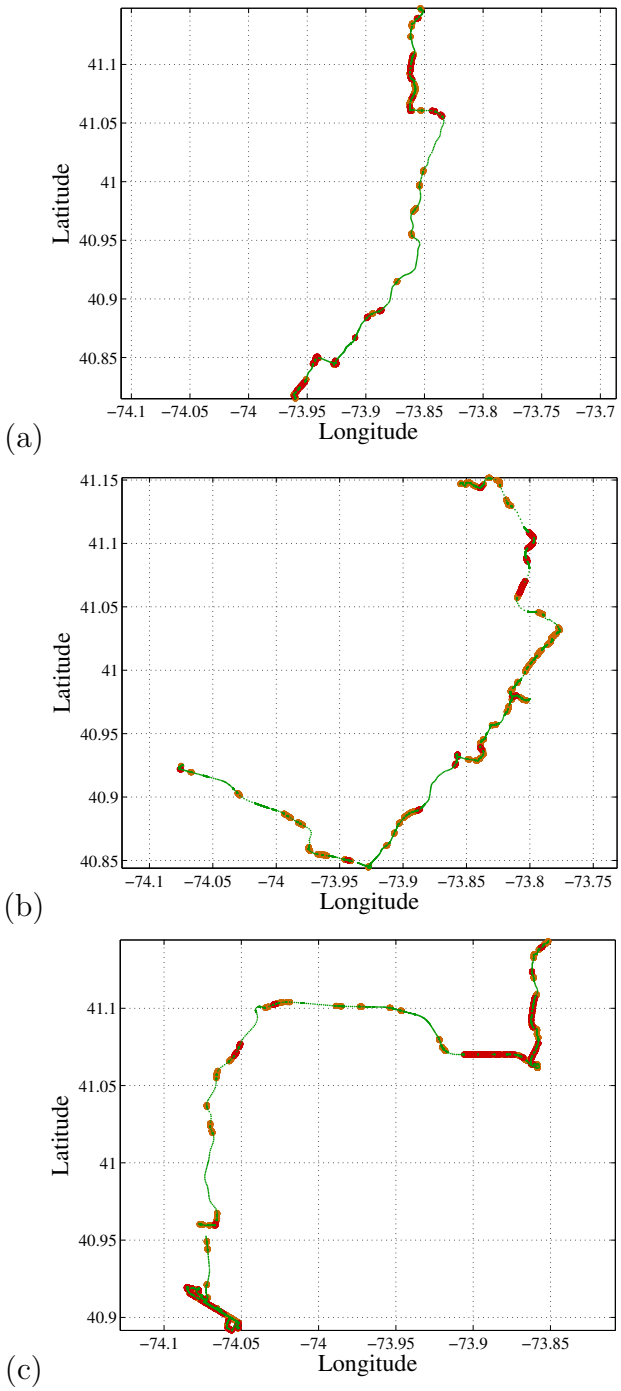

Figure 6.14: Detected street defects based on the data collected from three different vehicles: (a) result from the vehicle 1; (b) result from the vehicle 2; and (c) result from the vehicle 3.

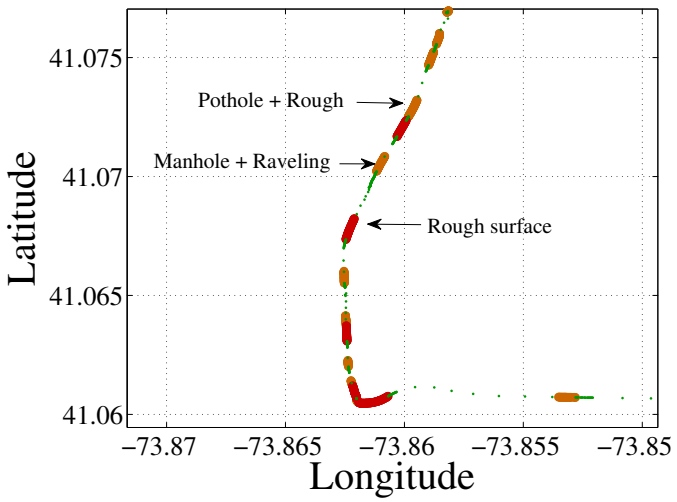

(a)

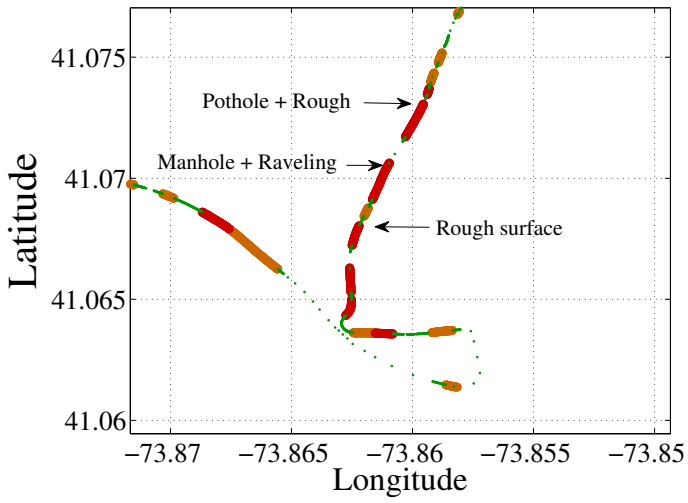

(b)

Figure 6.15: Identified road surface conditions on the overlapping route: (a) result from the vehicle 1, and (b) result from the vehicle 3.

vehicles travel in different lanes and/or different directions. It can also occur when some drivers may try to avoid street defects while still traveling in the same lane and direction. To increase the performance of the road surface monitoring system, the conditions of the road surfaces should be evaluated by integrating classification results from multiple vehicles. How to integrate the results based on their locations and moving directions is explained in the following section.

Most street defects classified into the impulse class are either potholes or sunken manholes. Some pavement joints are also detected as part of the impulse class. The acceleration responses due to a pothole and a sunken manhole generally differ from the ones due to a pavement joint. A pothole and a sunken manhole are usually hit by one side of a vehicle, causing a higher amplitude in the y direction. However, a pavement joint usually produces a higher amplitude in the z direction since it is hit by two tires (the front two and then the back two) at the same time. The defects classified into the rough class include a patch deterioration, shoving, and raveling.

6.5 Discussion

The framework of the data acquisition and integration for the detection of isolated street defects and rough road conditions is demonstrated. Since the sensor package is developed using low-cost off-the-shelf products, its low cost enables one to deploy many connected vehicles for data collection. The cost effectiveness of the suggested method can become more pronounced when it is integrated within an existing fleet management system. Since a fleet data management system in general consists of on-board processors, data storage, data transmission, and GPS sensors, the suggested method can be implemented with a low incremental cost by adding an accelerometer module on fleet vehicles. The suggested method can provide a complementary data

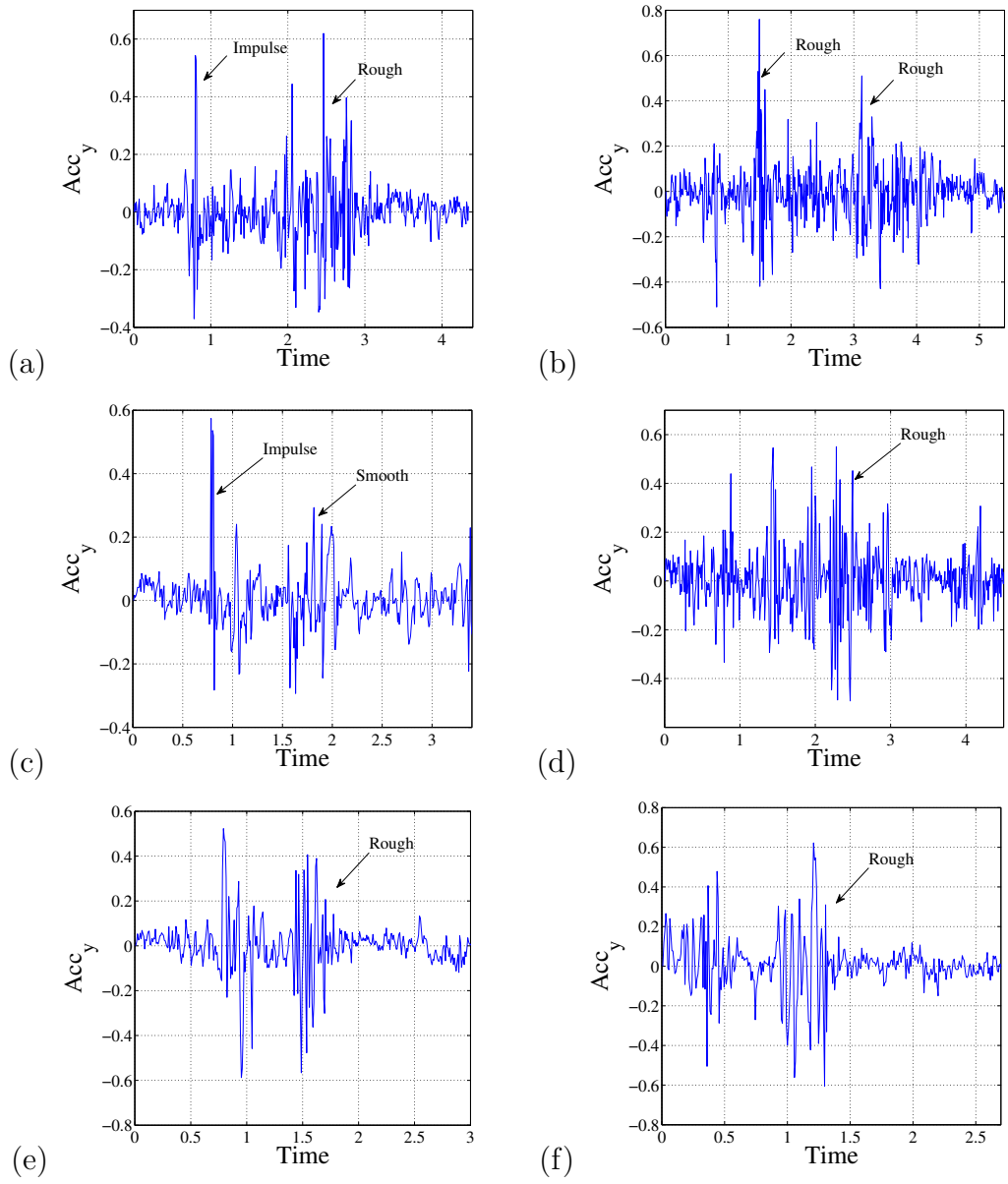

Figure 6.16: Classification results on the overlapping route: (a) result from the vehicle 1 and the "Pothole + Rough" ground truth; (b) result from the vehicle 3 and the "Pothole + Rough" ground truth; (c) result from the vehicle 1 and the "Manhole + Raveling" ground truth; (d) result from the vehicle 3 and the "Manhole + Raveling" ground truth;(e) result from the vehicle 1 and the "Uneven surface" ground truth; and (f) result from the vehicle 3 and the "Uneven surface" ground truth.

source for pavement distress management. The compact native of the acceleration data and the local data logging algorithm permit less frequent data transmission to the backend server. If vehicles are dispatched and come back to a base station such as a parking lot on a regular basis, a Wi-Fi hotspot can be installed at a base station. If cellular data transmission is used instead of the delay tolerant network and the trajectory clustering analysis is carried out in an online fashion, a result of the suggested system can be updated in real-time.

To make the suggested method more practically useful, a more robust classifier should be trained to predict more specific output categories. The output categories used here are determined based on the dynamic responses of vehicles, not based on street defect types or their severity levels. In the future, output categories should be more specifically determined based on both pavement distress types and severity levels which are summarized by Miller and Bellinger (2014). It could be possible to distinguish a pothole and a joint because acceleration responses due to a pothole and a pavement joint are different as mentioned before. A moderate pothole, a severe pothole, a normal joint, and damaged joint can be used instead of the impulse class. If a classifier is able to categorize a street defect based on its type and severity level, the street defect rating for the representative trajectory can become more practically meaningful since each trajectory can vote for the rating based on the type and severity level. For example, a pothole with a high severity level, which may necessitate a priority for treatment, would have a higher score than a moderate pothole. A higher score can be assigned to successive street defects to improve the rating system for the representative trajectories. In addition to neural networks and random forests, other learning algorithms such as support vector machines and logistic regression also can be used for the suggested system. A comparison between different learning algorithms should be done based on a large enough data set and various performance metrics.

The characteristics of different learning methods also can be taken into account based on the need of applications. To develop a more robust classifier, more training data sets are needed. They can be collected from a controlled test. They also can be collected by the suggested method. One of the advantages of the suggested method is that data sets are structurally formatted by the local data logging algorithm and grouped based on their locations and directions by the trajectory clustering algorithm. Those grouped data can be valuable since they have a potential to be used as training data sets when the corresponding types and severity levels of street defects become known. For example, one day a crew finds a pothole and reports its diameter and depth. Then, a large amount of already-grouped data that correspond to the reported pothole can be used as training data sets not only to update an existing classifier to improve a prediction accuracy, but also to develop a new classifier to predict more specific output categories.

Data collected from various vehicles exhibit a curtain level of variation. Acceleration responses of vehicles over the same street defect can vary due to different suspension systems, different total masses, and different vehicle speeds. The acceleration responses of vehicles can also vary due to road surface types (Belzowski & Ekstrom, 2015). Those variations due to the above-mentioned factors should be properly studied based on a large volume of data. The understanding of the variations is very important in the vibration-based approach and will help develop a more robust algorithm for the pavement distress detection and/or the evaluation of road surfaces roughness. In addition, large enough data sets from various vehicles are also required to study the reliability of the suggested method. It will be important to determine how many data samples over the same street defect are needed to produce a reliable result. What level of reliability can be provided by integrating results from various vehicles, compared to the current rating system such as PASER (Walker, Entine,

& Kumer, 2002) and/or the IRI. Recently, many researchers have studied the relationship between data from various vehicles and the current standard rating system. Dawkins and Powell (2011) related the acceleration data measured from the on-board sensors of the probe vehicles with the IRI and recommended the RMS values in the vertical direction as the primary means for IRI estimation. Mixon et al. (2012) compared the data measured from aftermarket accelerometers mounted on fleet vehicles with a road surface profiles obtained from the profilometry van equipped with single-point lasers and band-type profilometers. They concluded that it may be possible with sufficiently large data sets to correlate a given vehicle and device's characteristic responses to other pavement condition measures like the IRI and PASER rating. However, in this study, the data sets used here are insufficient to study the variation of data and the reliability of the results from the suggested method. More data should be collected from various vehicles and different road conditions to explore the variation and reliability of data. Processing big data might need an computationally efficient algorithm and/or a great deal of computational resources.

6.6 Conclusions and Future Work

The suggested monitoring system can be complementary to the current data collection practice by providing a continuous data source for isolated pavement distress and rough roads. The monitoring system consists of the vehicle clients and the back-end server. A local data logging algorithm embedded in the vehicle clients improves the efficiency of the use of local storage and provides preliminarily evaluation of the road surface conditions based on the predetermined thresholds. The data cached in local storage are sent back to the server, where the trained classifier categorizes the transmitted data into the three classes. The suggested framework enhances the

efficiency of the data logging process. Furthermore, the reliability of the suggested monitoring system is improved by having the dual detectors (the threshold-based filtering and the trained classifier).

Chapter 7

Trajectory Clustering: Application to Road Surface Monitoring

The suggested framework of a data collection system for pavement distress management, which is presented in the previous chapter, utilizes multiple connected vehicles. In order to provide a more reliable data resource for the road surface condition monitoring, it is necessary to integrate road conditions evaluated from multiple vehicles. Trajectory clustering is such a technique that groups trajectory data, which are the sequence of GPS positioning data with respect to time, based on the proximity of locations and moving directions. This chapter introduces the trajectory clustering technique and how it is applied to the suggested framework as a data integration scheme.

7.1 Introduction

Recently, a huge volume of trajectory data have become available due to the development of satellite systems and tracking facilities. vehicle tracking, storm path, and

animal movement data are examples of trajectory data. In order to analyze various trajectory data sets, trajectory clustering algorithms have been developed and developing in the field of data mining in computer science. The trajectory clustering algorithm using the regression mixture model and the maximum likelihood principle is developed (S. Gaffney & Smyth, 1999; S. J. Gaffney, Robertson, Smyth, Camargo, & Ghil, 2007). The partition-and-group framework is proposed for trajectory clustering (Lee, Han, & Whang, 2007). Since the latter method can produce common sub-trajectories (representative trajectories), it is adapted and modified to become applicable to the proposed road surface monitoring system.

Figure 7.1 shows a schematic of the trajectory clustering analysis. Trajectories are the sequence of GPS positioning data with respect to time. The method under consideration here is used to group trajectory data not only based on their locations, but also based on their moving directions. Since moving directions are taken into account for the trajectory clustering analysis, the main advantage of this analysis is the capability of analyzing a moving trend of massive trajectory data sets. The suggested trajectory clustering analysis consists of two parts. The first part is to group trajectories based on a predefined inter-vector distance calculation. Once certain groups of trajectories, which are also known as clusters, are formed, a representative trajectory is calculated for each cluster by considering trajectories belonging to the corresponding cluster.

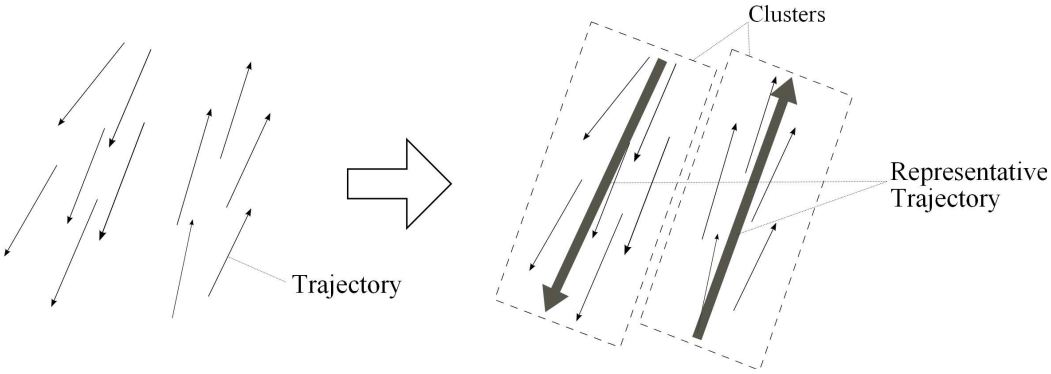

Figure 7.1: Trajectory clustering.

7.2 Trajectory Clustering analysis

7.2.1 Inter-vector distance function

A distance function is defined in order to calculate the locational and directional difference between two trajectories. The distance function consists of three components: (i) the *perpendicular distance* ($d_\perp$), *parallel distance* ($d_\parallel$), and *angular distance* (d_θ). The first two are the distances for proximity. The last is to evaluate the directional difference. The distance between two trajectories is shown in Figure 7.2. The longer and shorter trajectories are defined as L_i ($\overrightarrow{s_i e_i}$) and L_j ($\overrightarrow{s_j e_j}$), respectively. p_s and p_e are the projection points of s_j and e_j onto L_i. The projection points p_s and p_e can be calculated using vector operations, which is defined as follows:

$$p_s = s_i + u_1 \cdot \overrightarrow{s_i e_i}, \quad p_e = s_i + u_2 \cdot \overrightarrow{s_i e_i}, \tag{7.1}$$

where u_1 and u_2 are defined as:

$$u_1 = \frac{\overrightarrow{s_i s_j} \cdot \overrightarrow{s_i e_i}}{\|\overrightarrow{s_i e_i}\|^2}, u_2 = \frac{\overrightarrow{s_i e_j} \cdot \overrightarrow{s_i e_i}}{\|\overrightarrow{s_i e_i}\|^2} \tag{7.2}$$

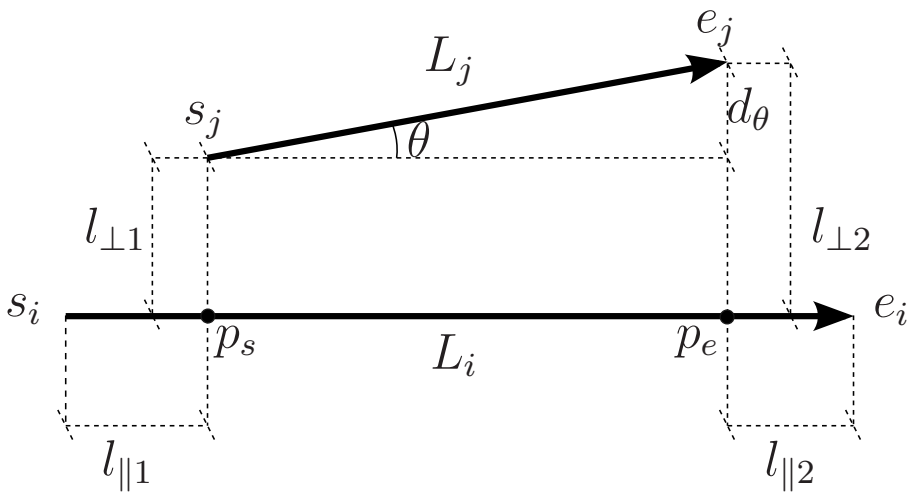

Figure 7.2: Distance function for two trajectory.

The *perpendicular distance* ($d_\perp$) between L_i and L_j is defined as the Lehmer mean of order two. It becomes:

$$d_\perp(L_i, L_j) = \frac{l_{\perp 1}^2 + l_{\perp 2}^2}{l_{\perp 1} + l_{\perp 2}}, \tag{7.3}$$

where $l_{\perp 1}$ and $l_{\perp 2}$ are the Euclidean distances from s_j and e_j to p_s and p_e, respectively. The *parallel distance* between L_i and L_j is defined as a minimum value of $l_{\parallel 1}$ and $l_{\parallel 2}$, which are the Euclidean distances from p_s and p_e to the nearest s_i or e_i, respectively. The parallel distance is:

$$d_\parallel(L_i, L_j) = min(l_{\parallel 1}, l_{\parallel 2}). \tag{7.4}$$

The *angular distance* between two trajectories is defined as:

$$d_\theta(L_i, L_j) = \begin{cases} \|L_j\| \times sin(\theta) & \text{if } 0° \leq \theta \leq 90° \\ \|L_j\| \times (1 + sin(\theta - 90°)) & \text{if } 90° \leq \theta \leq 180°, \end{cases} \tag{7.5}$$

where θ is calculated as follows:

$$cos(\theta) = \frac{\overrightarrow{s_i e_i} \cdot \overrightarrow{s_j e_j}}{\|\overrightarrow{s_i e_i}\| \|\overrightarrow{s_j e_j}\|} \tag{7.6}$$

A distance between two trajectories is a weighted sum of above three distances. $w_\perp$, $w_\parallel$, and w_θ are weights for the perpendicular, parallel, and angular distance, respectively. Since the direction of trajectories should be properly considered in the trajectory clustering, more weight is placed on the angular distance. The weights are defined as follows:

$$w_\perp = w_\parallel = 1, \quad w_\theta = \frac{d_{cut}}{2 \times frag_{min}}, \tag{7.7}$$

where d_{cut} is a cutoff distance in the clustering (the maximum distance between the trajectories in the same cluster) and $frag_{min}$ is the smallest travel distance of *data fragments*. The distance function between two trajectories becomes:

$$dist(L_i, L_j) = w_\perp \cdot d_\perp(L_i, L_j) + w_\parallel \cdot d_\parallel(L_i, L_j) + w_\theta \cdot d_\theta(L_i, L_j). \tag{7.8}$$

7.2.2 Hierarchical clustering

Based on the distances calculated by Eq. 7.8, the hierarchical clustering algorithm (Murtagh, 1983) is used for the trajectory clustering analysis. The hierarchical clustering algorithm is suitable for this application since it includes all trajectories into an analysis. More interest is placed on knowing the road condition with an emphasis on the location precision, which means the size of clusters should be constant. Therefore, complete linkage clustering is used for the linkage criterion, which can prevent a chaining phenomenon (Defays, 1977). The trajectories are grouped into the final clusters in such way that the trajectories in the same cluster have distances which are

less than a specified distance threshold, which is 35 meters in this application. Since the higher weight factors are assigned for the *angular distance*, nearby trajectories with the different directions are clustered into the different clusters.

7.2.3 Representative trajectories

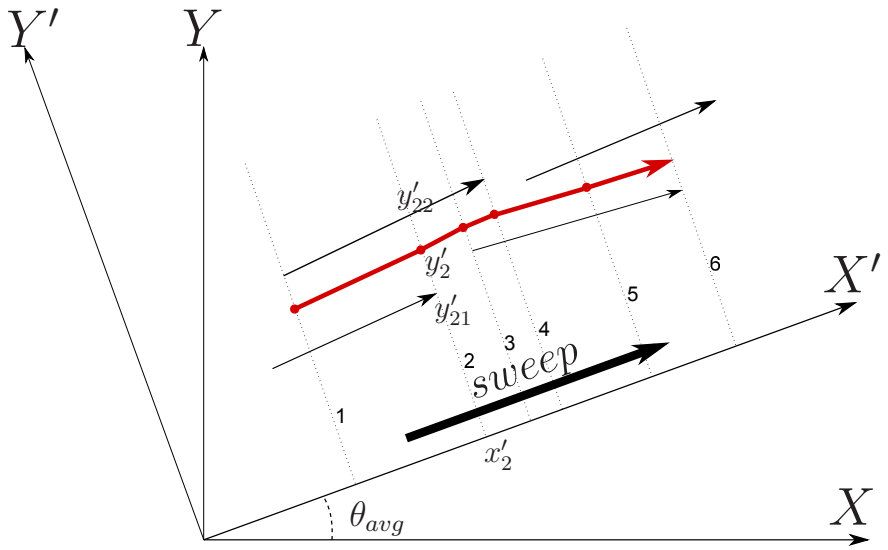

Figure 7.3: Representative trajectory.

A representative trajectory is calculated for each cluster. It represents the overall movement of the trajectories in the same cluster. Instead of showing all trajectories with corresponding street defect classes on a map, the extracted information of the trajectories helps represent the conditions of road surfaces in a more compendious way. The algorithm of generating the representative trajectories is developed in (Lee et al., 2007). Each representative trajectory consists of a sequence of points, which are determined by a sweep line approach. The sweeping of a vertical line is performed in the direction of a average vector. In Figure 7.3, the representative trajectory (the red arrow) and the vertical sweeping lines (the dotted lines) are illustrated with the

trajectories (the black arrows) grouped into the same cluster. After calculating the angle of the average direction vector θ_{avg}, the axes (X and Y) are rotated by θ_{avg} so that the average direction vector becomes parallel to the X' axis. In the rotated coordinate system, vertical line sweeping is performed along the X' axis. At the starting and end points of all trajectories, the coordinates of the representative trajectory are calculated only when the number of points of intersection of the trajectories and the vertical sweeping line is bigger than two. The coordinates of the representative trajectory is the average of the intersecting points with each vertical sweeping line. The n^{th} point of the representative trajectory can be calculated in the X' and Y' coordinate system, which is defined as follow:

$$(x'_n, y'_n) = \left(x'_n, \sum_{m=1}^{N_{overlap}} \frac{y'_{nm}}{N_{overlap}} \right), \tag{7.9}$$

where $N_{overlap}$ is the number of the intersecting points for the n^{th} vertical sweeping line.

7.2.4 Robustness of the trajectory clustering for measurement noise

The trajectory clustering analysis can be robust for the measurement noise due to its averaging routine in the calculation for representative trajectories. To verify its robustness for measurement noise, 360 trajectories are simulated. Then, Gaussian noise is added to the simulated trajectories. The histogram of measurement errors (the radial distances between the original data points and the noisy data points in meters) is shown in Figure 7.4a. The noise level that is added to the original trajectories is much higher than the noise level that is expected for the GPS module used in this

study (less than 3 m). Figure 7.4b shows the original and noisy trajectories, in which the blue lines correspond to the original simulated trajectories (no noise) and the red lines represent the noisy ones. The trajectory clustering method is applied to those two trajectory data sets. Then, representative trajectories are drawn for the original and noisy trajectory data sets. Figure 7.4c shows the calculated representative trajectories for those two data sets. The blue representative trajectories are calculated based on the original (no noise) trajectories. The red representative trajectories are drawn based on the noisy trajectories. It can be seen that there is a quite good agreement between those two sets of the representative trajectories despite the high level of measurement noise that was added to the original data set.

7.3 Application: Integration of the Result of Road Surface Monitoring System

7.3.1 The rating of road surface conditions for each trajectory cluster

As it is shown in Figure 7.1, each collected *data fragment* is in fact a trajectory since its GPS positioning data track the movement of the vehicle. It is worth noting that each trajectory is a *data fragment* whose RMS values satisfy the triggering condition defined by Eq. 6.2. Each trajectory has a predicted class from the trained neural network and a travel distance. The data sets that do not satisfy the triggering condition have no contribution to the trajectory clustering analysis. During the analysis, *data fragments* are grouped with respect to both their proximity and directions. Then, a representative trajectory for each cluster is drawn to show the average movement of

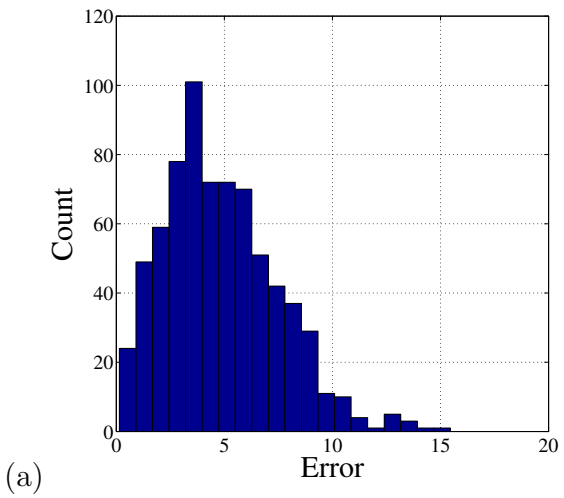

(a)

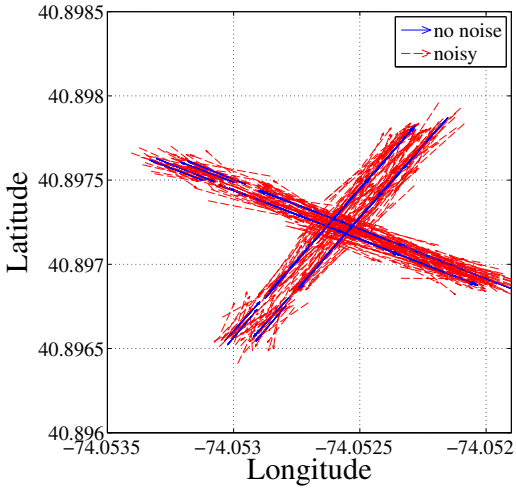

(b)

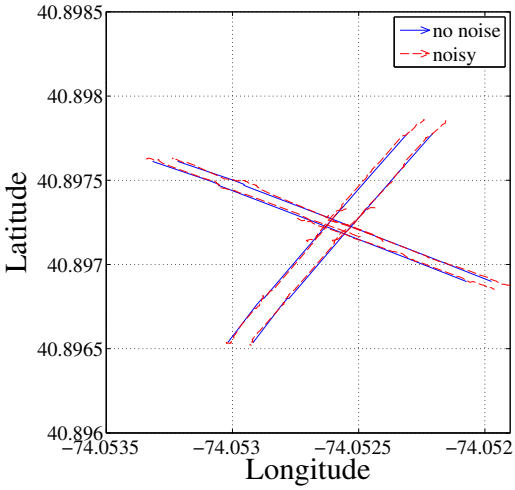

(c)

Figure 7.4: Trajectory clustering on simulated data sets: (a) The histogram of measurement errors in meter; (b) simulated trajectories; and (b) corresponding representative trajectories.

the trajectories grouped into the same cluster and to represent an integrated classification result.

Each data trajectory has a respective predicted class of street defects from the trained classifier. The trajectories included in the same cluster can have different predicted classes. As a result, the identification of street defects for each representative trajectory should be evaluated by integrating the predicted classes of trajectories that are used to draw a representative trajectory. The method used here is a weighted averaging mechanism. The data trajectories that are grouped into the same cluster vote for a road condition associated with a representative trajectory of that cluster. For each data fragment, a traveling distance is also calculated based on a vehicle speed and recorded time. Traveling distances and the predicted street defect classes of the data fragments evaluate the street defect level for a representative trajectory. The score of each data fragment can be assigned depending on the application needs. In this application, the score equals to unity when the predicted class of a trajectory is either the rough or the impulse class. For the smooth class, a zero score is assigned. It is possible to assign different scores for the street defect classes when more interest is placed on knowing a specific class. As an example, if one is more interested in the identification of potholes, a higher score can be assigned to the impulse class. The levels of street defects for representative trajectories are determined based on scores and travel distances corresponding to data trajectories in the same cluster. It is noteworthy that the data fragments, whose RMS values pass the thresholds defined in Eq. 6.2, only affect the evaluation of road conditions. A road condition level is calculated as follows:

$$\text{Street defect level} = \sum_{i=1}^{n} \frac{score_i \times travel\ distance_i}{\sum_{j=1}^{n} travel\ distance_j}, \tag{7.10}$$

where n is the number of trajectories included in the same cluster, i.e., the number of the trajectories to draw a representative trajectory. The street defect level ranges from 0 to 1. The level 0 denotes a pavement surface where no significant street defects are detected. The level 1 indicates a high level of chances to hit street defects. The trajectory data in Figure 6.14 are clustered based on the previously-mentioned trajectory clustering method. The representative trajectories and the street defect levels are calculated. Ten different colors from green to red are used for each representative trajectory to visualize an estimated street defect level. The level 0 calculated by Eq. 7.10 is shown as a green representative trajectory. The level 1 is marked with a red representative trajectory.

The representative trajectories in the small road network mentioned in the previous section are shown in Figure 7.5a. The representative trajectories corresponding to "Pothole + Rough", " Manhole + Raveling", and "Rough surface" are shown in Figures 7.5bcd, respectively. As shown in the small road networks, the trajectory clustering method successfully partitions the trajectories that are located within close proximity with different moving directions into different clusters. The trajectory clustering method has applied to the 2554 trajectories collected from the overall tested road networks and found 1128 clusters (representative trajectories). This clustering method can provide a much simpler format of data as representative trajectories, which are much easier to visualize and interpolate identified street defect levels. Furthermore, if more data are collected from the same road networks, the size of the final clusters (the total number of representative trajectories) should not significantly increase since newly-collected data are expected be grouped into already existing clusters. The trajectory clustering results are also visualized on online maps (Google Maps, 2015). Figure 7.6a shows the representative trajectories demonstrated in Figure 7.5. The overall tested road networks are shown in Figure 7.6b. Although it was

practically challenging to compare the the numerical quantity (identified street defect levels) with manual survey results, which can be subjective, the overall preliminary results were reasonably correlated with the observed road conditions. Moreover, some road networks that were identified as being in poor condition were resurfaced after this study.

7.3.2 GPS accuracy

The accuracy of the GPS positioning data plays a significant role in the trajectory clustering analysis since it can affect the positions of the representative trajectories and the corresponding ratings for street defects. The positioning errors (measurement noise) are mostly less than 3 meters when there is no significant object between the GPS module and satellites. The suggested trajectory clustering method is robust to those errors due to its averaging routine, which has been verified with simulated data. As shown in Figure7.6a, the representative trajectories are reasonably positioned since the satellite communication was fairly good around that area. When the satellite communication is blocked by an object such as a high-rise building and a civil structure, the GPS module performs jammer detection and reduction as well as multi-path detection and compensation to improve positioning data. It is observed that some representative trajectories are positioned such that they slightly deviate from the geometry of road. In this case, the GPS positioning errors are in the magnitude of 20 meters when an object moderately blocks the satellite communication. It is also observed that the GPS positioning errors increase up to 30 meters when the satellite communication is mostly blocked by a tunnel. If trajectory data are misplaced on a wrong road due to the positioning error, it becomes possible that misplaced trajectories can have a negative effect on the position and rating of the

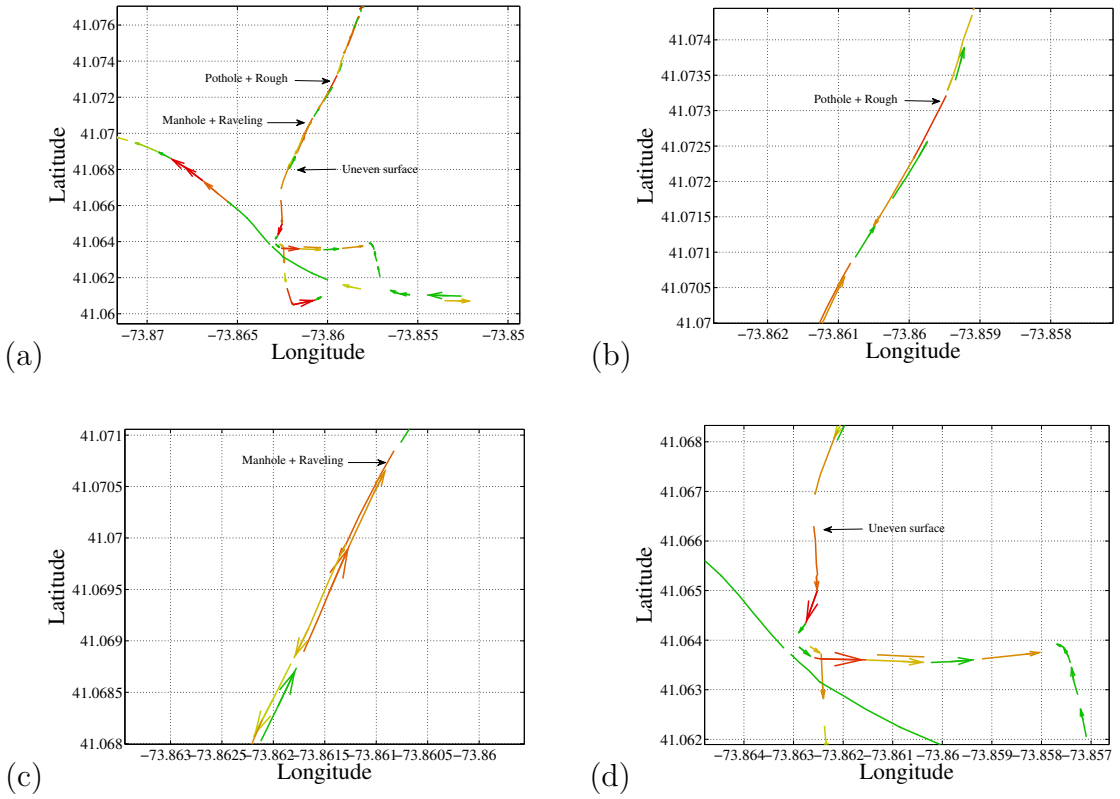

Figure 7.5: Results of the trajectory clustering analysis: (a) representative trajectories in the small area; (b) representative trajectories for "Pothole + Rough"; (c) representative trajectories for " Manhole + Raveling"; and (d) representative trajectories for "Uneven surface".

(a)

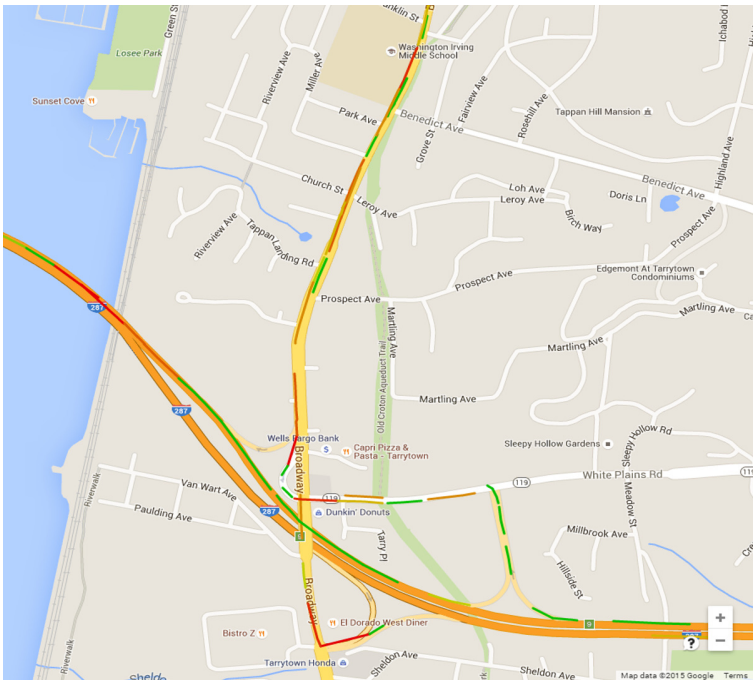

(b)

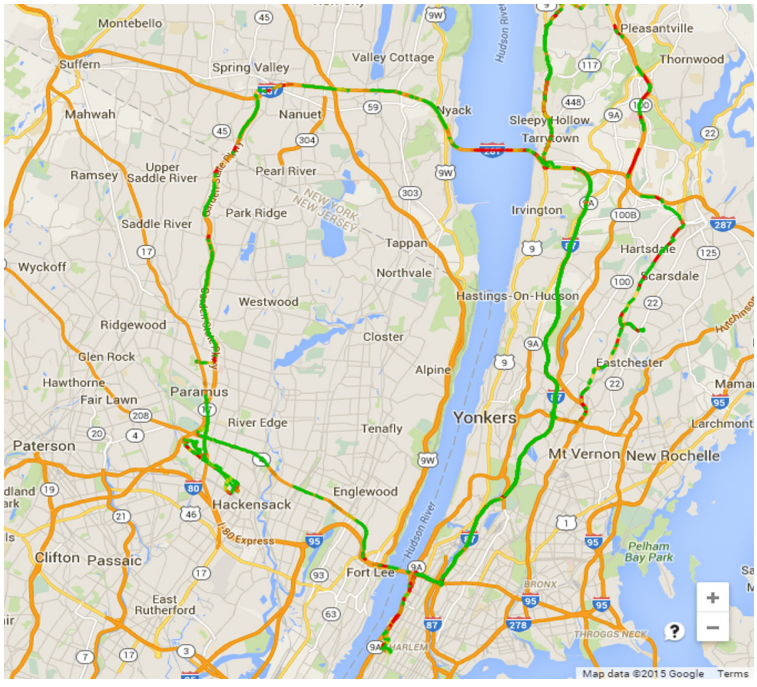

Figure 7.6: Results of the trajectory clustering analysis on online map: (a) representative trajectories in the small area (b) overall trajectory clustering result.

representative trajectory that they belong to. A more accurate GPS module can be used to improve the quality of positioning data. It can be also improved by applying the data snapping method suggested by Pack, Ogale, and Carceroni (2014) and/or by Kalman filtering (Sasiadek, Wang, & Zeremba, 2000) since the positions of vehicles are tracked with respect to time.

7.4 Conclusions

After classifying the collected data fragments, the trajectory clustering method enables the classification results to be integrated with respect to not only their locations, but also their moving directions. The representative trajectories are also drawn to visualize the integrated ratings with the different color scales. The trajectory clustering analysis helps to evaluate road conditions by multiple sensor equipped vehicles.

The data used in this study are collected from three different vehicles over limited road networks. In order to further develop a robust classifier and a rating system for representative trajectories, a large volume of data from various vehicles and different road conditions are required. Those large data also can help investigate the reliability of the data source provided by the suggested method. In the future research, more study should be conducted to understand the correlation between integrated results and the current rating system for pavement distress to provide more reliable and useful data sources. GPS data refinement methods can be implemented to improve the accuracy of the GPS positioning data which might affect the results of the trajectory clustering analysis. Processing a large volume of trajectory data can be challenging since pairwise inter-vector distances between all possible combination of trajectories are required. An efficient approach to deal with a large amount of trajectory data should be developed in the future.

Part III

Conclusions

Chapter 8

Conclusions

This dissertation has explored data analytics on various monitoring data collected from infrastructure. By leveraging real monitoring data, an effort was made to provide practically meaningful information and/or knowledge for the infrastructure management systems, especially for a large suspension bridge and pavement distress.

Acceleration responses measured on a large suspension bridge are used to explore the topics of temperature effects on natural frequencies and FE model updating. In the study of temperature effects on natural frequencies, an FE model is used to simulate temperature distribution effects on modal frequencies. The modeling of the thermal effects on natural frequencies and a method that generates random temperature distributions are demonstrated. A comprehensive comparison between linear and machine learning models is made for the temperature effects. For the thermal effects on the natural frequencies of the particular structure considered here, it is concluded that there is no significant improvement with machine learning models compared to a linear model. An in-depth understanding of the relationships between temperature distributions and natural frequencies can be fundamentally important in the vibration-based damage detection techniques since it can normalized out frequency

variations due to temperature from observed variations: damage detection algorithms applied to normalized frequency variations can provide a more reliable result.

In this study, both deterministic and probabilistic model updating approaches are covered. Moreover, a sophisticated full-scale FE model and real measured data are used to investigate the feasibility and applicabilities of various existing model updating techniques. In the deterministic (sensitivity-based) approach, the regularization technique is adopted and applied to deal with mode shapes agreements by placing nonlinear constraints on the MAC values between identified mode shapes and ones from an FE model. The suggested MAC constrains can be added to a model updating routine to find an optimal solution whose MAC values are above a predetermined threshold with a single optimization run. The suggested method can be further developed to deal with a problem in which mode shapes have more errors compared to natural frequencies due to a limited set of measurements and high noise levels. The sensitivity-based clustering method is first applied to the parameterization of a bridge model updating. This method determines an effective set of updating parameters by grouping similar sensitivities of natural frequencies with respect to mass densities and stiffness-related parameters of decomposed structural components. Each updating parameter includes the physical properties of structural components which have a similar effect on natural frequencies, which leads to a better updating result. The sensitivity analysis on updating parameters also provides structural engineers with fundamental knowledge that clarifies the relationship between structural components and natural frequencies.

In the probabilistic approach, the Bayesian model updating framework is used to update a full-scale FE model to match with measurements in an effort to study its feasibility to a more practical and complex problem. The Bayesian model updating technique has been mostly used with simple models and simulated data since a con-

trolled simulation-based study is preferred to validate whether a new method can lead to a benefit and a reasonable result. This study has made an effort to extend the application of the Bayesian model updating technique to a practical problem since a sophisticated full-scale model is, in general, used in industry. The HMC method, which is used in this study to generate posterior samples, provides a robust capability to deal with the comparatively large number of updating parameters. Generated posterior samples are further used to analyze uncertainty propagations to natural frequencies and mode shapes of an FE model. More work can be done as an extension of the Bayesian model updating such as a model selection problem with different sets of updating parameters using the Bayesian scheme. Surrogate models can replace an FE model to significantly reduce computational expenses. The two-stage Bayesian formulation (Au & Zhang, 2016; F.-L. Zhang & Au, 2016) also can be implemented in a Bayesian model updating problem to take the uncertainty of modeling errors into account.

Measured dynamic responses and positioning data from vehicles are used to develop a framework of data collection and integration for the detection of pavement distress. The suggested road condition monitoring system takes advantage of sensing technology, wireless data transmission, and an innovative data mining algorithm to detect isolated street defects and rough road surfaces. The local data logging algorithm is developed and embedded in each vehicle client to increase the efficiency of data logging. The trajectory clustering method is introduced as a mean of grouping trajectory data and the corresponding classification results based on their locations and moving directions. The suggested monitoring system can continuously provide complementary data sources for the current pavement data collection system, which can be valuable information for the management of quickly-developing pavement distresses. The introduced trajectory clustering analysis can be used by researchers to

condense a large volume of trajectory data into highly-compact representative trajectories, which are much easier to interpret and extract meaningful trends from within massive numbers of trajectories. The main challenge of the trajectory analysis on big data is that it necessitates a great deal of computational resources when processing data in a batch mode. For example, huge memory is needed for pairwise inter-vector distances between all possible combinations of trajectories. One of ways to circumvent tremendous computational requirements can be to process data incrementally, which means that representative trajectories are updated piece-by-piece when a new trajectory is added to an analysis. The incremental trajectory clustering method can be further used to process streaming trajectory data in an online fashion, which can be practically useful in an application that needs to obtain a real-time result. Future investigation is planned to develop the incremental trajectory clustering technique and apply it to massive trajectory data to highlight the advantage of this innovative data analytic method.

Bibliography

ABAQUS/CAE user's manual : version 6.4. (2003). Pawtucket, RI : ABAQUS.

Akaike, H. (1974, Dec). A new look at the statistical model identification. *IEEE Transactions on Automatic Control*, *19*(6), 716-723. doi: 10.1109/TAC.1974.1100705

Allemang, R. J., & Brown, D. L. (1982). Correlation coefficient for modal vector analysis. In *Proceedings of the international modal analysis conference & exhibit* (pp. 110–116).

Amador-Jiménez, L., & Matout, N. (2014). A low cost solution to assess road's roughness surface condition for Pavement Management. In *Transportation research board 93rd annual meeting.*

ASME. (2007). B31. 1-Power Piping. *The American Society of Mechanical Engineers*.

Atassi, L. (2014, Nov. 6, 2014). *Claims filed in 2014 for Cleveland pothole damage already surpass last year's total.* Retrieved from `http://www.cleveland.com/cityhall/index.ssf/2014/04/claims_filed_in_2014_for_cleve.html`

Au, S.-K., & Zhang, F.-L. (2016). Fundamental two-stage formulation for Bayesian system identification, Part I: General theory. *Mechanical Systems and Signal Processing*, *66–67*, 31 - 42.

Bakir, P. G., Reynders, E., & De Roeck, G. (2007). Sensitivity-based finite element model updating using constrained optimization with a trust region algorithm. *Journal of Sound and Vibration*, *305*(1-2), 211-225.

Bakir, P. G., Reynders, E., & De Roeck, G. (2008). An improved finite element model updating method by the global optimization technique 'Coupled Local Minimizers'. *Computers & Structures*, *86*(11-12), 1339-1352.

Balmès, É., Basseville, M., Bourquin, F., Mevel, L., Nasser, H., & Treyssede, F. (2008). Merging sensor data from multiple temperature scenarios for vibration monitoring of civil structures. *Structural health monitoring*, *7*(2), 129–142.

Balmès, É., Basseville, M., Mevel, L., & Nasser, H. (2009). Handling the temperature effect in vibration monitoring of civil structures: A combined subspace-based and nuisance rejection approach. *Control Engineering Practice*, *17*(1), 80 - 87.

Balmès, É., Corus, M., Siegert, D., et al. (2006). Modeling thermal effects on bridge dynamic responses. In *Proceedings of the 24th international modal analysis conference (imac-xxiv).*

Beck, J., & Arnold, K. (1977). *Parameter estimation in engineering and science.* New York: Wiley.

Beck, J. L., & Au, S.-K. (2002). Bayesian updating of structural models and reliability using Markov chain Monte Carlo simulation. *Journal of Engineering Mechanics*, *128*(4), 380–391.

Beck, J. L., & Katafygiotis, L. S. (1998). Updating models and their uncertainties. I: Bayesian statistical framework. *Journal of Engineering Mechanics*, *124*(4), 455–461.

Behmanesh, I., & Moaveni, B. (2015). Probabilistic identification of simulated damage on the Dowling Hall footbridge through Bayesian finite element model updating. *Structural Control and Health Monitoring*, *22*(3), 463–483.

Belzowski, B., & Ekstrom, A. (2015). *Evaluating roadway surface rating technologies* (Tech. Rep. No. RC- 1621). Lansing, MI: Michigan Department of Transportation.

Breiman, L. (2001). Random Forests. *Machine Learning*, *45*(1), 5-32. Retrieved from `http://dx.doi.org/10.1023/A%3A1010933404324`

Brewick, P., & Smyth, A. (2013). An investigation of the effects of traffic induced local dynamics on global damping estimates using operational modal analysis. *Mechanical Systems and Signal Processing*, *41*(1–2), 433 - 453.

Brincker, R., Ventura, C. E., & Andersen, P. (2001). Damping estimation by frequency domain decomposition. In *Proceedings of the 19th international modal analysis conference (imac)*. Kissimee, FL.

Brownjohn, J. M. W., Moyo, P., Omenzetter, P., & Lu, Y. (2003). Assessment of highway bridge upgrading by dynamic testing and finite-element model updating. *Journal of Bridge Engineering*, *8*(3), 162-172.

Brownjohn, J. M. W., & Xia, P. Q. (2000). Dynamic assessment of curved cable-stayed bridge by model updating. *Journal of Structural Engineering-Asce*, *126*(2), 252-260.

Bursanescu, L., Bursanescu, M., Hamdi, M., Lardigue, A., & Paiement, D. (2001). Three-dimensional infrared laser vision system for road surface features analysis. In *Romopto 2000: Sixth conference on optics* (pp. 801–808).

Byrd, R. H., Hribar, M. E., & Nocedal, J. (1999). An interior point algorithm for large-scale nonlinear programming. *Siam Journal on Optimization*, *9*(4), 877-900.

Caltrans. (2012). *Bridge design practice manual*. Sacramento, CA: California Department of Transportation.

Chang, K., Chang, J., & Liu, J. (2005). Detection of pavement distresses using 3D laser scanning technology. In *Proc. of the 2005 asce intl. conference on computing in civil engineering* (p. 105). Reston, Virginia: ASCE.

Cheung, S. H., & Beck, J. L. (2009). Bayesian model updating using hybrid Monte Carlo simulation with application to structural dynamic models with many uncertain parameters. *Journal of engineering mechanics*, *135*(4), 243–255.

Ching, J., & Chen, Y.-C. (2007). Transitional Markov chain Monte Carlo method for Bayesian model updating, model class selection, and model averaging. *Journal of engineering mechanics*, *133*(7), 816–832.

Ching, J., Muto, M., & Beck, J. L. (2006). Structural model updating and health monitoring with incomplete modal data using Gibbs sampler. *Computer-Aided Civil and Infrastructure Engineering*, *21*(4), 242–257.

Cornwell, P., Farrar, C. R., Doebling, S. W., & Sohn, H. (1999). Environmental variability of modal properties. *Experimental Techniques*, *23*(6), 45–48.

Cortes, C., & Vapnik, V. (1995). Support-Vector Networks. *Machine Learning*, *20*(3), 273–297. Retrieved from `http://dx.doi.org/10.1023/A:1022627411411` doi: 10.1023/A:1022627411411

Cybenko, G. (1989). Approximation by superpositions of a sigmoidal function. *Mathematics of control, signals and systems*, *2*(4), 303–314.

Dawkins, J., & Powell, B. (2011). Investigation of Pavement Maintenance Applications of Intellidrive SM (Final Report): Implementation and Deployment Factors for Vehicle Probe-based Pavement Maintenance (PBPM). *Auburn Univ., Auburn, AL, USA*.

Defays, D. (1977). An efficient algorithm for a complete link method. *The Computer Journal*, *20*(4), 364-366. Retrieved from `http://comjnl.oxfordjournals.org/content/20/4/364.abstract`

Dennis, E. P., Hong, Q., Wallace, R., Tansil, W., & Smith, M. (2014, Dec. 10, 2015). *Pavement Condition Monitoring with Connected Vehicle Data.* Retrieved from `http://www.cargroup.org/?module=Publications&event=View&pubID=104`

De Zoysa, K., Keppitiyagama, C., Seneviratne, G. P., & Shihan, W. (2007). A public transport system based sensor network for road surface condition monitoring. In *Proceedings of the 2007 workshop on networked systems for developing regions* (p. 9). New York.

Duane, S., Kennedy, A. D., Pendleton, B. J., & Roweth, D. (1987). Hybrid monte carlo. *Physics letters B*, *195*(2), 216–222.

Eaton, R. A. (1989). *Pothole Primer. A Public Administrator's Guide to Understanding and Managing the Pothole Problem* (Tech. Rep. No. 81-21). Cold Regions Research & Engineering Laboratory: US Army Corps of Engineers.

Eriksson, J., Girod, L., Hull, B., Newton, R., Madden, S., & Balakrishnan, H. (2008). The pothole patrol: using a mobile sensor network for road surface monitoring. In *Proceedings of the 6th international conference on mobile systems, applications, and services* (pp. 29–39). New York.

Ester, M., Kriegel, H.-P., Sander, J., & Xu, X. (1996). A density-based algorithm for discovering clusters in large spatial databases with noise. In *Kdd* (Vol. 96, pp. 226–231).

Everitt, B. S., Landau, S., Leese, M., & Stahl, D. (2011). Hierarchical clustering. *Cluster Analysis, 5th Edition*, 71–110.

Fox, R. L., & Kapoor, M. P. (1968). Rates of change of eigenvalues and eigenvectors. *AIAA Journal*, *6*(12), 2426-2429.

Friswell, M. I., Mottershead, J. E., & Ahmadian, H. (2001). Finite–element model updating using experimental test data: parametrization and regularization. *Philosophical Transactions of the Royal Society of London A: Mathematical, Physical and Engineering Sciences*, *359*(1778), 169–186.

Gaffney, S., & Smyth, P. (1999). Trajectory clustering with mixtures of regression models. In *Proceedings of the fifth acm sigkdd international conference on knowledge discovery and data mining* (pp. 63–72). New York.

Gaffney, S. J., Robertson, A. W., Smyth, P., Camargo, S. J., & Ghil, M. (2007). Probabilistic clustering of extratropical cyclones using regression mixture models. *Climate dynamics*, *29*(4), 423–440.

Gavilán, M., Balcones, D., Marcos, O., Llorca, D. F., Sotelo, M. A., Parra, I., ... Amírola, A. (2011). Adaptive road crack detection system by pavement classification. *Sensors*, *11*(10), 9628–9657.

Google Maps. (2015, Dec.10, 2015). *New York,NY.* Retrieved from `https://www.google.com/maps/@40.9186683,-73.9206965,10z?hl=en`

Hanson, K. M. (2001). Markov Chain Monte Carlo posterior sampling with the Hamiltonian method. In *Medical imaging 2001* (pp. 456–467).

Hartigan, J. A., & Wong, M. A. (1979). Algorithm AS 136: A k-means clustering algorithm. *Applied Statistics*, *28*(1), 100–108.

Hastings, W. K. (1970). Monte Carlo sampling methods using Markov chains and their applications. *Biometrika*, *57*(1), 97–109.

Haykin, S. (1998). *Neural Networks: A Comprehensive Foundation* (2nd ed.). Upper Saddle River, NJ, USA: Prentice Hall PTR.

Hjelmstad, K. D., Banan, M. R., & Banan, M. R. (1995). On building finite element models of structures from modal response. *Earthquake Engineering & Structural Dynamics*, *24*(1), 53-67.

Hou, Z., Wang, K. C., & Gong, W. (2007). Experimentation of 3D pavement imaging through stereovision. In *Proc. of intl. conference on transportation engineering (icte)* (pp. 376–381). Reston, Virginia: ASCE.

Hua, X., Ni, Y., Ko, J., & Wong, K. (2007). Modeling of temperature–frequency correlation using combined principal component analysis and support vector regression technique. *Journal of Computing in Civil Engineering*, *21*(2), 122–135.

Živanović, S., Pavic, A., & Reynolds, P. (2006). Modal testing and FE model tuning of a lively footbridge structure. *Engineering Structures*, *28*(6), 857-868.

Živanović, S., Pavic, A., & Reynolds, P. (2007). Finite element modelling and updating of a lively footbridge: The complete process. *Journal of Sound and Vibration*, *301*(1–2), 126-145.

Jolliffe, I. (2005). *Principal component analysis*. New York: Wiley Online Library.

Kim, J.-T., Park, J.-H., & Lee, B.-J. (2007). Vibration-based damage monitoring in model plate-girder bridges under uncertain temperature conditions. *Engineering Structures*, *29*(7), 1354 - 1365.

Kim, J.-T., Yun, C.-B., & Yi, J.-H. (2003). Temperature effects on frequency-based damage detection in plate-girder bridges. *KSCE journal of civil engineering*, *7*(6), 725–733.

Koch, C., & Brilakis, I. (2011). Pothole detection in asphalt pavement images. *Advanced Engineering Informatics*, *25*(3), 507–515.

Koch, C., Jog, G. M., & Brilakis, I. (2012). Automated pothole distress assessment using asphalt pavement video data. *Journal of Computing in Civil Engineering*, *27*(4), 370–378.

Lee, J.-G., Han, J., & Whang, K.-Y. (2007). Trajectory clustering: a partition-and-group framework. In *Proceedings of the 2007 acm sigmod international conference on management of data* (pp. 593–604). New York.

Levin, R. I., & Lieven, N. A. J. (1998). Dynamic finite element model updating using simulated annealing and genetic algorithms. *Mechanical Systems and Signal Processing*, *12*(1), 91-120.

Li, Q., Yao, M., Yao, X., & Xu, B. (2010). A real-time 3D scanning system for pavement distortion inspection. *Measurement Science and Technology*, *21*(1), 8.

Macdonald, J. H., & Daniell, W. E. (2005). Variation of modal parameters of a cable-stayed bridge identified from ambient vibration measurements and FE modelling. *Engineering Structures*, *27*(13), 1916–1930.

Magalhaes, F., Cunha, A., & Caetano, E. (2009). Online automatic identification of the modal parameters of a long span arch bridge. *Mechanical Systems and Signal Processing*, *23*(2), 316–329.

Marler, R. T., & Arora, J. S. (2004). Survey of multi-objective optimization methods for engineering. *Structural and multidisciplinary optimization*, *26*(6), 369–395.

MATLAB. (2013). *Version 8.1.0.604 (Matlab R2013a)*. Natick, Massachusetts: The MathWorks Inc.

McGhee, K. H. (2004). *Automated pavement distress collection techniques* (Vol. 334). Washington, DC: Transportation Research Board.

Metropolis, N., Rosenbluth, A. W., Rosenbluth, M. N., Teller, A. H., & Teller, E. (1953). Equation of state calculations by fast computing machines. *The journal of chemical physics*, *21*(6), 1087–1092.

Miller, J. S., & Bellinger, W. Y. (2014). *Distress identification manual for the long-term pavement performance program* (Tech. Rep. No. FHWA-HRT-13-092).

Mixon, L. T., Garrett, J. K., & Krueger, B. C. (2012). *Vehicle Infrastructure Integration (VII) Data Use Analysis and Processing–Project Summary Report* (Tech. Rep. No. RC-1568). Overland Park, KS: Mixon/Hill of Michigan, Inc.

Moaveni, B., & Behmanesh, I. (2012). Effects of changing ambient temperature on finite element model updating of the Dowling Hall Footbridge. *Engineering Structures*, *43*, 58-68.

Moaveni, B., Conte, J. P., & Hemez, F. M. (2009). Uncertainty and sensitivity analysis of damage identification results obtained using finite element model updating. *Computer-Aided Civil and Infrastructure Engineering*, *24*(5), 320-334.

Moser, P., & Moaveni, B. (2011). Environmental effects on the identified natural frequencies of the Dowling Hall Footbridge. *Mechanical Systems and Signal Processing*, *25*(7), 2336–2357.

Mosquera, V., Smyth, A. W., & Betti, R. (2012). Rapid evaluation and damage assessment of instrumented highway bridges. *Earthquake Engineering & Structural Dynamics*, *41*(4), 755-774.

Mottershead, J. E., Link, M., & Friswell, M. I. (2011). The sensitivity method in finite element model updating: A tutorial. *Mechanical Systems and Signal Processing*, *25*(7), 2275-2296.

Murtagh, F. (1983). A Survey of Recent Advances in Hierarchical Clustering Algorithms. *The Computer Journal*, *26*(4), 354-359. Retrieved from `http://comjnl.oxfordjournals.org/content/26/4/354.abstract`

Muto, M., & Beck, J. L. (2008). Bayesian updating and model class selection for hysteretic structural models using stochastic simulation. *Journal of Vibration and Control*, *14*(1-2), 7–34.

Neal, R. M. (2011). MCMC using Hamiltonian dynamics. *Handbook of Markov Chain Monte Carlo*, *2*.

Ni, Y., Hua, X., Fan, K., & Ko, J. (2005). Correlating modal properties with temperature using long-term monitoring data and support vector machine technique. *Engineering Structures*, *27*(12), 1762–1773.

Ni, Y., Zhou, H., & Ko, J. (2009). Generalization capability of neural network models for temperature-frequency correlation using monitoring data. *Journal of structural engineering*, *135*(10), 1290–1300.

Pack, J., Ogale, A., & Carceroni, R. (2014, May 6). *Snapping GPS tracks to road segments.* Google Patents. Retrieved from `http://www.google.com/patents/US8718932` (US Patent 8,718,932)

Papadimitriou, C., Ntotsios, E., Giagopoulos, D., & Natsiavas, S. (2012). Variability of updated finite element models and their predictions consistent with vibration measurements. *Structural Control and Health Monitoring*, *19*(5), 630–654.

Peeters, B., & De Roeck, G. (2001). One-year monitoring of the Z 24-Bridge: environmental effects versus damage events. *Earthquake engineering & structural dynamics*, *30*(2), 149–171.

Pierce, L. M., McGovern, G., & Zimmerman, K. A. (2013). *Practical Guide for Quality Management of Pavement Condition Data Collection* (Tech. Rep. No. FHWA-HIF-14-006). Washington, DC: Federal Highway Administration.

Priestley, M. J. N., Seible, F., & Calvi, G. M. (1996). *Seismic design and retrofit of bridges*. New York, NY: John Wiley & Sons.

Reynders, E. (2012). System Identification Methods for (Operational) Modal Analysis: Review and Comparison. *Archives of Computational Methods in Engineering*, *19*(1), 51–124.

Reynders, E., Teughels, A., & De Roeck, G. (2010). Finite element model updating and structural damage identification using OMAX data. *Mechanical Systems and Signal Processing*, *24*(5), 1306-1323.

Robert, C. P., & Casella, G. (2005). *Monte Carlo Statistical Methods (Springer Texts in Statistics)*. Secaucus, NJ, USA: Springer-Verlag New York, Inc.

Salton, G., & Buckley, C. (1988). Term-weighting approaches in automatic text retrieval. *Information Processing & Management*, *24*(5), 513-523.

Sasiadek, J., Wang, Q., & Zeremba, M. (2000). Fuzzy adaptive Kalman filtering for INS/GPS data fusion. In *Proceedings of the 2000 ieee international symposium on* (pp. 181–186). New York.

Shahverdi, H., Mares, C., Wang, W., & Mottershead, J. (2009). Clustering of parameter sensitivities: examples from a helicopter airframe model updating exercise. *Shock and Vibration*, *16*(1), 75–87.

Smart Growth America, & Taxpayers for Common Sense. (2014, Dec. 10, 2015). *Repair Priorities 2014: Transportation spending strategies to save taxpayer dollars and improve roads.* Retrieved from `http://www.smartgrowthamerica.org/documents/repair-priorities-2014.pdf`

Sohn, H. (2007). Effects of environmental and operational variability on structural health monitoring. *Philosophical Transactions of the Royal Society of London A: Mathematical, Physical and Engineering Sciences*, *365*(1851), 539–560.

Sohn, H., Dzwonczyk, M., Straser, E. G., Kiremidjian, A. S., Law, K. H., & Meng, T. (1999). An experimental study of temperature effect on modal parameters of the Alamosa Canyon Bridge. *Earthquake Engineering & Structural Dynamics*, *28*(8), 879–897.

Stringer, S. M. (2015, Dec. 10, 2015). *Pothole City: A Data-Driven Look at NYC Roadways.* Retrieved from `http://comptroller.nyc.gov/wp-content/uploads/documents/ClaimStat-Alert-July-2015.pdf`

Teughels, A., & De Roeck, G. (2004). Structural damage identification of the highway bridge Z24 by FE model updating. *Journal of Sound and Vibration*, *278*(3), 589-610.

TRIP. (2015, Dec. 10, 2015). *Conditions and safety of New York 's roads and bridges.* Retrieved from `http://licanys.org/files/4114/2772/7315/TRIP_Report_March_2015.pdf`

Van Gunsteren, W., & Berendsen, H. (1988). A leap-frog algorithm for stochastic dynamics. *Molecular Simulation*, *1*(3), 173–185.

Walker, D., Entine, L., & Kumer, S. (2002). PASER-Manual Asphalt Roads. *Wisconsin Transportation Information Center, College of Engineering, University of Wisconsin, Madison, WI*.

Xia, Y., Hao, H., Zanardo, G., & Deeks, A. (2006). Long term vibration monitoring of an RC slab: Temperature and humidity effect. *Engineering Structures*, *28*(3), 441 - 452.

Xu, Y., Chen, B., Ng, C., Wong, K., & Chan, W. (2010). Monitoring temperature effect on a long suspension bridge. *Structural Control and Health Monitoring*, *17*(6), 632–653.

Yan, A.-M., Kerschen, G., De Boe, P., & Golinval, J.-C. (2005). Structural damage diagnosis under varying environmental conditions—part I: a linear analysis. *Mechanical Systems and Signal Processing*, *19*(4), 847–864.

Yu, B. X., & Yu, X. (2006). Vibration-based system for pavement condition evaluation. In *Applications of advanced technology in transportation. the ninth international conference.* Reston, Virginia: ASCE.

Zhang, F.-L., & Au, S.-K. (2016). Fundamental two-stage formulation for Bayesian system identification, Part II: Application to ambient vibration data. *Mechanical Systems and Signal Processing*, *66–67*, 43 - 61.

Zhang, Q., Chang, T., & Chang, C. (2001). Finite-element model updating for the Kap Shui Mun cable-stayed bridge. *Journal of Bridge Engineering*, *6*(4), 285-293.

Zhou, H., Ni, Y., & Ko, J. (2010). Constructing input to neural networks for modeling temperature-caused modal variability: mean temperatures, effective temperatures, and principal components of temperatures. *Engineering Structures*, *32*(6), 1747–1759.